Optical and Magnetic Properties of Transition Metal and Lanthanide Compounds from a Quantum Chemical Perspective

Zur Erlangung des akademischen Grades einer

DOKTORIN DER NATURWISSENSCHAFTEN

(Dr. rer. nat.)

von der KIT-Fakultät für Chemie und Biowissenschaften
des Karlsruher Instituts für Technologie (KIT)

genehmigte

DISSERTATION

von

M.Sc. Chengyu Jin

Referent: Prof. Dr. K. Fink
Korreferent: Prof. Dr. W. Klopper
Tag der mündlichen Prüfung: 24.4.2024

Abstract

In this thesis, the optical and magnetic properties of complexes containing lanthanide or transition metals were investigated with quantum chemical methods. The study of the magnetic properties of lanthanide sandwich complexes highlights the superior performance of Er-based single molecule magnets (SMMs) in an equatorial ligand field. The introduction of metal-metal interactions enhanced the SMM performance of the Er-based complexes, whereas it impaired that in Dy-based complexes. Extending the molecular approach to cerium oxide, the embedded cluster model balances computational efficiency with accurate property description, paving the way for predicting optical and magnetic properties of high-entropy oxides (HEOs). Ground state investigations revealed no metal-metal interactions for a family of lanthanum-coinage metal complexes. Contrarily, excited state calculations suggested a potential interaction evidenced by the Ligand-to-Metal-Metal Charge Transfer (LMMCT) in a triplet structure of a lanthanum-gold complex. Overall, the thesis employed quantum chemical methods to interpret and predict the optical and magnetic properties of lanthanide and transition metal complex materials. In doing so, it highlights the need for an accurate electronic structure description and explicit consideration of the coordination environment surrounding the metal centers.

Kurzfassung

In dieser Dissertation wurden die optischen und magnetischen Eigenschaften von Lanthanid- und Übergangsmetallkomplexen mit quantenchemischen Methoden untersucht. Eine Studie hebt die überlegene Leistung von auf Erbium basierenden Einzelmolekülmagneten (SMMs) in einer äquatorialen Ligandenumgebung hervor. Hierbei wurde eine Reihe von Lanthanid-Sandwich-Komplexen untersucht. Die Einführung von Metall-Metall-Wechselwirkung verbesserte die SMM-Leistung von Erbium-Komplexen, während sie die von auf Dysprosium basierenden Komplexen beeinträchtigte. Die Ursache ist ein Unterschied in der dipolaren Kopplung. Bei der Erweiterung des molekularen Ansatzes auf periodische Systeme balanciert ein eingebettetes Clustermodell für Ceroxid Recheneffizienz und genaue Eigenschaftsbeschreibung. Dies ebnet den Weg für die Vorhersage optischer und magnetischer Eigenschaften von Hochentropieoxiden (HEOs). Zuletzt ergaben Untersuchungen im Grundzustand keine Metall-Metall-Wechselwirkungen in einer Familie von Lanthan-Münzmetall-Komplexen. Dahingegen legten angeregte Zustandsrechnungen eine potenzielle Wechselwirkung nahe, die durch den Ligand-zu-Metall-Metall-Ladungstransfer (LMMCT) in der Triplettstruktur des Lanthan-Gold-Komplexes belegt wurde. Insgesamt setzte die Dissertation quantenchemische Methoden ein, um die optischen und magnetischen Eigenschaften von Lanthanid- und Übergangsmetallkomplexmaterialien zu interpretieren und vorherzusagen. Dabei zeigte sich die Notwendigkeit einer genauen elektronischen Strukturbeschreibung und einer expliziten Berücksichtigung der Koordinationsumgebung um die Metallzentren.

Contents

1 Introduction

Complexes featuring open-shell transition metal (TM) and lanthanide (Ln) ions present significant potential across various domains, including catalysis,[1–3] luminescent materials[4] and molecular magnetism.[5,6] The aforementioned functionalities arise from the unique electronic structure of the TM and Ln centers. The interplay of ligand-field splitting and spin-orbit coupling (SOC) removes the degeneracy of the electronic states of the free ions, resulting in multiplets with different energies.[7] The intrigue and complexity of researching these complexes escalates with the addition of extra metal ions within the same molecule. Exchange and dipolar couplings between metal centers further influence the electronic states, possibly inducing metal-metal cooperative effects that modify their functionality.[8]

The optical properties of molecules containing open-shell ions are fundamentally linked to their electronic structure. Previous investigations have been carried out on molecules containing lanthanide ions, i.e. terbium acetylacetonate ($Tb(acac)_3$),[9] for the applications in organic light-emitting diodes (OLEDs). Specifically, for Ln^{3+} coordination compounds featuring f-f transitions, the 4f-shell of Ln^{3+} is effectively shielded.[10]. This leads to only a few hundred cm^{-1} energy differences among various electronic states with same J value.[10] This characteristic contributes to the emergence of sharp emission bands.[10]

Magnetic properties emerge in these compounds also due to the open-shell electronic structures, rendering them promising candidates for single-molecule magnets (SMMs). SMMs are molecules showing slow magnetic relaxation and potentially can be used in quantum information storage and processing.[5] The pioneering SMM, identified by Sessoli *et al.*,[11,12] is a Mn_{12} complex ($Mn_{12}O_{12}(O_2CR)_{16}(H_2O)_4$) featuring a magnetic assembly of eight Mn^{3+} (S=2) and four Mn^{4+} (S=3/2) centers.[13] These Mn ions couple to a total spin S=10 ground state[11] and the complex exhibits slow magnetic relaxation below 4 K.[12] Years of research have led to the synthesis of new SMMs, setting new benchmarks for magnetic reversal barriers and the blocking

temperatures at which open magnetic hysteresis is observed. The current record-holder is a mixed-valence dilanthanide complex $(Cp^{iPr5})_2Dy_2I_3$ (Cp^{iPr5}: pentaisopropylcyclopentadienyl), reported by Gould *et al.*,[14] showcases a magnetic reversal barrier of 2347 K and exhibits open hysteresis up to 72 K. This marks a significant advancement in the field of molecular magnetism.

Significant challenges arise in accurately describing the electronic structure of open-shell molecules, especially when metal-metal or metal-ligand interactions are involved. Fortunately, advances in computational methods have provided valuable tools to address these complexities. Multireference methods such as Complete Active Space Self-Consistent Field (CASSCF) has become a standard approach to provide wave functions that capture the multireference nature of open-shell transition metal and lanthanide ions. For lanthanide ions, the relativistic effects play a crucial role, making the inclusion of spin-orbit coupling (SOC) necessary, particularly when magnetic properties are concerned.[15] Consequently, the primary methodology employed in this thesis is Complete Active Space Spin-Orbit Configuration Interaction (CASOCI),[16] which is chosen to obtain electronic states that incorporate SOC into multireference wave functions.

The aim of this thesis is to calculate the optical and magnetic properties of compounds containing open-shell 3d or 4f ions utilizing quantum chemical methods. The objective is to provide theoretical insights for the interpretation and prediction of absorption and emission spectra as well as magnetic measurements in both molecular and lanthanide oxide systems. This thesis is organized as follows:
The necessary theoretical background is given in Chapter 2. Here, both single and multireference methods applied in this thesis are introduced. In Chapter 3, a series of lanthanide-coinage metal complexes were investigated for possible metal-metal interactions and their optical properties. Chapter 4 focuses on the magnetic properties. Calculations of a series of mononuclear and dinuclear lanthanide sandwich complexes, as well as a trinuclear ion complex are presented. A main focus lies on intramolecular interactions. Chapter 5 aims to employ a molecular approach, utilizing an embedded cluster model, to investigate the electronic structures of lanthanide oxides. This methodological framework is intended to elucidate the optical and magnetic properties of lanthanide oxides at an *ab initio* level, offering insights into possible functional characteristics of a complicated high-entropy oxide (HEO) system. Finally, the main conclusions of this thesis are summarized in Chapter 6.

2 Theoretical background

This chapter aims to introduce the theoretical background for the methods used in this thesis. In this work, the focus lies on the applications of the methods, rather than on the implementation. Therefore, only the fundamental concepts are presented. A more extensive introduction could be found in textbooks.[17–20] The details of the implementation can be found in references.[16,21]

First, single reference methods are introduced in section 2.1.1. Then, these concepts are extended to multireference methods in section 2.1.2. The differences between the two approaches are discussed in section 2.1.3. Section 2.2 provides an introduction to the necessary considerations to describe the electronic energies of 3d and 4f compounds. Section 2.3 introduces the main program that is used in this thesis to calculate the magnetic and optical properties that is developed and implemented by Dr. Bodenstein.[16,21]

2.1 Electronic Structure Methods: Single and Multi-Reference

2.1.1 General Hartree-Fock Method

Under the Born-Oppenheimer Approximation, the time-independent electronic Schrödinger equation can be written as

$$\hat{H}_\mathrm{e} \left|\Psi\right\rangle = E \left|\Psi\right\rangle \tag{1}$$

where Ψ is the electronic wave function and E is the total electronic energy.[17] Within the Hartree Fock approximation, the ground state electronic wave function is represented by one single Slater Determinant (SD). For the general case of an

N-electron system, the SD is given as

$$\Psi_{SD} = \frac{1}{\sqrt{N!}} \begin{vmatrix} \chi_i(x_1) & \chi_j(x_1) & ... & \chi_k(x_1) \\ \chi_i(x_2) & \chi_j(x_2) & ... & \chi_k(x_2) \\ \vdots & \vdots & \ddots & \vdots \\ \chi_i(x_N) & \chi_j(x_N) & ... & \chi_k(x_N) \end{vmatrix} \tag{2}$$

Where χ_i is the the spin orbital and x_N indicates both the space and spin coordinates. A shorthand notation of a normalized SD can be written as

$$\Psi = |\chi_i \chi_j \cdots \chi_k\rangle \tag{3}$$

The total electronic energy of a SD has the form of

$$E[\Psi] = \frac{\langle\Psi|\hat{H}|\Psi\rangle}{\langle\Psi|\Psi\rangle} \geq E_0 \tag{4}$$

which, according to the variational principle, gives the lowest possible energy E_0 for an optimal set of orbitals and the basis set limit. By minimizing the energy to obtain the optimal orbitals, the Hartree-Fock equation is derived with the form of

$$\hat{f}\,|\chi_i\rangle = \varepsilon_i\,|\chi_i\rangle \tag{5}$$

where ε_i is the orbital energy and $\hat{f}$ is the Fock operator. The Fock operator is an effective one-electron operator with the form

$$\hat{f} = \hat{h} + \sum_{j}^{N} (\hat{J}_j - \hat{K}_j) \tag{6}$$

The first term $\hat{h}$ is a one-electron operator which describes the kinetic energy of an electron and the attraction between an electron and all nuclei. The second term with the *Coulomb* and *Exchange* operators $\hat{J}$ and $\hat{K}$ includes an averaged electron-electron interaction. The *Coulomb* operator defines the electron repulsion between i-th and j-th electrons, while the *Exchange* operator describes the effect when two electrons are exchanged. The orbital energy can be written as

$$\varepsilon_i = \langle\chi_i|\hat{f}|\chi_i\rangle = h_i + \sum_{j}^{N} (J_{ij} - K_{ij}) \tag{7}$$

The electronic energy E is expressed

$$E = \sum_{i}^{N} \varepsilon_i + \frac{1}{2} \sum_{i,j}^{N} (J_{ij} - K_{ij}) \tag{8}$$

The Coulomb and Exchange integrals over spin orbitals χ_i and χ_j are denoted as

$$\begin{aligned} J_{ij} &= (ii|jj) \\ K_{ij} &= (ij|ji) \end{aligned} \tag{9}$$

2.1.1.1 Restricted Hartree-Fock (RHF) and The Roothaan Equation

In a closed-shell Hartree-Fock scheme, the molecular system has an even number of electrons and each spacial orbital $\{\psi_a | a = 1, 2, ..., N/2\}$ is doubly occupied. A restricted set of spin orbitals can be expressed with spacial orbitals

$$\chi_i(x) = \begin{cases} \psi_i(\mathbf{r})\alpha(\omega) = \psi_i \\ \psi_i(\mathbf{r})\beta(\omega) = \bar{\psi}_i \end{cases} \tag{10}$$

The ground state of a closed-shell SD can be written as

$$\Psi_{RHF} = |\psi_1 \bar{\psi}_1 ... \psi_p \bar{\psi}_p ... \psi_{N/2} \bar{\psi}_{N/2}\rangle \tag{11}$$

The converted spacial orbital Fock operator of a closed-shell system can be written as

$$\hat{f} = \hat{h}_p + \sum_{q}^{N/2} (2\hat{J}_q - \hat{K}_q) \tag{12}$$

The closed-shell spacial orbital Hartree-Fock equation can be written as:

$$\hat{f} \, |\psi_p\rangle = \varepsilon_p \, |\psi_p\rangle \tag{13}$$

With the closed-shell SD Ψ_{RHF}, the Hartree-Fock energy can be written as

$$E_{RHF} = 2 \sum_{p}^{N/2} h_p + \sum_{p,q}^{N/2} (2J_{pq} - K_{pq}) \tag{14}$$

However, it is not practical to solve the eigenvalue problem with an infinite set of orbitals numerically. It has been shown by Roothaan[22] that by using a set of known spatial basis functions to express the molecular orbitals (MOs), the equation can be converted into a matrix eigenvalue problem, which can be solved iteratively. A set of spatial basis functions $\{\phi_\mu(\mathbf{r})|\mu = 1, 2, ..., K\}$ is introduced and the MOs are represented by the linear expansion of ϕ_μ.

$$\psi_i = \sum_{\mu=1}^{K} C_{\mu,i}\phi_\mu \quad i = 1, 2, ..., K \tag{15}$$

By substituting the ψ_a by the linear expansion ψ_i in restricted Hartree-Fock equation (13) and introducing the *overlap matrix* $\mathbf{S}$ and *Fock matrix* $\mathbf{F}$, the integrated Hartree-Fock equation can be written as

$$\sum_\mu \boldsymbol{F}_{\mu\nu}\boldsymbol{C}_{\mu i} = \varepsilon_i \sum_\mu \boldsymbol{S}_{\mu\nu}\boldsymbol{C}_{\mu i} \quad i = 1, 2, ..., K \tag{16}$$

The *density matrix* is defined as

$$P_{\mu\nu} = 2\sum_p^{N/2} C_{\mu p}C_{\nu p}^* \tag{17}$$

The result is the Roothaan equation[22] which can be written in the more concise form of

$$\boldsymbol{FC} = \boldsymbol{SC\varepsilon} \tag{18}$$

where the *overlap matrix* $\mathbf{S}$ has the matrix elements

$$\boldsymbol{S}_{\mu\nu} = \int d\boldsymbol{r}\phi_\mu^*\phi_\nu \tag{19}$$

and the *Fock matrix* $\mathbf{F}$ has the elements of

$$\boldsymbol{F}_{\mu\nu} = \int d\boldsymbol{r}\phi_\mu^*\boldsymbol{f}\phi_\nu \tag{20}$$

2.1.1.2 Unrestricted Hartree-Fock (UHF) and The Pople-Nesbet Equations

In RHF, the number of electrons is even and the spacial orbitals are the same for $\alpha(\omega)$ and $\beta(\omega)$. An open-shell system, however, can have an odd number of electrons. In order to solve the open-shell problem, unrestricted Hartree-Fock (UHF) can be

applied. In UHF, the spacial orbitals of α and β spins are allowed to differ. The unrestricted spin orbitals are given in the form

$$\chi_i(x) = \begin{cases} \psi_i^\alpha(\mathbf{r})\alpha(\omega) = \psi_i^\alpha \\ \psi_i^\beta(\mathbf{r})\beta(\omega) = \psi_i^\beta \end{cases} \tag{21}$$

The unrestricted SD can be written as

$$\Psi_{UHF} = |\psi_1^\alpha \psi_1^\beta ... \psi_{N^\alpha}^\alpha \psi_{N^\beta}^\beta\rangle \tag{22}$$

The unrestricted Hartree-Fock equation can be written with α and β spin orbitals

$$\begin{aligned} \hat{f}_\alpha |\psi_i^\alpha\rangle &= \varepsilon_i^\alpha |\psi_i^\alpha\rangle \\ \hat{f}_\beta |\psi_i^\beta\rangle &= \varepsilon_i^\beta |\psi_i^\beta\rangle \end{aligned} \tag{23}$$

The Coulomb interaction doesn't change between different spins, while the Exchange interaction is only non-zero to electrons with the same spin. Therefore, the unrestricted Fock operators can be reformulated from the restricted Fock operator for α and β spins, respectively:

$$\begin{aligned} \hat{f}^\alpha &= \hat{h} + \textstyle\sum_j^{N^\alpha}(\hat{J}_j^\alpha - \hat{K}_j^\alpha) + \sum_j^{N^\beta} \hat{J}_j^\beta \\ \hat{f}^\beta &= \hat{h} + \textstyle\sum_j^{N^\beta}(\hat{J}_j^\beta - \hat{K}_j^\beta) + \sum_j^{N^\alpha} \hat{J}_j^\alpha \end{aligned} \tag{24}$$

The total unrestricted electronic energy can be expressed as

$$E_{UHF} = \sum_p^{N^\alpha} h_p + \sum_p^{N^\beta} h_p + \frac{1}{2}\sum_p^{N^\alpha}\sum_q^{N^\alpha}(J_{pq}^{\alpha\alpha} - K_{pq}^{\alpha\alpha}) + \frac{1}{2}\sum_p^{N^\beta}\sum_q^{N^\beta}(J_{pq}^{\beta\beta} - K_{pq}^{\beta\beta}) + \sum_p^{N^\alpha}\sum_q^{N^\beta} J_{pq}^{\alpha\beta} \tag{25}$$

In order to solve the UHF equation, a set of basis functions is introduced as in the RHF scenario. The Pople-Nesbet[23] equations are then derived as an analogue to the Roothaan equation

$$\begin{aligned} \boldsymbol{F^\alpha C^\alpha} &= \boldsymbol{S C^\alpha \varepsilon^\alpha} \\ \boldsymbol{F^\beta C^\beta} &= \boldsymbol{S C^\beta \varepsilon^\beta} \end{aligned} \tag{26}$$

2.1.1.3 Restricted Open-shell Hartree-Fock (ROHF)

An alternative method to treat open-shell system is the Restricted Open-shell Hartree Fock (ROHF).[24] In the frame of ROHF, the total wave function is a sum of several antisymmetrized products, each of which consists of the doubly occupied closed-shell orbitals ψ_c and partially occupied open-shell orbitals ψ_o.[24]

$$\psi_i = (\psi_c, \psi_o) \tag{27}$$

The ROHF energy expectation value consist of three parts, the first two terms correspond to the close-shell energy, the third and fourth terms are the open-shell energy. Finally, the last term represents the coupling energy between the closed- and open-shells.[24]

$$\begin{aligned} &E_{ROHF} = 2\sum_k h_k + \sum_{kl}(2J_{kl} - K_{kl}) + \\ &f[2\sum_m h_m + f\sum_{mn}(2aJ_{mn} - bK_{mn}) + \sum_{km}(2J_{km} - K_{km})] \end{aligned} \tag{28}$$

Here, indices k and l are for closed-shell orbitals, m and n are for open-shell orbitals, and i and j are for either sets. f is the fractional occupational number of the open-shell which equals to the number occupied open-shell orbitals over the total number of open-shell orbitals.[24] a and b are parameters corresponding to specific occupations and they are also known as Roothaan parameters.[24]
The *Coulomb* and *Exchange* coupling operators are defined for closed- and open-shells, respectively. The total *Coulomb* and *Exchange* operators $\hat{J}$ and $\hat{K}$ can be represented as a sum of closed- and open-shell operators.[24]

$$\begin{aligned} \hat{J} &= \hat{J}_c + \hat{J}_o = \sum_k J_k + f\sum_m J_m \\ \hat{K} &= \hat{K}_c + \hat{K}_o = \sum_k K_k + f\sum_m K_m \end{aligned} \tag{29}$$

The Fock operators of closed- and open-shells can be written with the help of two hermitian *Coulomb* and *Exchange* operators $\hat{L}$ and $\hat{M}$,

$$\begin{aligned} \hat{f}_c &= \hat{h} + 2\hat{J}_c - \hat{K}_c + 2\hat{J}_o - \hat{K}_o + 2\alpha\hat{L}_o - \beta\hat{M}_o \\ \hat{f}_o &= \hat{h} + 2\hat{J}_c - \hat{K}_c + 2a\hat{J}_o - b\hat{K}_o + 2\alpha\hat{L}_o - \beta\hat{M}_o \\ &\text{with} \quad \alpha = \tfrac{1-a}{1-f} \qquad \beta = \tfrac{1-b}{1-f} \end{aligned} \tag{30}$$

which are are associated with orbitals ψ_i with the form of

$$\begin{aligned}\hat{L}_i\psi &= \langle\psi_i|\hat{J}_o|\psi\rangle\,\psi_i + \langle\psi_i|\psi\rangle\,\hat{J}_o\psi_i \\ \hat{M}_i\psi &= \langle\psi_i|\hat{K}_o|\psi\rangle\,\psi_i + \langle\psi_i|\psi\rangle\,\hat{K}_o\psi_i\end{aligned} \tag{31}$$

The restricted open-shell Hartree-Fock equation can be expressed in the same form as eq. 5 but with the total Fock operator as a sum of closed- and open-shell Fock operators

$$\hat{f} = \hat{f}_c + \hat{f}_o \tag{32}$$

Identifying the Roothaan Parameters of various electron occupations is essential for ROHF calculations, although this task is not straightforward. The energy expression of the open-shell can be written as

$$E_o = \sum_m 2f_m h_m + \sum_{mn} 2f_m f_n (2a_{mn}J_{mn} - b_{mn}K_{mn}) \tag{33}$$

where h_{mm} is the one-electron integral, J_{mn} and K_{mn} are two-electron integrals, f_m and f_n are the fractional occupation numbers of orbitals ψ_m and ψ_n. The calculated Roothaan parameters[25] used for this thesis are given in Appendix A Table A1. To calculate Roothaan parameters, the one- and two-electron integrals are constructed based on an averaged weight of each SD. Orbitals belonging to the same occupations are grouped into one shell. The Roothaan parameters of each pair of orbitals ψ_m and ψ_n can be calculated subsequently from the two-electron integrals and occupation numbers of corresponding orbitals by

$$\begin{aligned}a &= \tfrac{J_{mn}}{2f_m f_n} \\ b &= -\tfrac{K_{mn}}{f_m f_n}\end{aligned} \tag{34}$$

2.1.2 Complete Active Space Self-Consistent Field

In this section the Complete Active Space Self-Consistent Field (CASSCF)[26] method which incorporates the static correlation is introduced. Static correlation concerns the coupling between different electronic states, in which electrons are allowed to avoid one another by occupying different orbitals. It is particularly important for systems with quasi-degenerate electronic states, such as Ln^{3+} coordination compounds.

In the HF method, only one SD is considered to construct the trial wave function. An

intuitive way to improve is to take a trial wave function as a linear combination of many SDs. Full Configuration Interaction (FCI)[27] is an approach that considers all possible excited determinants to construct the total wave function. For an N-electron system with 2K spin orbitals, the number of SDs needed for full CI is $\binom{2K}{N}$, which makes full CI unfeasible even for small systems.[18] E. Rossi *el al.* reported a full CI calculation of N_2 molecule using an ANO [4s3p1d] basis set, which gives a CI space of 9.68×10^9 symmetry-adapted Slater determinants.[28] It is possible to truncate full CI by allowing only excitation in a chosen range of orbitals. In CASSCF the truncation is done by allowing excitations only within the active space. Molecular orbitals are divided into three sub-spaces, the inactive, active and virtual spaces (Figure 1). While the orbitals in the inactive space are all doubly occupied and unoccupied in the virtual space, in the active space all the possible configurations are considered.

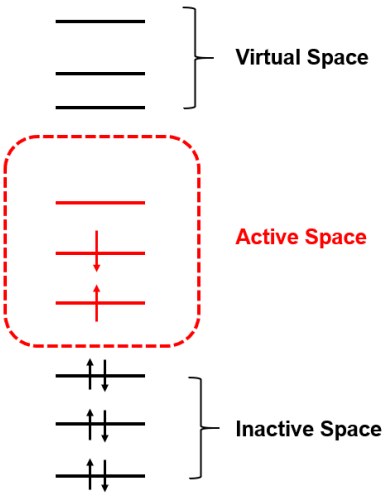

Figure 1: The illustration of the CASSCF orbital partitions.

The CASSCF wave function is the linear combination of SDs corresponding to all configurations in the active space where c_n is the CI coefficient

$$\Psi_{CAS} = \sum_n c_n \Phi_n \tag{35}$$

To optimize the CASSCF wave function means to optimize both CI coefficients and the orbitals. The orbitals are optimized by satisfying the Brillouin condition[29] and coefficients are optimized via the variational principle.

The CASSCF implementation used in this thesis is from Meier and Staemmler[30]

in which the Brillouin condition is modified such that three types of singly excitation, namely, inactive-active, active-virtual and inactive-virtual excitations are considered.[31] The matrix elements of the ground state and singly excited state should be zero in the modified Brillouin condition

$$B_{pq} = \langle\psi_0|\hat{H}|(\psi_{pq} - \psi_{qp})\rangle >= 0 \tag{36}$$

where ψ_0 is the ground state wave function and ψ_{pq} is the normalized singly excited wave function. The modified Brillouin condition can be expressed with the two operators $\hat{F}^I$ and $\hat{G}^A$[30], where the two operators in the forms of

$$\begin{aligned} \hat{F}^I_{pq} &= \hat{h}_{pq} + \textstyle\sum_i 2(pq|ii) - (pi|qi) \\ \hat{G}^A_{pq} &= \textstyle\sum_{tu} \gamma_{tu}(pq|tu) - \frac{1}{2}(pt|qu) \end{aligned} \tag{37}$$

Here, indices p, q, r and s are for all electrons, i, j, k, l are for electrons in the inactive space, t, u, v and w are for electrons in the active space and a, b, c and d are for electrons in virtual space. The three types of matrix elements can be expressed as[30]

$$\begin{aligned} &inactive(i) \rightarrow virtual(a) \\ &\quad B_{ai} = \tfrac{1}{\sqrt{2}}(2\hat{F}^I_{ai} + 2\hat{G}^A_{ai}) \\ &active(t) \rightarrow virtual(a) \\ &\quad B_{at} = \tfrac{1}{\sqrt{\gamma_{tt}}}(\textstyle\sum_u \gamma_{tu}\hat{F}^I_{au} + 2\sum_{uvw} \Gamma_{tuvw}(au|vw)) \\ &inactive(i) \rightarrow active(t) \\ &\quad B_{ti} = \tfrac{1}{\sqrt{2-\gamma_{tt}}}(2\hat{F}^I_{ti} + 2\hat{G}^A_{ti} - \textstyle\sum_u \gamma_{tu}\hat{F}^I_{ui} - 2\sum_{uvw} \Gamma_{tuvw}(iu|vw)) \end{aligned} \tag{38}$$

Here, γ and Γ are first- and second-order reduced density matrices.[30] A matrix $\boldsymbol{B}$ is defined with the matrix elements from eq. 38 as off-diagonal elements. A CASSCF calculation goes through macro-iterations and micro-iterations. In a macro-iteration, a CI calculation is done in the active space, as well as the construction of density matrices and operators. In a micro-iteration, $\boldsymbol{B}$ is diagonalized and new $\boldsymbol{B'}$ is constructed.

The choice of active orbitals is crucial in CASSCF. Ideally, all the valence orbitals should be included in the active space. However, the active space can easily become unmanageably large. For compounds containing 3d and 4f open-shell ions, it is neces-

sary to include all 3d and 4f orbitals in the active space. In practice, both ROHF and UHF can provide good starting orbitals for CASSCF calculations.

2.1.3 Exchange Coupling in a H_2 Model

The advantages of using multi-reference methods in a weakly coupled bimetallic lanthanide or transition metal complex can be demonstrated with a simple example of the H_2 dissociation problem. This scenario, where the two hydrogen atoms are at a significant distance from each other, serves as an analog for bimetallic complexes. In such complexes the metal centers weakly couple with each other and the orbitals are semi-localized on each metal center.[32] Such orbitals that are not strictly orthogonal are also known as non-orthogonal magnetic orbitals (NMOs) whereas orthogonal magnetic orbitals (OMOs) can be obtained from NMOs through a Löwdin procedure.[33] The H_2 at large distance mirrors such a weakly exchange-coupled bimetallic complex.

Figure 2 shows the potential energy curve of H_2 calculated with a def2-TZVP basis set. At equilibrium, RHF shows a good agreement with the CASSCF dissociation energy. However, when the H-H distance is at 10 Bohr, the RHF method predicts a dissociation energy that is significantly higher than 0. In contrast, UHF predicts the energy to be around 0 at the bond breaking distance but gives a qualitatively wrong dissociation energy at equilibrium.

UHF fails at equilibrium because of the same reason RHF fails in the bond breaking region. A single reference wave function can not describe the potential energy curve. Instead, a multi-reference wave function is required. If only the 1s orbitals of hydrogen A and B (χ_A and χ_B) are considered, the bonding σ_g and anti-bonding σ_u orbitals are

$$\begin{aligned} \sigma_g &= \tfrac{1}{\sqrt{2}}(\chi_A + \chi_B) \\ \sigma_u &= \tfrac{1}{\sqrt{2}}(\chi_A - \chi_B) \end{aligned} \tag{39}$$

For RHF, the two electrons will be in the bonding orbitals and the wave function has the form

$$\begin{aligned} \Psi_{RHF} &= |\sigma_g \bar{\sigma}_g| \\ &= \tfrac{1}{2}(|\chi_A \bar{\chi}_A| + |\chi_B \bar{\chi}_B| + |\chi_A \bar{\chi}_B| + |\chi_B \bar{\chi}_A|) \end{aligned} \tag{40}$$

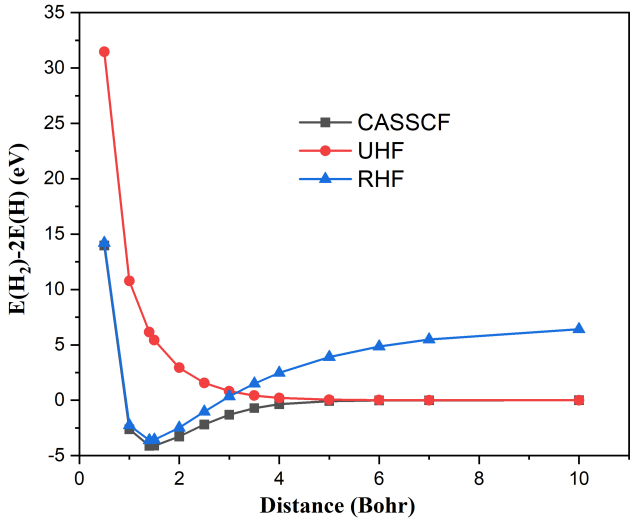

Figure 2: The H_2 dissociation energy (in Hartree) calculated by RHF, UHF and CASSCF methods with def2-TZVP basis set.

The first two terms are the ionic contributions that represent the state of both electron at one site with opposite spins. The other terms are the covalent contributions that represent the state where one electron is at one site. Both ionic and covalent occupancies contribute equally to the RHF wave function. This clearly does not hold true in dissociation region because the system should be treated as two separate hydrogen atoms. The CASSCF(2,2) wave function is a linear combination of both the bonding and anti-bonding orbitals with coefficients and can be expanded as

$$\begin{aligned} \Psi_{CAS} &= c_g \left|\sigma_g \bar{\sigma}_g\right| + c_u \left|\sigma_u \bar{\sigma}_u\right| \\ &= (c_g + c_u)(\left|\chi_A \bar{\chi}_A\right| + \left|\chi_B \bar{\chi}_B\right|) + (c_g - c_u)(\left|\chi_A \bar{\chi}_B\right| + \left|\chi_B \bar{\chi}_A\right|) \end{aligned} \tag{41}$$

When the CI coefficients are optimized, the ionic contribution becomes negligible at dissociation. A multi-reference wave function gives a good description of H_2 at both equilibrium and dissociation.

2.2 3d and 4f Coordination Compounds

3d and 4f coordination compounds containing open-shell ions exhibit appealing optical and magnetic properties and have a wide range of applications such as molecular

imaging,[34], single-molecule magnetism[35] and catalysis.[3] To predict the magnetic and optical properties, a good description of electronic energies is necessary. To achieve this goal, it is essential to employ an appropriate quantum chemical electronic structure method. Furthermore, the consideration of major contributions, including Spin-Orbit Coupling (SOC), ligand field (LF) splitting, and the Zeeman effect, is crucial.

2.2.1 Spin-Orbit Coupling

Spin-Orbit can be interpreted as the spin of electrons interacting with the orbital angular momentum in the electrostatic field generated by the nucleus. This results in a shift of energies which is detectable in atomic spectra. In order to determine the energy shift and splitting, the spin-orbit coupled wave function as well as the SOC Hamiltonian need to be obtained.

2.2.1.1 Total Angular Momentum

The orbital momentum coupled with spin gives the total angular momentum j. The possible values of j are

$$\begin{aligned} j &= l+s, l+s-1, ..., |l-s| \\ m_j &= m_l + m_s \end{aligned} \tag{42}$$

The eigenfunction of the total angular momentum can be expressed as the linear expansion of the uncoupled tensor product basis with Clebsch-Gordan Coefficients. Clebsch-Gordan Coefficients are tabularized in the Particle Data Group.[36] The uncoupled states are given as $|l, m_l\rangle \otimes |s, m_s\rangle$. The coupled eigenstates can be expressed as such

$$|j, m_j\rangle = \sum_{m_l} \sum_{m_s} |l, m_l, s, m_s\rangle \langle l, m_l, s, m_s | j, m_j\rangle \tag{43}$$

here $\langle l, m_l, s, m_s | j, m_j\rangle$ is the Clebsch-Gordan Coefficient.

2.2.1.2 Russel-Saunders Coupling

One way to incorporate SOC in a many-electron system is by Russel-Saunders Coupling[37] (or LS-coupling), which is considered when the SOC is weaker than electron-electron interaction. In the Russel-Saunders Coupling scheme, the electrons individual spin s and orbit momenta l couple first to S and L, respectively. Then, L

and S couple to the total angular momentum J of the N-electron atom.

$$\begin{aligned} &\hat{\boldsymbol{L}} = \textstyle\sum_i^N \hat{\boldsymbol{l}}_i \quad \hat{\boldsymbol{S}} = \textstyle\sum_i^N \hat{\boldsymbol{s}}_i \\ &J = L+S, L+S-1, ..., |L-S| \end{aligned} \tag{44}$$

The quantum state can be represented by a term symbol

$$^{2S+1}L_J \tag{45}$$

where $2S+1$ is the spin multiplicity, L uses the symbols $[S, P, D, F, G, H, I...]$ corresponding to $L = [0, 1, 2, 3, 4, 5, 6...]$. The term symbol of the ground state can be determined following Hund's rule.[38] With the largest possible S value, the ground state can be obtained by maximizing L. The smallest value for J corresponds to the ground state for less than half-filled shells, and vice versa for more than half-filled shells. The angular momentum operators have the relation of

$$\hat{\boldsymbol{L}} \cdot \hat{\boldsymbol{S}} = \frac{1}{2}(\hat{\boldsymbol{J}}^2 - \hat{\boldsymbol{L}}^2 - \hat{\boldsymbol{S}}^2) \tag{46}$$

The energy shift of a state can be expressed with quantum numbers

$$\begin{aligned} &\hat{\boldsymbol{L}} \cdot \hat{\boldsymbol{S}} \, |L, M_L, S, M_S\rangle = E_{SO} \, |L, M_L, S, M_S\rangle \\ &E_{SO} = \tfrac{1}{2}\lambda(J(J+1) - L(L+1) - S(S+1))\hbar^2 \end{aligned} \tag{47}$$

where λ is a constant depends on the element of interest. The general form of non-relativistic one-electron Spin-Orbit coupling Hamiltonian can be written as

$$\hat{h}_{SOC} = \zeta(r)\hat{\boldsymbol{l}} \cdot \hat{\boldsymbol{s}} \tag{48}$$

where the one-electron factor $\zeta(r)$ has the form of

$$\zeta(r) = \frac{\alpha^2}{2}\frac{1}{r}\frac{\partial V}{\partial r} \tag{49}$$

Here $\alpha \approx \frac{1}{137}$ is the fine structure constant, V is the Coulomb potential due to the nucleus.[39]

2.2.1.3 Spin-Orbit Coupling Hamiltonian

An electron possesses a magnetic dipole moment $\vec{\mu} = \frac{e}{m_e}\vec{s}$ due to its spin. Because of special relativity, an electron also experiences a magnetic field $\boldsymbol{B} = \frac{\vec{v}\times\vec{E}}{c^2}$ (here $\boldsymbol{B}$ indicates it's a vector) while moving in the electric field generated by the nucleus. The potential of an electron in a magnetic field has the form of $\hat{H}_L = -\vec{\mu}\boldsymbol{B}$. However, one needs to further include relativistic correction of Thomas precession into the Hamiltonian.[40] Eventually, the one-electron Spin-Orbit Hamiltonian with its relativistic correction can be written

$$\hat{h}_{SOC}^{rel} = \frac{Ze^2}{8\pi\epsilon_0 m_e^2 c^2}\frac{\hat{\boldsymbol{l}}\cdot\hat{\boldsymbol{s}}}{r^3} \tag{50}$$

The generalization of the many-electron Spin-Orbit Hamiltonian is not trivial because the electron interaction and relativistic correction need to be included. The many-electron Spin-Orbit Hamiltonian, namely the Breit-Pauli Hamiltonian, which includes relativistic correction and electron-electron interaction was first derived by Breit[41–43] and Pauli[44] and has the form of

$$\begin{aligned}
\hat{H}_{SOC} &= \hat{H}_{SOC}^{(1)} + \hat{H}_{SOC}^{(2)} \\
\hat{H}_{SOC}^{(2)} &= \hat{H}_{SsO} + \hat{H}_{SoO} \\
\hat{H}_{SOC}^{(1)} &= \tfrac{\alpha^2}{2}\textstyle\sum_{iA} Z_A \frac{\hat{\boldsymbol{s}}_i\hat{\boldsymbol{l}}_{iA}}{r_{iA}^3} \\
\hat{H}_{SsO} &= -\tfrac{\alpha^2}{2}\textstyle\sum_i\sum_{j\neq i}\frac{\hat{\boldsymbol{s}}_i\hat{\boldsymbol{l}}_{ij}}{r_{ij}^3} \\
\hat{H}_{SoO} &= -\tfrac{\alpha^2}{2}\textstyle\sum_i\sum_{j\neq i}\frac{2\hat{\boldsymbol{s}}_j\hat{\boldsymbol{l}}_{ij}}{r_{ij}^3}
\end{aligned} \tag{51}$$

where i, j are the indices for electrons and A for nucleus. $\hat{H}_{SOC}^{(1)}$ and $\hat{H}_{SOC}^{(2)}$ are the one and two-electron contributions. The one-electron contribution is a summation of the one-electron spin-orbit Hamiltonian over all electrons. The two-electron contribution is composed of two terms $\hat{H}_{SsO}$ and $\hat{H}_{SoO}$, which account for the spin-same-orbit and spin-other-orbit interactions,[45] respectively.

2.2.2 Ligand Field Theory

For coordination compounds, the 3d and 4f orbital energy degeneracy of the free ions is lifted when ligands are present. To describe the energy splitting, ligand field theory[46] (LFT) was introduced combining crystal field theory and molecular orbital

theory.[47] Crystal field theory was introduced by Bethe[48] and Van Vleck,[49] which considers how the electrostatic potential of ligands influences orbitals on the metal center. In crystal field theory, the ligands are either ions or have lone pair electrons. With molecular orbital theory, the covalent bonding is considered. Electrons can occupy the molecular orbitals which combine metal and ligand orbitals.[46] One can describe the ligand field splitting with ligand field operators. The general form of one-electron ligand field operator[50] is

$$\hat{H}_{LF} = \sum_{k=0}^{\infty} \sum_{q=-k}^{+k} A_k^q r^k C_q^k(\theta, \phi) \tag{52}$$

where A_k^q is the geometrical coordination factor and C_q^k is the Racah tensor.[20] However, in practice, an effective Hamiltonian is employed to connect the *ab initio* calculation and crystal field parameters (see the section 2.3.2.1).[51]

2.2.3 SOC and LF in 3d/4f Coordination Compounds

Considering both Spin-Orbit Coupling and Ligand Field Splitting in 3d and 4f coordination compounds, two situations emerge depending on which one is more dominant. An example calculation comparing the energy scheme of d^1 and f^1 configurations in an octahedral ligand field is given in Figure 3 to clarify the different effects of LF and SOC in 3d and 4f coordination compounds.

For 3d compounds, the ligand field is the main contribution to the energy splitting. The ligand field splitting is two orders of magnitudes larger than SOC energy splitting in the $3d^1$ model complex. Conversly, SOC plays a more significant role for the $4f^1$ model complex.

The ground term of Ti^{3+} free ion is ^2D. For the model complex $[TiCl_6]^{3-}$, ^2D state splits into $^2T_{2g}$ and ^2E_g with an octahedral ligand field. When considering SOC, the $^2T_{2g}$ state further splits into E" and G". To determine the states of more complex d^n systems, Tanabe-Sugano diagrams[52–54] are good references.

The ground term of Ce^{3+} free ion is ^2F. Considering SOC, the total angular momenta J can be 7/2 and 5/2 with $^2F_{5/2}$ being the ground state. The splitting caused by SOC is 2418 cm^{-1} while the degeneracy is further lifted when the ligand field is

considered. The zero-field splitting is around 400-500 cm^{-1} for the $[CeCl_6]^{3-}$ model complex. The inclusion of SOC is particularly important for describing magnetic properties of 4f compounds since zero-field splitting is crucial for the magnetic anisotropy.

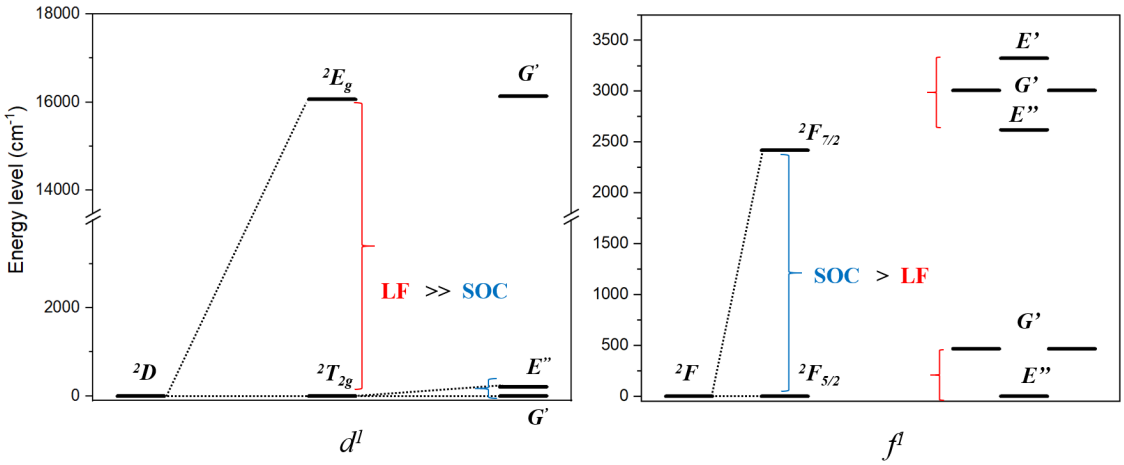

Figure 3: Calculated energy levels (in cm^{-1}) of $[TiCl_6]^{3-}$ (d^1 configuration) and $[CeCl_6]^{3-}$ (f^1 configuration). (x2c-TZVPall basis set)

2.3 Complete Active Space Spin-Orbit Configuration Interaction

In the scope of this thesis, magnetic and optical properties 3d and 4f complexes are investigated utilizing the Complete Active Space Spin-Orbit Configuration Interaction (CASOCI) program developed by Dr. Bodenstein.[16] For compounds whose magnetic and optical properties rise from partially filled 3d and 4f orbitals, a multi-reference wave function is compulsory, as well as the inclusion of SOC for a precise description of the low-lying states.

In the CASOCI program, SOC is included in the complete active space wave function obtained from CASSCF (or ROHF). The electronic structures are calculated using the program package developed in the group of Prof. Staemmler from Bochum.[30,55–58]

The CASOCI algorithm is based on the determinant-based full CI method presented by Knowles and Handy[59] and the determinant-based spin-orbit CI method introduced

by Sjøvoll, Gropen and Olsen.[60] A Block-Davidson[61] Algorithm was implemented for the CI matrix diagonalization.

2.3.1 CASOCI Energy

The complete Hamiltonian implemented in CASOCI can be written as

$$\hat{H}_{\mathrm{CASOCI}} = \hat{H}_{\mathrm{BO}} + \hat{H}_{\mathrm{SOC}} + \hat{H}_{\mathrm{Zeeman}} + \hat{H}_{\mathrm{MCASCI}} \tag{53}$$

where $\hat{H}_{\mathrm{BO}}$ is the electronic Born-Oppenheimer Hamiltonian.

In order to avoid treating two-electron interaction explicitly, the spin-orbit mean-field Hamiltonian was applied to $\hat{H}_{SOC}$ instead of the Breit-Pauli Hamiltonian from eq. 51. The mean-field approximation is introduced by Heß *el al.*[62] using an effective one-electron spin-orbit operator to simplify the two-electron contribution by averaging over electrons in the valence space. The matrix elements of the spin-orbit operator between an excitation from i to j in the valence orbital space can be expressed as

$$\begin{aligned}\hat{H}^{mean-field} &= \langle i|\hat{H}^{(1)}_{SOC}|j\rangle + \tfrac{1}{2}\textstyle\sum_k n_k\{\langle ik|\hat{H}^{(2)}_{SOC}|jk\rangle \\ &- \langle ik|\hat{H}^{(2)}_{SOC}|kj\rangle - \langle ki|\hat{H}^{(2)}_{SOC}|jk\rangle\}\end{aligned} \tag{54}$$

where n_k is the fixed occupation number which is typically chosen to be p/m for p electrons in m valence orbitals.[62] $\hat{H}^{(1)}_{SOC}$ and $\hat{H}^{(2)}_{SOC}$ are the one- and two-electron spin-orbit operators from the Breit-Pauli Hamiltonian in eq. 51.

$\hat{H}_{Zeeman}$ is the Zeeman Hamiltonian which gives the energy splitting when an external homogeneous magnetic field is present. In the CASOCI approach, the magnetic field is treated in first-order perturbation theory.

$$\hat{H}_{Zeeman} = \sum_i \mu_B(\hat{\boldsymbol{l}}_i + g_e\hat{\boldsymbol{s}}_i)\boldsymbol{B} \tag{55}$$

where μ_B is the bohr magneton, $\hat{\boldsymbol{l}}_i$ and $\hat{\boldsymbol{s}}_i$ are the orbital and spin angular momentum operators for electron i and g_e=2.0023[63,64] for free electrons.

$\hat{H}_{MCASCI}$ is the modified CAS-CI Hamiltonian[65] which gives a more reasonable magnetic exchange coupling by lowering the high energy charge-transfer states in multi-center magnetic molecules.

The main application of the CASOCI program to calculate the magnetic properties of 3d and 4f (one- and multi-center) complexes including the g-tensor, zero-field splitting parameters and magnetic susceptibility. With the further development by C. Pachl,[66] the m_j compositions and oscillator strengths can also be calculated for interpreting optical spectra.

2.3.2 Spin Hamiltonian

The interpretation of experimental magnetic data is connected to *ab initio* results by the effective Hamiltonian in a model space. The spin Hamiltonian is such an effective Hamiltonian that uses the information from experiments to reproduce spectroscopic data.[67] The splitting of the ground configuration into multiplets can be described by the spin Hamiltonian.[68] A single-ion spin Hamiltonian can be written as

$$\hat{H}_{spin} = E_0 + \hat{\boldsymbol{S}}^T \boldsymbol{D} \hat{\boldsymbol{S}} + \mu_B \boldsymbol{B}^T \boldsymbol{g} \hat{\boldsymbol{S}} \tag{56}$$

where the first term is an energy shift that matches the energy of spin and microscopic Hamiltonian.[67] The second term is the zero-field splitting Hamiltonian and third term gives the Zeeman interaction in an external magnetic field. The hyperfine interaction with magnetic nuclei is not considered here because it is not implemented in the CASOCI program. Finally, with the spin Hamiltonian, the magnetic data can be extracted from the *ab initio* energies.

2.3.2.1 Zero-Field Splitting

Experimentally, zero-field splitting parameters can be determined by Electron Paramagnetic Resonance (EPR) which measures the energy differences of complexes with unpaired electrons.[69] For one magnetic center in the absence of an external magnetic field, the zero-field splitting Hamiltonian has the form of

$$\begin{aligned} \hat{H}_{ZFS} &= \hat{\boldsymbol{S}}^T \boldsymbol{D} \hat{\boldsymbol{S}} \\ &= D(\hat{\boldsymbol{S}}_z^2 - \tfrac{1}{3}S(S+1) + \tfrac{E}{D}(\hat{\boldsymbol{S}}_+^2 + \hat{\boldsymbol{S}}_-^2)) \end{aligned} \tag{57}$$

where $\boldsymbol{D}$ is a trace-less, symmetric 3 dimensional tensor. D and E are the axial and rhombic parameters for magnetic molecules[70] and can be expressed from the diagonal matrix elements of $\boldsymbol{D}$

$$\begin{aligned} D &= D_{zz} - \tfrac{1}{2}(D_{xx} + D_{yy}) \\ E &= \tfrac{1}{2}(D_{xx} - D_{yy}) \end{aligned} \tag{58}$$

D and E are axial and rhombic zero-field splitting parameters[71] that contain important information about magnetic interaction in the spin $> 1/2$ ground state and can be obtained from various experimental methods such as electronic paramagnetic resonance (EPR) measurements.[72] They are commonly used in transition metal compounds. However, for the lanthanide compounds, equivalent operators,[69] namely the Stevens Operator are used to express the zero-field splitting operators.[73] Stevens Operators were further developed by Rudowicz[74,75] as the extended Stevens Operators (ESOs). The Hamiltonian has the the form of

$$\hat{H}_{ESO} = \sum_{k} \sum_{q=-k}^{k} B_k^q \hat{\boldsymbol{O}}_k^q \tag{59}$$

where B_k^q is the interaction constant and $\hat{\boldsymbol{O}}_k^q$ is the operator equivalent (k =0, 2, 4, 6).[69] Ryabov[76] derived the general form of the operator equivalents with the total angular momentum operators

$$\hat{\boldsymbol{O}}_k^q = \frac{\alpha}{2F_{k,q}} \sum_{m=0}^{k-q} a(k,q;m)[\hat{\boldsymbol{J}}_+^q \pm (-1)^{k-q-m} \hat{\boldsymbol{J}}_-^q] \hat{\boldsymbol{J}}_z^m \tag{60}$$

where the + sign is taken when $q \geq 0$ and $-$ sign is taken when $q < 0$. $\alpha = 1$ when both k and q are even numbers.

2.3.2.2 g Matrix

As written in eq. 56, the interaction with the external magnetic field can be expressed with an effective Zeeman Hamiltonian

$$\hat{H}_{Zeeman}^{eff} = \mu_B \boldsymbol{B}^T \boldsymbol{g} \hat{\boldsymbol{S}} \tag{61}$$

The energy splitting for a pseudospin $\tilde{S} = 1/2$ in the magnetic field is

$$\Delta E = \mu_B \sqrt{\sum_{ijk} B_i g_{ik} g_{jk} B_j} \tag{62}$$

where $i, j, k \in x, y, z$. The connection to the electronic Zeeman Hamiltonian in eq. 55 is established by considering that it is the cause of the energy splitting.[77] The pseudospin spin space can be connected to the electronic states space by the invariant Abragam-Bleaney tensor.[77–79]

$$\boldsymbol{G} = \boldsymbol{g}\boldsymbol{g}^{\boldsymbol{T}} \tag{63}$$

The energy splitting can also be written with the Abragam-Bleaney tensor.[77]

$$\Delta E = \mu_B \sqrt{\sum_{ij} B_i B_j G_{ij}} \tag{64}$$

The matrix elements of G_{ij} are derived by Gerloch and McMeeking[80]

$$\boldsymbol{G}_{ij} = 2 \sum_{v} \sum_{w} \langle v | \hat{\boldsymbol{l}}_i + g_e \hat{\boldsymbol{s}}_i | w \rangle \langle w | \hat{\boldsymbol{l}}_j + g_e \hat{\boldsymbol{s}}_j | v \rangle \tag{65}$$

where w and v are the two conjugate states of the Kramers doublet. When G is diagonalized, the diagonal elements corresponds to the g-values whereas the eigenvectors are the magnetic axes.

2.3.2.3 Magnetic Susceptibility

The magnetic susceptibility (χ) of a material describes its ability to become magnetized when exposed to an external magnetic field. This property is quantitatively defined as $\chi = \frac{M}{H}$, where M is the magnetization of the material and H is the applied magnetic field. In crystalline materials, the relationship between magnetization (M) and the magnetic field (H) is not always linear or direct, as these vectors may not align perfectly.[81] Consequently, the magnetic susceptibility in such cases is more accurately represented as a tensor,

$$\boldsymbol{\chi}_{ij} = \frac{\partial \boldsymbol{M}_i}{\partial H_j} \quad (i, j \in x, y, z) \tag{66}$$

which can be calculated via

$$\boldsymbol{\chi}_{ij} = N\frac{\partial}{\partial H_j}\frac{\sum_n(-\frac{\partial E_n}{\partial H_i})exp(-\frac{E_n}{kT})}{\sum_n exp(-\frac{E_n}{kT})} \tag{67}$$

where N is the Avogadro constant and k is the Boltzmann constant. When the Zeeman splitting is small, the partial differentiation $\frac{\partial E_n}{\partial H_i}$ can be approximated by $\frac{E_n(H_i)-E_n(0)}{H_i}$. Therefore, the magnetic susceptibility can be calculated by the energy levels of the low-lying states by the form[57]

$$\boldsymbol{\chi}_{ij} = -\frac{N}{H_j}\frac{\sum_n(-\frac{E_n(H_i)-E_n(0)}{H_i})exp(-\frac{E_n(H_i)}{kT})}{\sum_n exp(-\frac{E_n(H_i)}{kT})} \tag{68}$$

where E_n is the energy of the corresponding state. The differential part from eq. 67 can also be calculated numerically.[21] Eventually, to compare with the magnetic susceptibility measured in powder samples, the diagonal elements of the tensor $\boldsymbol{\chi}$ are calculated from both methods and the arithmetic mean values are taken

$$\chi(T) = \frac{1}{3}\mathrm{Tr}(\boldsymbol{\chi}(T)) \tag{69}$$

2.3.2.4 Magnetic Coupling

With spin Hamiltonian and low-lying energy from *ab initio* calculations, the magnetic properties of single-spin center molecules can be extracted. For multi-spin-center molecules, the coupling between the spin centers also needs to be considered to correctly predict magnetic behaviour. Two types of magnetic coupling will be introduced, namely, the exchange coupling and dipolar coupling.

The exchange coupling between two spin centers A and B can be described by the Heisenberg-Dirac-van-Vleck Hamiltonian[82]

$$\hat{H}^{HDvV} = -2J_{AB}\hat{\boldsymbol{S}}_A\hat{\boldsymbol{S}}_B \tag{70}$$

here the J_{AB} is the exchange coupling constant. The energy difference between two spin states can be express with exchange coupling constant

$$\Delta E = E(S) - E(S-1) = -2J_{AB}S \tag{71}$$

When the energies of the different spin states are known, the exchange coupling constant can be calculated. The spin centers couple ferromagnetically when $J > 0$ or antiferromagnetically if $J < 0$.

In practice, determining the energies of various spin states of multi-spin-center molecules is not trivial. Single reference methods describe wave functions poorly and multi-reference methods may fail to predict the energy correctly if dynamic correlation is not considered. The Broken Symmetry (BS) approach proposed by Noodleman[83] gives a single-reference solution to calculate the exchange coupling constant. The energy of the pure highest spin state (E_{HS}) and a mixed spin state (E_{BS}) is calculated by Hartree-Fock method or Density Functional Theory. The exchange coupling constant can then be written as

$$J^{Noodleman} = -\frac{E_{HS} - E_{BS}}{S^2_{MAX}} \tag{72}$$

which is further modified by Yamaguchi *et al.*[84,85] to better describe the weak coupling regime.[86] This yields the form of

$$J^{Yamaguchi} = -\frac{E_{HS} - E_{BS}}{\langle S^2_{HS}\rangle - \langle S^2_{BS}\rangle} \tag{73}$$

The exchange coupling constants in this thesis are calculated with the Yamaguchi modification.[84,85]

A second important magnetic coupling to mention is the dipolar coupling, which occurs in molecules with highly anisotropic states. The dipolar coupling is treated as a direct coupling between two magnetic moments. The coupling energy can be written as

$$E_{dip} = \frac{\mu_0}{4\pi r^3}(\vec{\boldsymbol{\mu}}_A \cdot \vec{\boldsymbol{\mu}}_B - 3(\vec{\boldsymbol{\mu}}_A \cdot \vec{\boldsymbol{r}})(\vec{\boldsymbol{\mu}}_B \cdot \vec{\boldsymbol{r}})) \tag{74}$$

where $\vec{\boldsymbol{\mu}}$ is the magnetic moment of each center and $\vec{\boldsymbol{r}}$ is the normalized vector connecting the two spin centers. The dipolar coupling constant J_{dip} in this thesis is calculated between two highly anisotropic ground states with the form of

$$J_{dip} = -2E_{dip} \tag{75}$$

2.3.3 Transition Dipole Moment

Transition dipole moments (TDM) determine the transition probability of molecular state changes.[87] The TDM between two states i and j calculated in the dipole length form is expressed[88]

$$d_{ij} = \langle \psi_i | \hat{\mu} | \psi_j \rangle \tag{76}$$

where $\hat{\mu}$ is the position operator when the dipole length is concerned. ψ_i and ψ_j are the wave functions of i and j states. Laporte rule[89] states that for molecules with an inversion center, the transition between between two states is forbidden when the two states exhibit the same symmetry (both g or both u).[90] In this case the TDM is zero. The relation between the TDM and the optical observable oscillator strengths in the length approximation can be expressed

$$f_{ij} = \frac{2}{3}(E_j - E_i)|d_{ij}|^2 \tag{77}$$

here, E_i and E_j are the energies of corresponding states. The oscillator strengths can also be calculated with the dipole velocity expression.[88] However, in this thesis they are calculated in the dipole length expression.

3 Structural and Optical Properties of Ln-TM Complexes

3.1 Introduction

The application of the optical properties of lanthanides can be traced back to 1891, when Auer von Welsbach invented Auer-mantle composed of lanthanide oxides for the purpose of lighting.[91] Until today, lanthanide luminescence has found its applications in many fields such as light-emitting diodes (LEDs)[92] and bio-imaging.[93] Three types of electronic transitions, charge transfer transitions,[94,95] 4f-5d transitions[96] and 4f-4f transitions can contribute to lanthanide luminescence.[91] Particularly, 4f-4f transitions are responsible for the sharp emission bands in spectra.[91] In this chapter, mainly the 4f-4f transitions and charge transfer transitions were investigated.

Bi-metallic complexes are of great interest for their possible applications in improving catalytic performance and alternating photophysical properties.[8] In some cases, the metal-metal interactions play a key role in the catalytic process.[97,98] Therefore, the field of metal-metal bonding has attracted great interest[99] and complexes containing metal-metal bond have been synthesized.[100] In terms of Lanthanide-transition metal hetero-metallic complexes, short Ln-TM distances are achieved in the molecular cluster $Ce\{N[(CH_2CH_2NPiPr_2)RhCl(COD)]_3\}$.[101] Additionally, lanthanide-transition metal complexes with metal-metal interactions were also synthesized.[102] However, achieving a short lanthanide-coinage metal distance has remained a synthetic challenge.[103]

In this chapter, two hetero-bimetallic lanthanum-coinage metal (CM) compounds and a monometallic Nd complex were investigated. Here, the coinage metals are Au and Ag. They are synthesized by Dr. Dahlen from Prof. Roesky's group at Karlsruhe Institute of Technology. These hetero-bimetallic complexes utilize the PNNP ligand system N,N'-bis[(2-diphenylphosphino)phenyl]formamidinate, dpfam ligand)[104–106],

which features coordination positions for both lanthanide (hard metal) and coinage metal (soft metal)[103] as in Figure 4 (A).

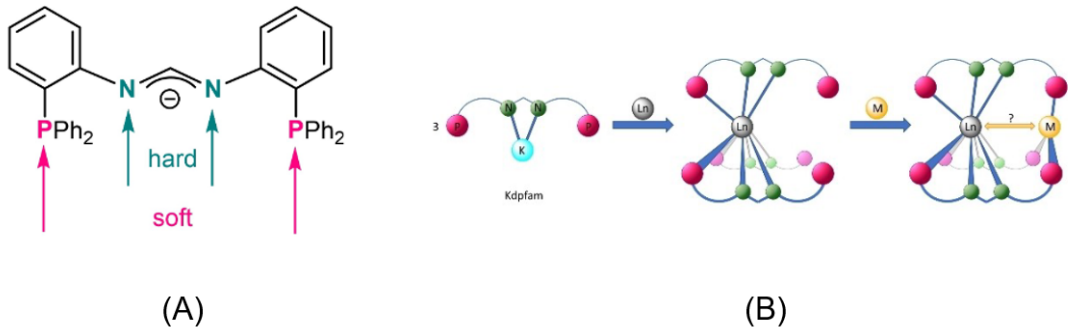

Figure 4: (A) Illustration of the dpfam ligand. (B) Schematic drawing of the synthetic approach to binuclear lanthanide/coinage metal complexes. Adapted from reference[103] Figure 1 and 3.

The Au/Ag-La complexes were constructed according to Figure 4 (B). The La atom occupies the hard metal position of three dpfam ligands, whereas the soft position is occupied by Au/Ag. The [dpfam$_3$Nd] complex features only Nd coordinating with three dpfam ligands without coinage metal.

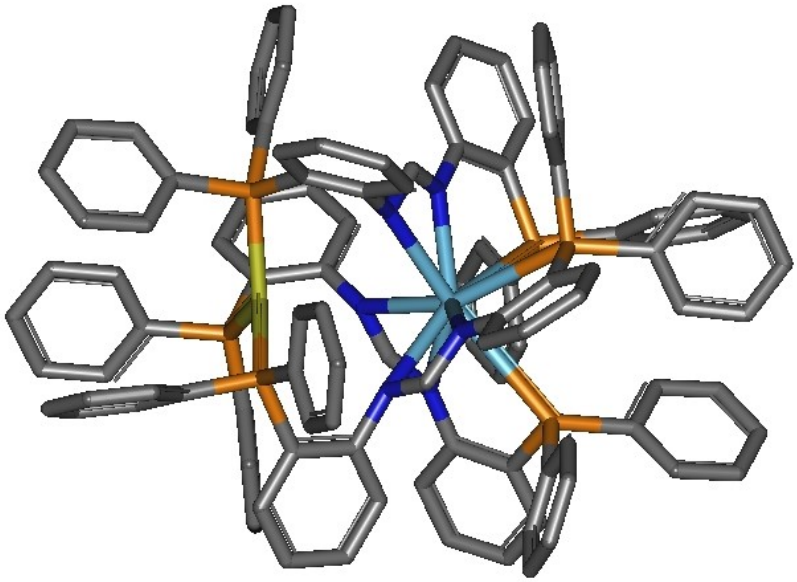

Figure 5: Illustration of complexes investigated in this section, hydrogen atoms are omitted for clarity. Grey: carbon; Orange: phosphorus; Yellow: gold/silver; Blue: nitrogen; Light blue: lanthanum/neodymium.

The Au-La and Ag-La complexes display short metal-metal distances. These complexes also exhibit photoluminescence despite the absence of f-electrons in La^{3+}. Offering an explanation for both the short metal-metal distances and the origin of the unexpected emission band is of great interest. Quantum chemical calculations were carried out to clarify possible reasons for the short metal-metal distances and to assist the interpretation of emission spectra of the Au-La, Ag-La and Nd complexes.

3.2 Computational details

Geometry optimizations were performed with Turbomole[107] at DFT level. In most calculations, the BP86 functional (BP)[108,109] was applied. Dispersion corrections were considered with Grimmes D3 correction combined with Becke-Johnson damping.[110,111] Resolution of the Identity (RI) Approximation[112,113] was applied with corresponding auxiliary basis sets.[114] Results with the def2-SVP[115] and def2-TZVP[115] basis sets were compared. In case of carbon atoms, the f-functions were removed from the def2-TZVP basis set. However, the basis set is still denoted as def2-TZVP in this chapter. For comparison, geometry optimizations were also performed with the PBE0[116,117] functional with the def2-TZVP basis set.

UV/Vis spectra of simplified model complexes were calculated with Time-Dependent Density Functional Theory (TDDFT) at PBE0/def2-TZVP level. Excitation energy and transition probabilities of the full complex Au-La wer calculated with the simplified Tamm-Dancoff Approximation (sTDA).[118]

The excitation energies of a Nd^{3+} model complex (see Figure 9) were calculated with the CASOCI program.[16]

In this section, chemical structures are visualized by VMD[119] and Gabedit[120], graphs are plotted with Origin.[121]

3.3 Geometry Optimization

Structures of Au-La and Ag-La complexes were optimized and compared. The gold/silver atom is coordinated with three P atoms, each saturated by two phenyl rings and one phenyl bridge connecting to the N atom which is coordinated with

lanthanum. The lanthanum atom is coordinated with six N and three P atoms. All P atoms are saturated by three phenyl rings. For N atoms, three of them are connected to the phenyl bridge, while the other three are linked to them via methanetriyl groups (see Figure 5). These three N atoms are coordinating with one of the phenyl groups from triphenylphosphine.

Table 1 and 2 list the La-CM distances and the metal-ligand distances of the first coordination sphere within the structures optimized at different levels. In general, the geometry optimized under PBE0-D3(BJ)/def2-TZVP shows the best agreement with the crystal structure. The calculated La-CM distances are 3.990 and 4.133 Å for the Ag-La and Au-La complexes, respectively, with a 0.055/0.11 Å difference compared to the experimental values. The distances are longer than the sum of ionic radii (2.322 and 2.542 Å for Ag^{+}-La^{3+} and Au^{+}-La^{3+}), which indicates that there is no direct bond between gold/silver and the lanthanum ion.

For the BP functional with different basis sets def2-SVP and def2-TZVP, the Au-La distance optimized with D3(BJ) dispersion correction is shortened by 0.5 Å compared to the same case without dispersion correction. Under BP/def2-SVP level, the calculated Au-La distances with and without dispersion correction are 3.900 and 4.453 Å respectively. For BP/def2-TZVP, the distances are 3.968 Å with dispersion and 4.534 Å without. The La-CM distances are slightly shorter with smaller basis set. The structures optimized without dispersion correction exhibit significantly longer La-CM distances compared to the experimental values.

In terms of the distance between metals and coordinating N or P atoms, the changes caused by different functionals or basis sets are rather insignificant. The results showed a good agreement with the experiment.

		def2-SVP		def2-TZVP		
Distance (Å)	Exp.	BP-D3(BJ)	BP	BP-D3(BJ)	BP	PBE0-D3(BJ)
Ag-La	4.045	3.851	4.248	3.917	4.305	3.99
Ag-P3	2.486	2.462	2.519	2.444	2.506	2.478
Ag-P4	2.483	2.466	2.523	2.446	2.507	2.476
Ag-P5	2.491	2.472	2.524	2.447	2.508	2.48
La-P6	3.411	3.226	3.493	3.236	3.501	3.293
La-P7	3.365	3.216	3.481	3.233	3.490	3.282
La-P8	3.433	3.236	3.494	3.247	3.501	3.304
La-N9	2.663	2.668	2.735	2.679	2.747	2.684
La-N10	2.559	2.553	2.581	2.548	2.577	2.542
La-N11	2.664	2.661	2.741	2.68	2.751	2.683
La-N12	2.536	2.545	2.580	2.541	2.575	2.541
La-N13	2.700	2.684	2.751	2.691	2.769	2.696
La-N14	2.548	2.546	2.582	2.546	2.576	2.539

Table 1: Geometry parameters of Ag-La complex optimized at different levels of DFT.

		def2-SVP		def2-TZVP		
Distance (Å)	Exp.	BP-D3(BJ)	BP	BP-D3(BJ)	BP	PBE0-D3(BJ)
Au-La	4.243	3.900	4.453	3.968	4.534	4.133
Au-P3	2.364	2.416	2.462	2.388	2.436	2.392
Au-P4	2.387	2.416	2.460	2.390	2.436	2.395
Au-P5	2.380	2.417	2.464	2.388	2.438	2.393
La-P6	3.481	3.230	3.502	3.237	3.507	3.307
La-P7	3.423	3.236	3.509	3.241	3.526	3.306
La-P8	3.377	3.229	3.498	3.234	3.519	3.305
La-N9	2.524	2.552	2.577	2.546	2.567	2.539
La-N10	2.542	2.552	2.576	2.547	2.571	2.542
La-N11	2.533	2.552	2.576	2.546	2.570	2.539
La-N12	2.658	2.683	2.734	2.685	2.746	2.688
La-N13	2.723	2.684	2.736	2.688	2.748	2.689
La-N14	2.624	2.682	2.729	2.682	2.748	2.679

Table 2: Geometry parameters of Au-La complex optimized at different levels of DFT.

3.4 Intramolecular Interaction

In this section, various contributions of intramolecular interactions were investigated in order to understand the short metal-metal distance between La and CM.

Initially, the metal-metal interactions were evaluated by the Wiberg bond order.[122] The Wiberg bond order between La and Au/Ag is negligible in all structures (less than 0.15, see Table 3). The result indicates that no covalent bonding exists between the two metal ions.

	def2-SVP		def2-TZVP		
	BP-D3(BJ)	BP	BP-D3(BJ)	BP	PBE0-D3(BJ)
Ag-La	0.07385	0.06236	<0.02	0.03437	<0.02
Au-La	0.12173	0.06451	<0.02	<0.02	<0.02

Table 3: Calculated Wiberg bond order of Au-La and Ag-La complexes at different levels.

Given the weak metal-metal interaction within the Ln-CM complexes, other potential interactions were explored through an Energy Decomposition Analysis (EDA).[123] EDA is a method that can only be applied to two sub-systems without direct chemical bonding, thus two model complexes (see Figure 6) were constructed and employed. In both models, the bridging phenyl-rings were removed, and the remaining P and N were saturated with H. In model A, the structure was further simplified and the non-bridging phenyl-rings were replaced by methyl groups. Therefore, the influence of the non-brdging phenyl-rings can be evaluated by comparing the interaction energy difference of the two models. Structures with three different metal-metal distances, specifically, the distances obtained by optimizing the complete complexes at BP/def2-TZVP with or without dispersion correction and the distances derived from the crustal structure, were used in the EDA analysis.

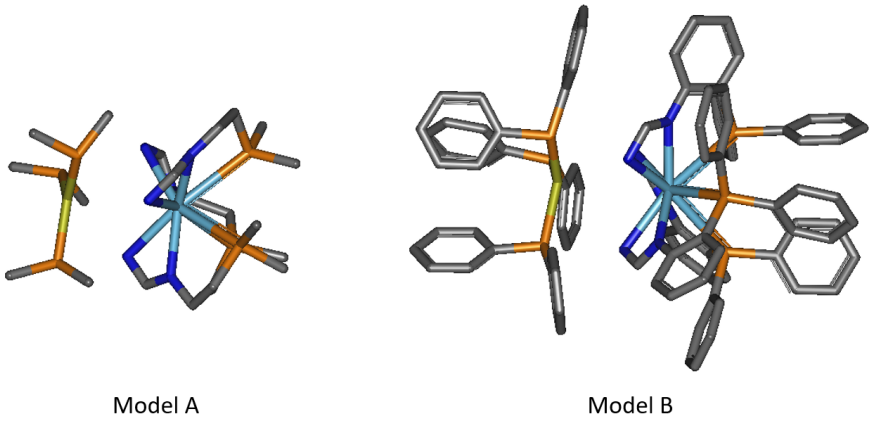

Figure 6: Illustration of the structure of model A (A) and model B (B) for the energy decomposition analysis. Hydrogen atoms are omitted for clarity. Grey: carbon, Orange: phosphorus, Yellow: gold/silver, Blue: nitrogen, Light blue: lanthanum.

Each individual contribution to the total interaction was given in the EDA results (Figure 7). Among all contributions, only the exchange repulsion was positive while the rest of the interactions including dispersion, correlation, orbital relaxation and electrostatic interaction were bonding interactions.

First, the interaction energies of complexes with the same metal-metal distance but different ligands (model A and B) were compared. For the Au-La complex, when the Au-La distance is 3.986 Å, the total interaction energy in model A is -1.939 eV, while for model B it is -1.962 eV. There is no significant difference of the total interaction energies in the two models (0.023 eV). Similar results can be found in the total interaction energy calculated at the other metal-metal distances. This result suggests that the non-bridging ligands have little significance in the total interaction.

Second, individual interactions in both models were compared at different metal-metal distances. The dispersion interaction in model B is -2.118 eV, which is 0.731 eV lower than in model A (-1.387 eV). However, the exchange repulsion in model B is 4.473 eV, which is 1.417 eV higher than the one in model A (3.056 eV). When the Au-La distance is 4.243 and 4.534 Å, the stabilizing effect caused by dispersion is cancelled out by repulsion, therefore, the total interaction energy is even higher in model B than in model A. Although the repulsive and attractive interactions change significantly with the change of the metal-metal distance, they compensate each other

in both model complexes, resulting in similar total interaction energies at different distances. A similar trend can be observed in the Ag-La complex.

In conclusion, the non-bridging phenyl-rings are not the main contribution to the intramolecular interaction to maintain the short distance between two ligand coordinations. The bridging phenyl-rings are important from a geometrical perspective, therefore, further investigation of the interaction between the bridging ligands and other ligands in the full complex was conducted.

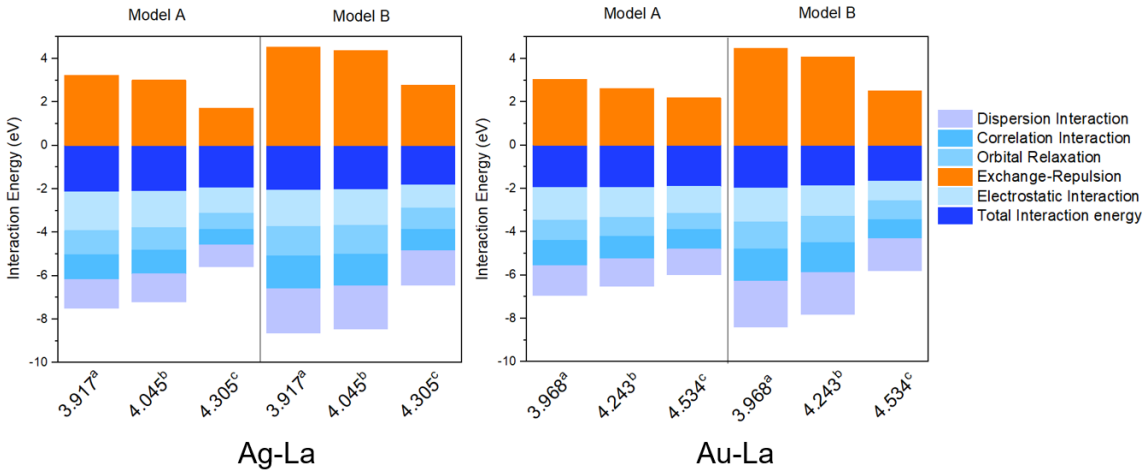

Figure 7: Energy decomposition analysis of model A and B of Ag-La and Au-La complexes, energies are in eV. [a]: The Ag/Au-La distance from the structure optimized in BP-D3(BJ)/def2-TZVP level; [b]: The Ag/Au-La distance from the crystal structure in experiments; [c]: The Ag/Au-La distance from the structure optimized in BP/def2-TZVP level.

Neither metal-metal interactions nor interactions between non-bridging phenyl-rings constitute the primary contribution to the intramolecular interaction. The dispersion interactions between the phenyl-ring subgroup and the rest of the molecule are studied, as well as the interactions between different subgroups. Three subgroups were considered (see Figure 8). These are the 1) phenyl groups acting as the bridges connecting the Au/Ag side ligand and La side ligand systems (marked in red); 2) the phenyl rings forming a plain on the M ligand side (marked in green); and 3) the phenyl groups between N and P atoms on the La ligand side (marked in velvet).

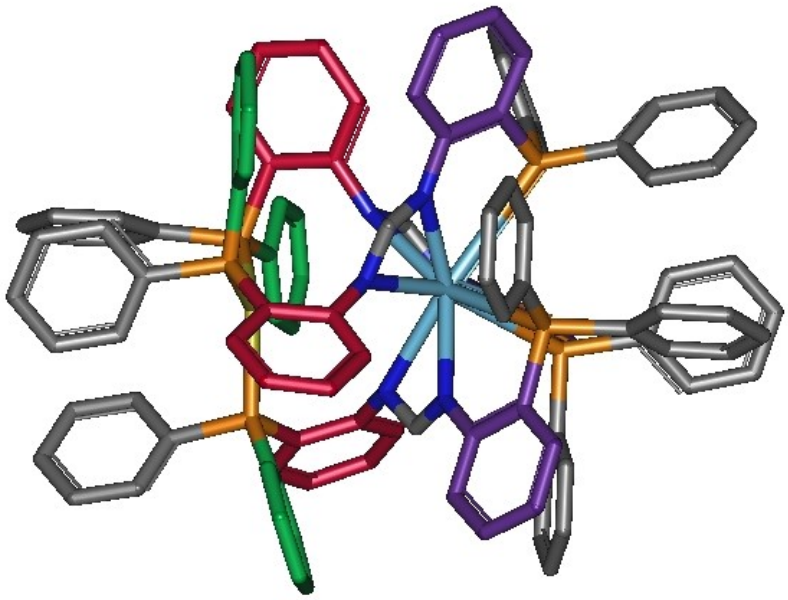

Figure 8: Illustration of phenyl rings subgroups (highlighted by green, purple and red) for analysis of dispersion interactions in the ligand system.

Empirical dispersion energies study shows that the dispersion interaction between the bridges (red) and the rest of the molecule is stronger than the interaction caused by other subgroups (see Table 4). The interaction between the bridges (red) and the plain (green) is more significant than between the other subgroups (Table 5). This result emphasizes the importance of ligand systems instead of metal-metal interactions in forming the investigated complexes.

	Au-La			Ag-La		
	Red	Green	Velvet	Red	Green	Velvet
E_1	-1.221	-1.297	-1.211	-1.229	-1.3	-1.215
E_2	-19.316	-19.825	-19.772	-19.035	-19.654	-19.595
E_{disp}	-4.191	-3.605	-3.745	-4.140	-3.449	-3.594
E_1'	-1.227	-1.301	-1.213	-1.228	-1.298	-1.214
E_2'	-17.334	-17.938	-17.996	-17.285	-17.916	-17.908
E_{disp}'	-3.705	-3.027	-3.057	-3.680	-2.978	-3.071

Table 4: Calculated dispersion interaction of various subgroups with the rest of the molecule in Au-La and Ag-La complexes (eV). E_{disp} =E_{total}-E_1-E_2, E_{total}= -24.728 and -24.404 eV in Au-La and Ag-La, is the dispersion energy of the complete molecule (based on the structure optimized in BP-D3(BJ) /def2-TZVP level). ': dispersion energy calculated based on the structure optimized without dispersion correction. E_{total}'= -22.266 and -22.192 eV in complex Au-La and Ag-La.

	Au-La			Ag-La		
	Red Green	Red Velvet	Green Velvet	Red Green	Red Velvet	Green Velvet
E_{a+b}	-2.518	-2.432	-2.508	-2.529	-2.444	-2.515
E_{a+b}	-3.648	-2.939	-3.028	-3.67	-2.877	-3.011
E_{ab}-E_{a+b}	-1.13	-0.507	-0.52	-1.141	-0.433	-0.496
E_{a+b}'	-2.528	-2.44	-2.514	-2.526	-2.442	-2.512
E_{a+b}'	-3.486	-2.758	-2.921	-3.524	-2.705	-2.849
(E_{ab}-E_{a+b})'	-0.958	-0.318	-0.407	-0.998	-0.263	-0.337

Table 5: Calculated dispersion interaction between various subgroups in Au-La and Ag-La (eV). The dispersion interaction between the two groups can be expressed by the energy difference of the dispersion energies of the two groups together (denoted as E_{ab}) and the sum of the energies (E_1 in Table 4) of the two separate groups (denoted as E_{a+b}).

3.5 Optical Properties

This section aims to interpret the experimental spectroscopic data which are shown in Figure 9 and Figure 10. The two figures are adapted from Figure 8 and Figure 9 from the reference.[103] Photoluminescence (PL) and photoluminescence excitation (PLE) spectra were recorded at various temperatures in the solid state by the group of Prof. P. Roesky. The spectra of Kdpfam, [dpfam$_3$La] and [dpfam$_3$Nd] are shown in Figure 9. The dpfam ligand exhibits signature emission band with a maximum at 437 nm.[103] For the [dpfam$_3$Nd], three emission bands are around 900 nm, 1100 nm and 1400 nm. This is expected because the f-f transition of Nd^{3+} is in the near infrared (IR) range.[124] However, the absence of f-electrons in La^{3+} results in no emission bands in this range for [dpfam$_3$La]. Interestingly, in the hetero-bimetallic Au-La and Ag-La complexes, broad emission bands emerge in the near IR range even in the absence of Nd^{3+}. Excited states calculations were conducted for the Au-La, Ag-La complexes and a model complex containing Nd.

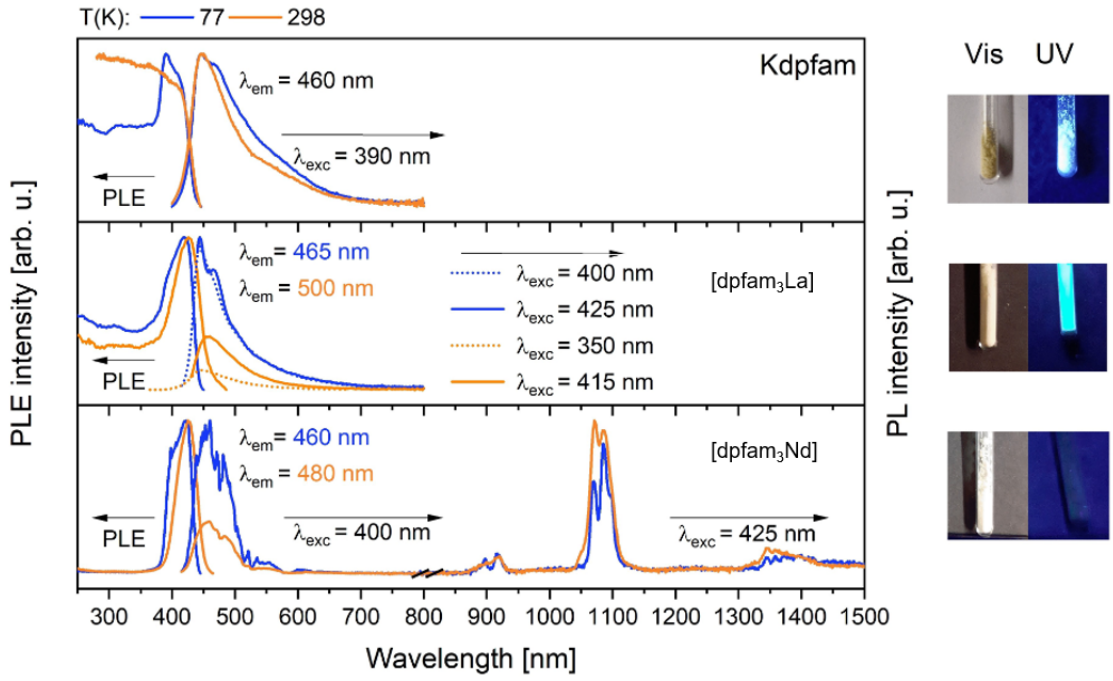

Figure 9: PL and PLE spectra of Kdpfam, [dpfam$_3$La] and [dpfam$_3$Nd] recorded at 77 K and room temperature at the given emission (PLE spectra λ_{em}) and excitation wavelengths (PL spectra λ_{exc}). This figure is adapted from the reference[103] Figure 8. Structures of [dpfam$_3$La] and dpfam$_3$Nd] can be found in the reference.[103]

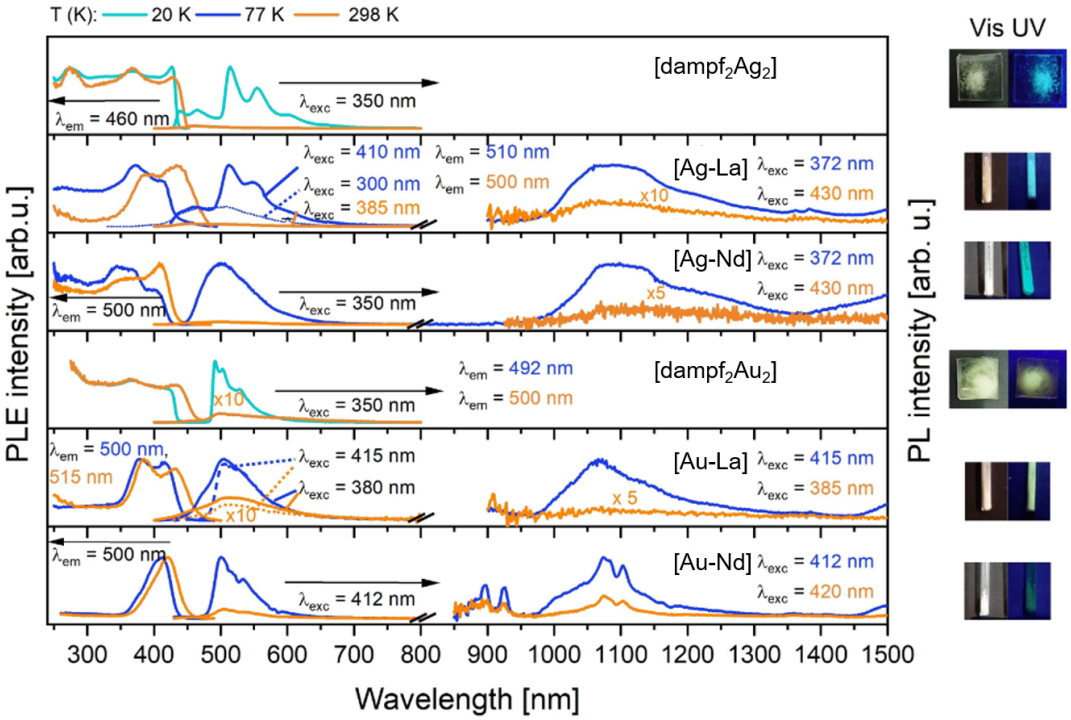

Figure 10: PL and PLE spectra of [dpfam$_2$Ag$_2$] and [dpfam$_2$Au$_2$] (from the reference[125]) to compare with the spectra of [Ag-La], [Ag-Nd], [Au-La] and [Au-Nd] complexes recorded at 77 K and room temperature at the given emission (PLE spectra λ_{em}) and excitation wavelengths ((PL spectra λ_{exc}). This figure is adapted from reference[103] Figure 9. Structures of Ag-La and Au-La complexes whose structures are illustrated in Figure 5. Ag-Nd and Au-Nd share similar structures as Ag-La and Au-La complexes but with Nd instead of La. Molecular structures of [Ag$_2$] and [Au$_2$] can be found in the reference.[125]

To investigate the splitting of the electronic states by the ligand field, spin orbit configuration interaction calculations were performed for a model system resembling the ligand field in the ground state structure of complex Au-Nd. Nd^{3+} has a electron configuration of [Xe]$4f^3$. The ground state is $^4I_{9/2,\ 11/2,\ 14/2,\ 15/2}$ with $^4I_{9/2}$ lowest in energy.

Starting from the simplified model in Figure 11 (Right), Mulliken charges were obtained in a DFT calculation (BP/def2-TZVP) and re-scaled in such a way that Nd has a charge of 3+. Afterwards, the electronic states of Nd^{3+} were calculated in the point charge field describing the ligands. For comparison, the energy levels of the free ion were calculated. Dynamical correlation is not included in the CASOCI calculations, thus the error for the energy of the excited $^4F_{3/2}$ state amounts to 4498 cm^{-1} compared to the NIST data base.[126] Therefore, the states corresponding to the $^4F_{3/2}$ were shifted by this value before calculating the f-f transitions $^4I_{9/2}\leftarrow{}^4F_{3/2}$, $^4I_{11/2}\leftarrow{}^4F_{3/2}$ and $^4I_{13/2}\leftarrow{}^4F_{3/2}$.

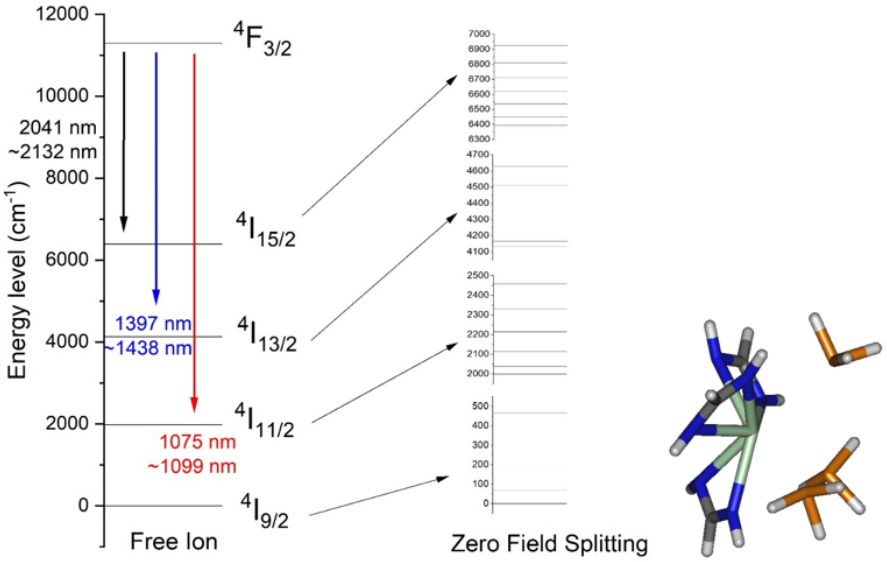

Figure 11: Left: Energy levels of Nd(III). Left: free ion, the first value for the wavelength refers to the free ion, the second one to the average of all levels in the point charge field. In both values a shift of the $^4I_{3/2}$ state is considered (see text). Middle: electronic states with zero field splitting in the point charge field. Right: Model complex for the calculation of the electronic states of the Nd complex.

To obtain an overview about possible emissions of the Au-La complex we used the model complex Au-La-sim (Figure 12, left). For this complex, TDDFT calculations

were performed at PBE0/def2-TZVP level. The lowest excited state was a ligand to metal-metal charge transfer state from one of the N combined with the bridging phenyl into a bonding orbital between the two metals (Figure 12, right). This indicated a dependence of the excitation from the distance of the metal centers. In Figure 13, calculated spectra for different metal-metal distances are shown. The excitation energy drops significantly with decreasing distance, while the character of the transition remains the same. The lowest energy was found for a Au-La distance of 3.3 Å.

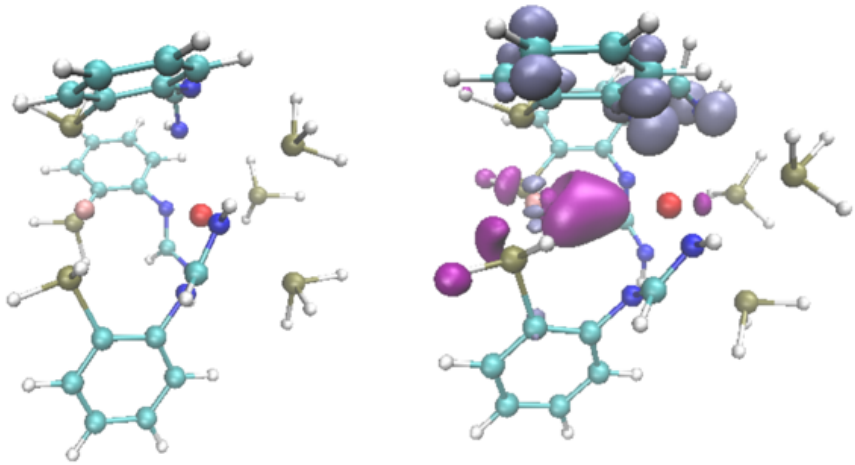

Figure 12: Illustration of model complex Au-La-sim for excited state optimizations in TDDFT. (Pink: Au; Red: La; Cyan: C; Tan: P; Blue: N; H: White). Right: Transition density of the lowest excited state obtained by TDDFT at the excited state structure (PBE0-D3(BJ)/def2-TZVP).

Based on these results obtained from the simplified model, a triplet state of the full complex was optimized starting from a shortened metal-metal distance and sTDA[118] calculations were performed based on the triplet optimized structures and compared with those performed based on ground state structures.

The metal-metal distance in the optimized triplet Au-La structure is significantly shortened compared to the ground state structure, featuring a change from 4.266 to 3.372 Å (see Table 6), while the metal-metal distance is only decreased by 0.1 Å in the Ag-La complex.

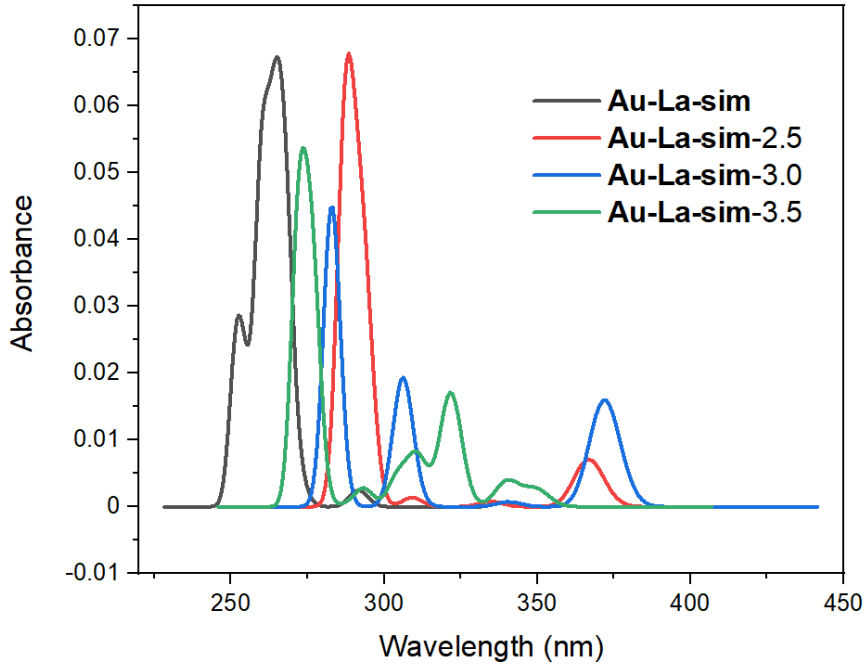

Figure 13: TDDFT spectra for Au-La-sim with variation of the Au-La distance (2.5, 3.0 and 3.5 Å). For each distance, the ground state structure was optimized. The lowest excitation energy was found for a distance of 3.0 Å.

	Au-La complex		Ag-La complex	
	singlet	triplet	singlet	triplet
Distance (Å)	4.266	3.372	3.990	3.817

Table 6: Optimized metal-metal distances (Å) of Au-La and Ag-La complexes in the singlet and triplet states at PBE0-D3(BJ)/def2-TZVP level.

At the optimized triplet structure of the Au-La complex, the lowest excitation was a HOMO-LUMO excitation which amounted to 2.65 eV (468 nm) for the singlet and 2.57 eV (482 nm) for the triplet excitation, respectively. The origin of the lowest excitation was a transfer from the amidinate ligand to the region between the metals shown in Figure 14,[103] featuring a ligand to metal-metal charge transfer (LMMCT). Table 7 lists the first 5 low-lying excitation energies and the main transition for the triplet structure of the Au-La complex. In the 5 states, the dominant transition is always in the direction to the LUMO. The corresponding orbitals are plotted in Figure 15.

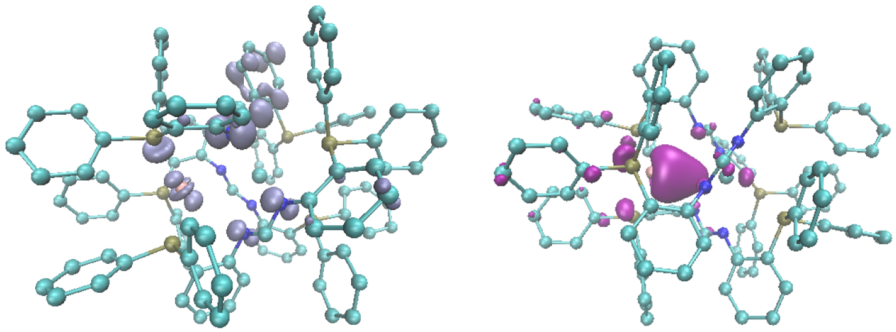

(A) **(B)**

Figure 14: Transition of the lowest excited state obtained by sTDA at the triplet structure of Au-La complex. (A): HOMO; (B): LUMO. Isovalue=± 0.05 a.u.. In the excitation, electron density is shifted from the region of the ligand shown in A to the region between the metal centres (LMMCT).

State	Excitation energy (eV)	Excitation energy (nm)	Main Transition	Contribution of the main transition
1	2.649/2.57	468.0/482.4	HOMO > LUMO	0.98/0.92
2	2.812/2.811	440.9/441.1	HOMO-1 (Fig. 15-A) > LUMO	0.98/0.96
3	2.967/2.97	417.9/417.5	HOMO-2 (Fig. 15-B) > LUMO	0.98/0.90
4	3.062/2.989	404.9/414.8	HOMO-3 (Fig. 15-C) > LUMO	0.96/0.85
5	3.281/3.276	377.9/378.4	HOMO-4 (Fig. 15-D) > LUMO	0.96/0.92

Table 7: First 5 low-lying singlet/triplet excitation energies and the main character of the transition for Au-La complex at its optimized triplet structure.

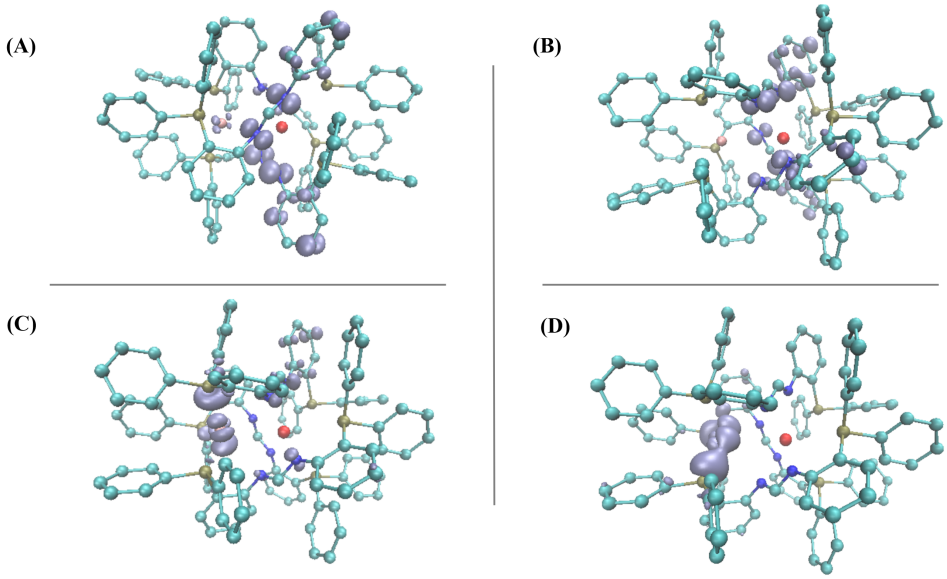

Figure 15: Selected molecular orbitals (A to D is HOMO-1 to HOMO-4) of the lowest triplet state of the Au-La complex. Isovalue=± 0.05 a.u..

The form of the spin density of the triplet state (see Figure 16) further supports the metal-metal cooperativity in the excited state, which can be classified as ligand to metal-metal charge transfer (LMMCT).

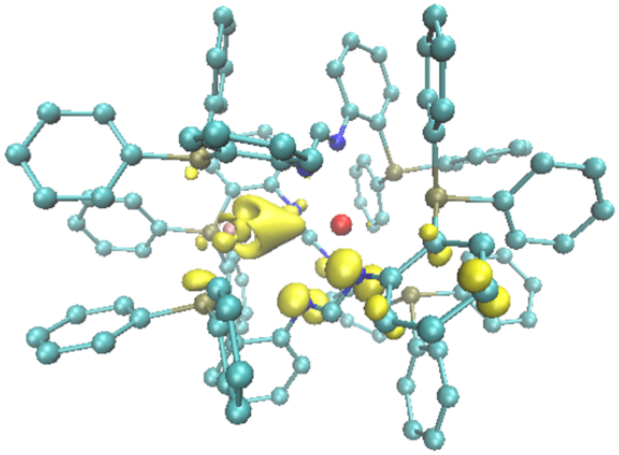

Figure 16: Spin density of the triplet state of Au-La complex at the triplet structure. Isovalue=± -0.005 a.u..

Nonetheless, in the ground state structure of Au-La complex, the HOMO-LUMO excitation features a ligand-to-ligand charge transfer (LLCT) see Figure 17, A to B

is HOMO to LUMO. The lowest 6 unoccupied orbitals show no contributions to the possible metal-metal interaction (see Figure 18).

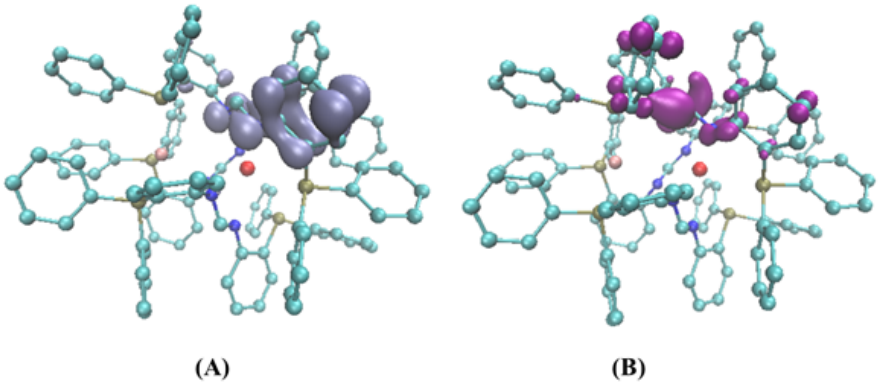

Figure 17: Transition of the lowest excited state obtained by sTDA at the singlet state structure of Au-La complex. (A): HOMO; (B): LUMO. Isovalue=± 0.05 a.u..

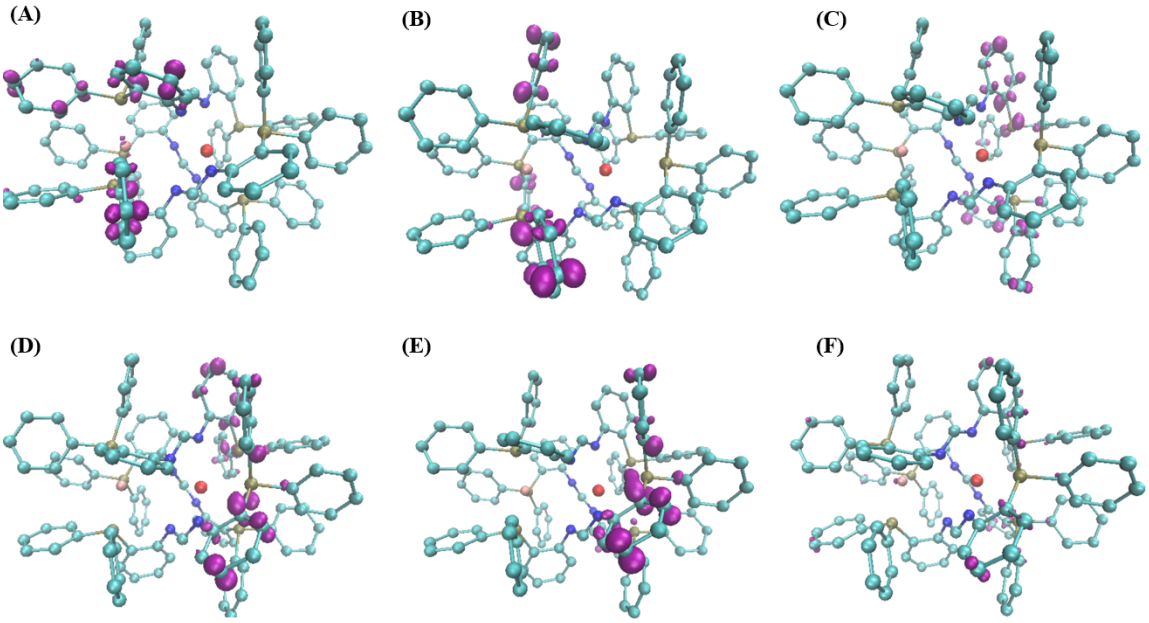

Figure 18: Selected molecular orbitals (A to F is LUMO+1 to LUMO+6) for the ground state structure of the Au-La complex. Isovalue=± 0.05 a.u..

For the Ag-La complex, the metal-metal distance only changed by only 0.1 Å (Table 6) with a singlet-triplet gap of 2.57 eV. In the sTDA for the triplet structure, the first

singlet and triplet excitation energies amount to 3.21 eV (386.7 nm) and 2.85 eV (435 nm), respectively. The HOMO-LUMO excitation showed no LMMCT feature, but rather demonstrated a LLCT (see Figure 19). The HOMO-LUMO transition in the singlet structure of Ag-La complex also features LLCT (see Figure 20).

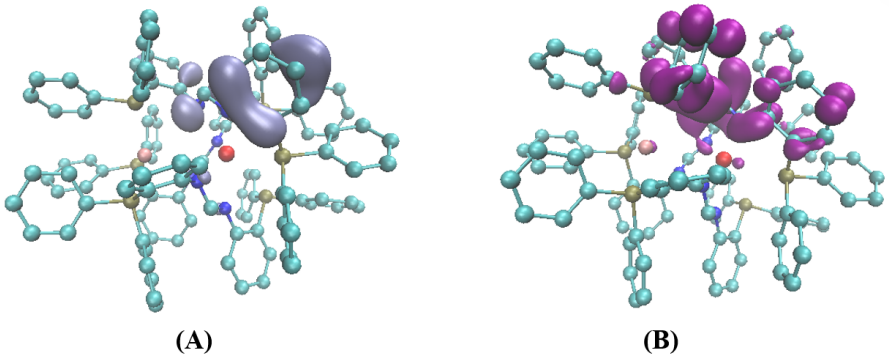

Figure 19: Transition of the lowest excited state obtained by sTDA at the triplet state structure of Ag-La complex. (A): HOMO; (B): LUMO. Isovalue=± 0.05 a.u..

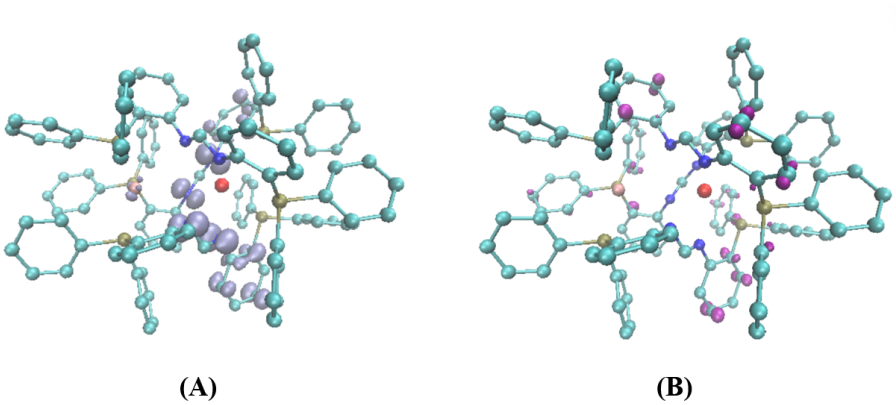

Figure 20: Transition of the lowest excited state obtained by sTDA at the singlet state structure of Ag-La complex. (A): HOMO; (B): LUMO. Isovalue=± 0.05 a.u..

3.6 Conclusions

In this chapter, structural and optical properties of Au-La and Ag-La complexes were investigated.

The detailed analysis of intramolecular interactions in the ground state structure has elucidated that the primary contribution to the short metal-metal distance is the dispersion interaction between the bridging ligands and other parts of the molecule in both complexes. No significant metal-metal interaction was found in the ground state of either Au and Ag complexes.

Excited states calculations were carried out for Au-La and Ag-La complexes. A ligand to metal-metal charge transfer (LMMCT) was found at the triplet structure of the Au-La complex, indicating a possible metal-metal interaction in the excited state of Au-La complex. The shortened metal-metal distance and spin density distribution in between the metal area in the triplet structure also support the result obtained from excited state calculations. However, no LMMCT was found at the ground state structures of either complexes, nor in the triplet state structure of Ag-La complex. The cooperative effect between lanthanide and coinage metals is only observed in the triplet structure of the Au-La complex.

Optical properties of Au-La, Ag-La and Au-Nd complexes were investigated by CASOCI, TDDFT and sTDA. From the CASOCI calculated excitation energy of the Nd model complex, the emission in the near IR regime can be interpreted as a 4f-4f transition $^4I_{11/2} \leftarrow {}^4F_{3/2}$. For Au-La and Ag-La complexes, the triplet excitation was found at 482 nm and 435 nm, respectively. However, no excitation was found at the range of 1100 nm. A possible explanation is that the excited state structure present in the emission spectra was not obtained.

4 Magnetic Properties of Complexes Containing TM or Ln Elements

4.1 Introduction

The Mn_{12} complex $[Mn_{12}O_{12}(O_2CR)_{16}(H_2O)_4]$[13] is the first single molecule magnet (SMM) identified by Sessoli *et al.*,[11,12] which shows slow magnetization relaxation below 4 K.[12] The discovery of polynuclear transition metal complexes exhibiting magnetic hysteresis has catalyzed the research into the first generation of SMMs. These SMMs utilize exchange coupling between transition metal centers to construct molecules with a large total spin, consequently, yielding a substantial magnetic moment.[5]

However, achieving SMM characteristics that can be potentially applied to information storage and quantum computing[127] requires considering not only of a large magnetic moment but also of two other criteria, a bistable ground state and a large magnetic anisotropy.[5] The requirement for a bistable ground state stems from the need for two degenerate states in binary memory storage.[5] The large anisotropy is required due to its connection to the magnetic reversal energy barrier U_{eff} by eq. 78.[128] U_{eff} represents the energy required to transition between these bistable ground states. It is clear that a large anisotropy is s required to achieve a higher U_{eff}.

$$\tau^{-1} = \tau_0^{-1} e^{-(U_{\text{eff}}/k_B T)} \tag{78}$$

Despite of the large magnetic moment in the ground state, polynuclear transition metal complexes still have small U_{eff} due to their small magnetic anisotropy.[5] This phenomenon is shown in a Mn_{19} complex ($[Mn^{III}{}_8Mn^{IV}{}_4O_{12}(O_2CR)_{16}(H_2O)_4]$(R= Ph, Me)) discovered by Ako *et al.*, which possesses a large ground state spin S=83/2 but a small U_{eff}=5.8 K.[129]

Inspired by the lanthanide double decker complexes from Ishikawa *et al.*[130], a second generation of SMMs were discovered and gained popularity since 2003.[131] The second generation SMMs feature complexes[132,133] with one or more lanthanide ions as magnetic centers. The advantage of lanthanide based SMMs can be attributed to the substantial magnetic moment and anisotropy inherent to them.[5] Ideally with high U_{eff}, a slow magnetic relaxation should be obtained up to room temperature, making SMMs suitable for practical applications. However, various relaxation mechanisms, particularly the temperature-independent Quantum Tunneling of Magnetization (QTM)[134,135] impede SMMs from achieving an open magnetic hysteresis at such temperatures.[5]

One possible method to improve SMM performance is to shift the QTM relaxation away from zero-field[136] by utilizing magnetic coupling between lanthanide ions or with radicals.[5] In 2022, Gould *et al.*[14] reported a dinuclear dysprosium SMM tha features strong Ln-Ln interaction via radical bridge, achieving the highest to date U_{eff} (2347 K) which also shows open hysteresis up to 72 K.

Quantum chemical studies are valuable for interpreting magnetic properties, elucidating magnetic relaxation mechanisms, and ultimately providing insights for the rational design of high-temperature SMMs. CASSCF calculations and the inclusion of SOC have become a standard approach in the field of molecular magnetism.[5] In this chapter, quantum chemical calculations were carried out to investigate the magnetic properties of lanthanide (sections 4.3 and 4.4) and transition metal (section 4.5) complexes.

4.2 Computational details

Geometry optimizations were carried out with the computational chemistry package Turbomole.[107] In all complexes, only the hydrogen positions were optimized, addressing the common issue of underestimated hydrogen-atom distances that often occurs during the crystallographic refinement of single crystal X-ray structures.[137] Restricted Open-shell Hartree Fock (ROHF) was employed to obtain open-shell molecular orbitals with Turbomole.[25,107] CASSCF calculations were carried out using the Bochum CASSCF program.[30]

Energy levels and magnetic properties were calculated and extracted using the Complete Active Space Spin-Orbit Configuration Interaction (CASOCI) program.[16] The Broken symmetry Density Functional Theory (BS-DFT)[83] approach was employed to determine the exchange coupling constants using Turbomole[107]. The exchange coupling constants were calculated with eq.73 proposed by Yamaguchi.[84,85]

In this section, chemical structures are visualized with VMD[119] and graphs are plotted with Origin.[121]

4.2.1 Lanthanide Complexes

For momoners, the hydrogen positions were optimized at TPSS[138]-D3(BJ)[110,111]/def2-TZVP[115] level with diamagnetic substitution[1] by Y^{3+}. The RI Approximation[112,113] was applied with corresponding auxiliary basis sets.[114]

For Dy^{3+}, the Roothaan parameters[25] are a=238/243 and b=308/243 while a=119/121 and b=126/121 for Er^{3+} (see Table A1). For ROHF calculations, an x2c-TZVPall[139] basis set was employed to all atoms. Fourth-order Douglas-Krolloll-Hess[140,141] transformation was used for the optimization of ROHF orbitals to incorporate relativistic effect. For CASSCF calculations, the def2-SVP[115] basis set was employed to all H atoms, while the x2c-TZVPall[139] basis set[139] was used for the rest of atoms.

In all dimers, DFT-BS calculations were performed with Gd^{3+} replacing Dy^{3+}/Er^{3+}. DFT calculations were carried out for the high spin and broken symmetry states at B3LYP[108,142,143] level. The x2c-TZVPall[139] basis set was employed to describe the metal atoms and the atoms in the first coordination sphere, while x2c-SV(P)all[139] was used for the rest of the atoms. Fourth-order Douglas-Kroll[140,141] transformation was applied for both the high spin and broken symmetry states. ROHF and CASSCF calculations for dimers were carried out including only one open-shell ion with the other ion substituted by Y^{3+}. For ROHF/CASSCF calculations, the basis set x2c-TZVPall[139] was employed for the metal ion and atoms in the first coordination sphere while x2c-SVPall[139]/def2-SV(P)[115] basis sets were used in other atoms.

[1] The open-shell ions substituted by closed-shell diamagnetic ions, normally the ion with the same charge and similar ionic radius is chosen.

4.2.2 Transition Metal Complexes

With the single crystal X-ray structure obtained from experiments, hydrogen atoms were optimized at TPSS[138]-D3(BJ)[110,111]/def2-TZVP[115] level. Fe^{2+} was replaced by Zn^{2+} during geometry optimization.

ROHF calculations were carried out at B3LYP[108,142,143]-D3(BJ)[110,111]/def2-TZVP[115] level. The Roothaan parameters were calculated by the Mathematica script.[25] For each Fe^{2+} the Roothaan parameters are a=35/36 and b=25/18. When two Fe^{2+} were considered, the Roothaan parameters for the two interacting open-shells are a=1 and b=13/9.

4.3 Diborataanthracene Lanthanide Complexes

In this section, four diborataanthracene (DBA) lanthanide complexes were investigated which were synthesized by Uhlmann from Prof. Roesky's group at Karlsruhe Institute of Technology. Structures of these four complexes, which are two monomers (2-Er and 2-Dy) and two dimers (3-Er and 3-Dy) are given in Figure 21. The Ln^{3+} ions are located in between two ligand planes, which are COT^{TIPS} (1,4-($^{i}Pr_3Si)_3C_8H_6$, TIPS = triisopropylsilyl) and diborataanthracene (DBA) ligands. For the dimers, the DBA ligand is in the middle while COT^{TIPS} ligands on both ends. The monomers/dimers feature double/triple-decker sandwich-type complexes.

The charges of both COT^{TIPS} and DBA ligands are -2. For the monomers, one counterion K^+ with charge of +1 is present in the unit cell. The monomer structure within one unit cell is charge neutral. However, the Ln-K distances are similar for counterions in the next and the same unit cell (4.4 and 4.9 Å for 2-Er, 4.4 and 5.0 for 2-Dy). To account for the effect of counterions, three model complexes were investigated first (see Figure 22). The dimers possess C_i symmetry, which results in the same coordination environment for the two metal centers. The metal-metal distances are 4.5 and 4.6 Å in 3-Er and 3-Dy, respectively.

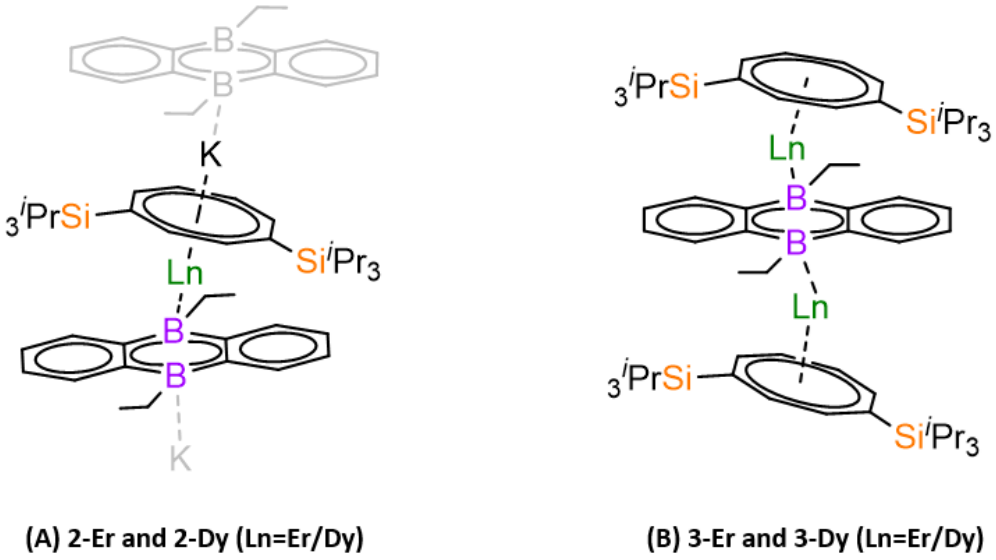

Figure 21: Structures of the four diborataanthracene rare-earth complexes investigated in this section.

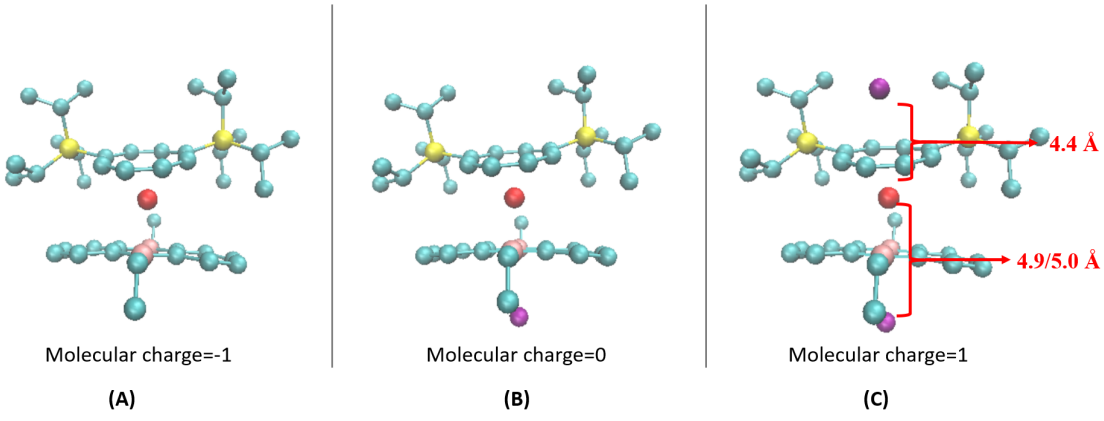

Figure 22: Illustration of three models for 2-Er/Dy are shown. The models are model A without counterion, model B with one counterion and model C with two counterions. (C: cyan; Si: yellow; K: purple; B: pink; Er/Dy: red; hydrogen atoms are omitted for clarity).

4.3.1 Energy Levels

For lanthanide ions, Russel-Saunders coupling is the dominant contribution to energy splitting followed by ligand field splitting. A free Er^{3+} ion has a $4f^{11}$ occupation with angular momentum L=6 and a total spin S=3/2. Thus, the Russel-Saunders (RS) Term is $^4I_{15/2,\ 13/2,\ 11/2 \text{ and } 9/2}$ with $J = 15/2$ as the ground state. For Dy^{3+} the Russel-Saunders term is $^6H_{15/2,\ 13/2,\ 11/2,\ 9/2,\ 7/2,\ 5/2}$ with $J = 15/2$ as the ground state.

In Figure 23, the splitting of all states corresponding to the different J-states of the Russel Saunders ground term are shown for the free ion as well as for the three models A, B, and C for 2-Er and 2-Dy, respectively. The calculated energy levels of each electronic state are within the same range compared to the experimental values of the free ions from the NIST Database.[126] This observation is anticipated, as the ligand-field splitting exerts only a minor influence on the electronic energy of Ln^{3+} coordination compounds. A detailed plot of the splitting of the $^4I_{15/2}$ state of 2-Er can be found in Figure 24. For the model without any counterion (A) and with two counterions (C), the first excited Kramers Doublet (KD) is around 50 cm^{-1} higher in energy than the ground KD. However, for the model molecule with one counterion (B) the energy gap is around 100 cm^{-1}. Comparing all other corresponding excited KDs between the three models, one can see that model B differs from A and C. The same trend can be observed in the 2-Dy complex.

The presence of only one counterion can bring up to around 50 cm^{-1} energy difference for the same KDs. The difference can be caused by the reduced ligand symmetry in the model B. In the following, we discuss the results obtained with two counterions (Figure 22, C) since it is closest to the situation in the crystal structure.

After confirming the use of the two-counterion model for the monomers, different methodologies were examined for the low-lying energies. The energy levels calculated from ROHF and CASSCF optimized orbitals of $^4I_{15/2}$ and $^6H_{15/2}$ states (lowest eight KDs) of 2-Er and 2-Dy are compared in Table 8.

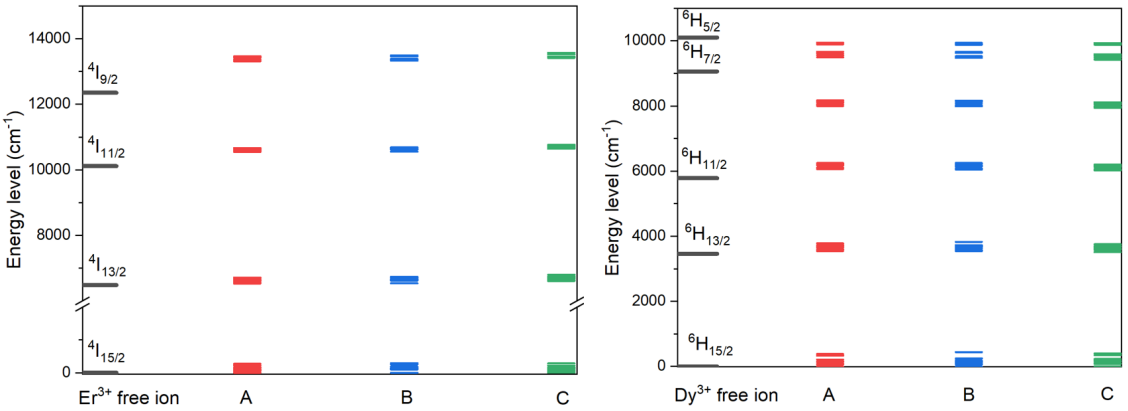

Figure 23: Calculated energy levels (cm^{-1}) of 2-Er (left) and 2-Dy (right) without counterion K^+ (A), with one K^+(B) and with two K^+ (C) compared with the atomic energy spectra of the free ion.[126]).

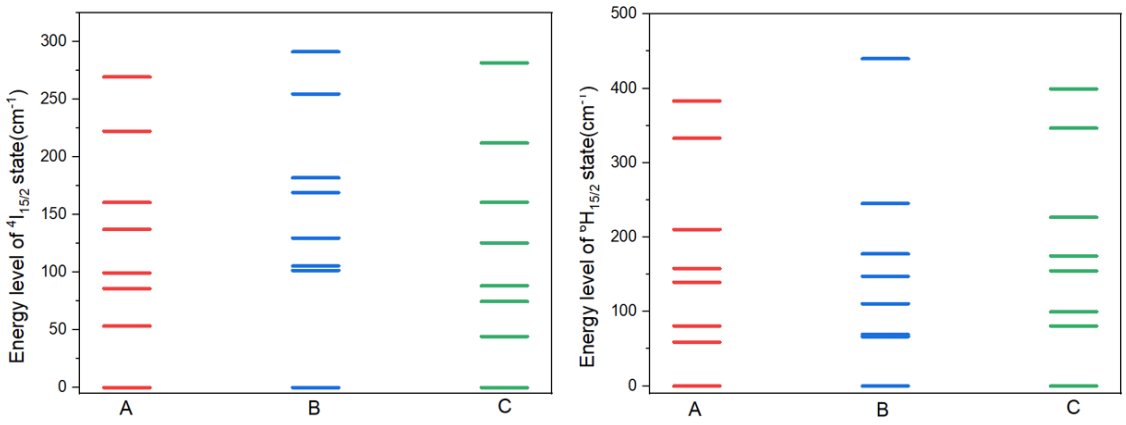

Figure 24: Calculated energy levels of the first 8 KDs (cm^{-1}) in the 2-Er (left) and 2-Dy (right) without counterion K^+ (A), with one K^+(B) and with two K^+ (C).

The energies derived from the ROHF orbitals exhibit good agreement with those obtained from CASSCF orbitals when considering all high spin states (35 quartet states for 2-Er and 21 sextet states for 2-Dy). It is anticipated that the energies calculated using ROHF orbitals will align well with those based on CASSCF orbitals that are optimized for all high-spin states. For the chosen Roothaan parameters, the ROHF orbitals are optimized for an average over all high-spin determinants.[25] However, a notable energy difference was observed when comparing the energies obtained from ROHF orbitals or from CASSCF orbitals optimized for the lowest RS state in the 2-Er.

With significantly less computational effort, ROHF calculations offer a reasonable

description of low-lying states and good starting orbitals for CASSCF. Consequently, ROHF calculations were carried out for all complexes and the magnetic properties were examined with orbitals optimized at ROHF and CASSCF level (orbitals of the lowest RS states).

	2-Er			2-Dy		
	ROHF	CASSCF*	CASSCF**	ROHF	CASSCF$^{!}$	CASSCF$^{!!}$
1st KD	0.00	0.00	0.00	0.00	0.00	0.00
2nd KD	44.45	145.24	44.15	80.56	89.76	80.15
3rd KD	74.68	148.02	74.37	99.78	114.33	98.73
4th KD	88.33	183.40	88.11	154.72	168.38	154.27
5th KD	125.46	224.61	125.13	174.75	193.72	173.93
6th KD	160.81	240.81	160.51	226.54	246.73	225.41
7th KD	212.17	352.03	211.84	346.48	373.91	345.00
8th KD	281.64	374.43	281.32	399.28	425.79	399.68

Table 8: Energy levels of the lowest eight KDs in 2-Er and 2-Dy calculated from ROHF and CASSCF(n,7) (n=11 and 9 for 2-Er and 3-Dy, respectively) optimized orbitals. *: orbitals of 13 quartet states were optimized. **: orbitals of 35 quartet states were optimized. $^{!}$: orbitals of 11 sextet states were optimized. $^{!!}$: orbitals of 21 sextet states were optimized.

Figure 25 shows the calculated energy level of the first eight KDs of all four complexes. Firstly, the energies calculated on each metal center individually within the dimers are identical (Figure 25, left). This further proves the ligand surroundings of each metal center are identical in the dimers due to the C_i molecular symmetry. Therefore, calculations were done on one metal center in the dimers in the future. Secondly, the energies of 2nd KDs from different methods were compared. Special focus was put on this energy because it is crucial for possible magnetic relaxation pathways. The energies of the 2nd KDs always increase for orbitals obtained for the lowest RS term. The increase is significant for 2-Er, with a change from 44.45 cm^{-1} to 145.24 cm^{-1}. Lastly, the calculated excitation energy for the 2nd KD of various complexes were compared. The excitation energy to the 2nd KD calculated with CASSCF-optimized orbitals is the highest in the 3-Er (147.99 cm^{-1}) whereas it is the lowest in 3-Dy (75.81 cm^{-1}). For the energies obtained from ROHF-optimized orbitals, the highest 2nd KD energy is still in 3-Er (97.9 cm^{-1}) while the lowest is in 2-Er (44.45 cm^{-1}).

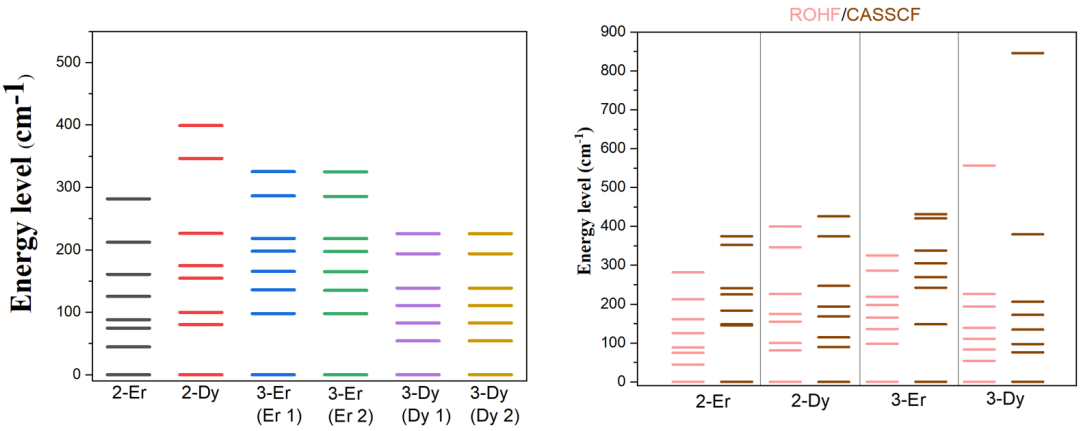

Figure 25: Left: Calculated energy levels (cm^{-1}) of the first eight KDs in 2-Er, 2-Dy, 3-Er and 3-Dy with ROHF-optimized orbitals (for 3-Er and 3-Dy, the calculations are done on one of the spin centers with the other center substituted by diamagnetic Y^{3+}). Right: Calculated energy levels (cm^{-1}) of the first eight KDs in 2-Er, 2-Dy, 3-Er and 3-Dy with ROHF-optimized (pink) and CASSCF-optimized (brown) orbitals.

4.3.2 Magnetic Properties

The calculated and measured temperature dependent molar magnetic susceptibility $\chi_M T$ verses temperature (T) of the four complexes are plotted in Figure 26. ROHF/CASSCF-optimized orbitals give similar results for molar magnetic susceptibility. In all complexes, the room temperature $\chi_M T$ agrees with the measured magnetic data. However, in the low temperature range, the calculated $\chi_M T$ is larger than measured.

g-factors of the eight KDs in the ground RS term are calculated. Table 9 and 10 show g-factors calculated from CASSCF-optimized orbitals. Table A2 and A3 show g-factors calculated with ROHF-optimized orbitals. The deviation between g-factors calculated with ROHF/CASSCF-orbitals is small but not negligible. Particularly for the 2^{nd} KD, the magnetic main axes show different orientations (see Figure A1). The magnetic properties calculated with CASSCF-optimized orbitals are discussed in the current and next section.

The ground state magnetic main axes (Table A4) of the four complexes are plotted in Figure 27. The magnetic main axis of 2-Er ground state is almost perpendicular (83 °) to the DBA ligand plane. However, for 2-Dy the main axis is more parallel to the

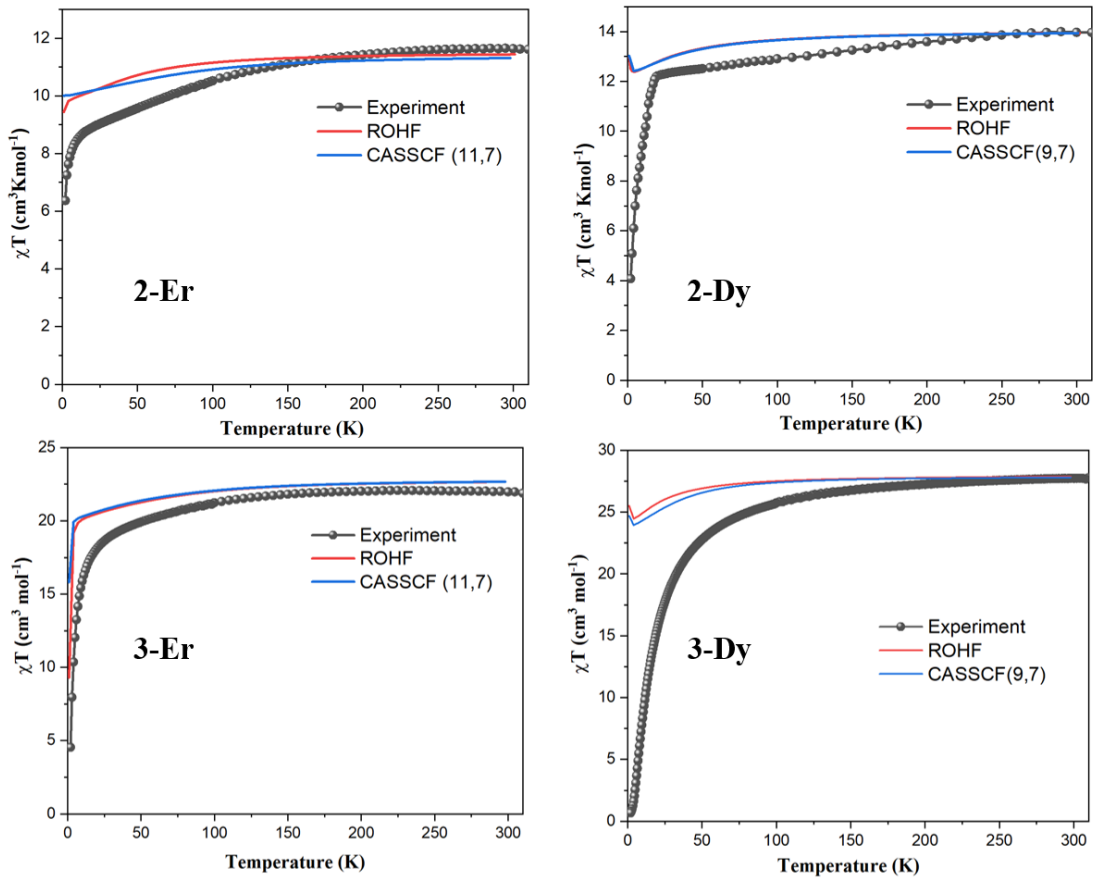

Figure 26: Measured and calculated magnetic susceptibility $\chi_M T$-T of 2-Er, 2-Dy, 3-Er and 3-Dy. Black dots: measured magnetic susceptibility; Red curve: CASOCI calculated magnetic susceptibility with ROHF-optimized orbitals; Blue curve: CASOCI calculated magnetic susceptibility with CASSCF-optimized (low-lying high-spin states) orbitals.

it (with an angel of 54 °). For the dimers, the direction of the magnetic main axes remains almost unchanged in 3-Er (84 °) while is even more parallel to DBA ligand in 3-Dy (29 °) compared to their monomer analogues.

The ground KDs of both 2-Er and 2-Dy possess large anisotropy with large g_z values and almost zero g_x=g_y=0, for 2-Er the g_z=17.81 while for 2-Dy g_z=19.79. The m_j composition shows the main components of the ground KDs in both complexes, which are m_j=±15/2 state with 97.8% and 98.8% (see Table A6 and A7), respectively. Due to the large anisotropy and high percentage of m_j=15/2 states in the ground state, both 2-Er and 2-Dy exhibit SMM behavior.

Large anisotropy is also obtained for the dimers with g_x=g_y=0, g_z=17.88 for 3-Er and g_x=0.01, g_y=0.03, g_z=19.41 for 3-Dy. A high percentage of m_j=±15/2 component in the ground doublets is also retained with 99 % for 3-Er (Table A8). However, it is reduced to 92 % for 3-Dy compared to its mononuclear counterpart (Table A9).

The orientations of the magnetic main axes obtained align with those reported for Er and Dy sandwich complexes featuring COT" ligands (COT": 1,4-bis(trimethylsilyl)-cyclooctatetraenyl dianion).[144,145] In the sandwich-shape $[Dy(COT")_2]^{-1}$ complex, the orientation of the magnetic main axis is sensitive to the second coordination sphere.[145]

Rinehart and Long[146] characterized f-elements into prolate/oblate-shape by their f-orbital electron densities.[146] They predicted a prolate-shape Er^{3+} should benefit in an equatorial ligand surrounding whereas an axial ligand surrounding is preferred for an oblate-shape Dy^{3+} to maximize the anisotropy of f-ions.[146] A large ground state magnetic moment is also found in $[Dy(COT")_2]^{-1}$ type complexes.[145] This can be explained by the reduced symmetry surrounding of Dy^{3+}.[145] It is known that Dy^{3+} that the ground state anisotropy benefits from a low symmetry surrounding.[145,147] For 2-Dy and 3-Dy, the symmetry is reduced (compared to bare $Dy(COT)^2$ complex) due to the different ligand planes and the angle between them. Therefore, a large anisotropy was still obtained in the ground state.

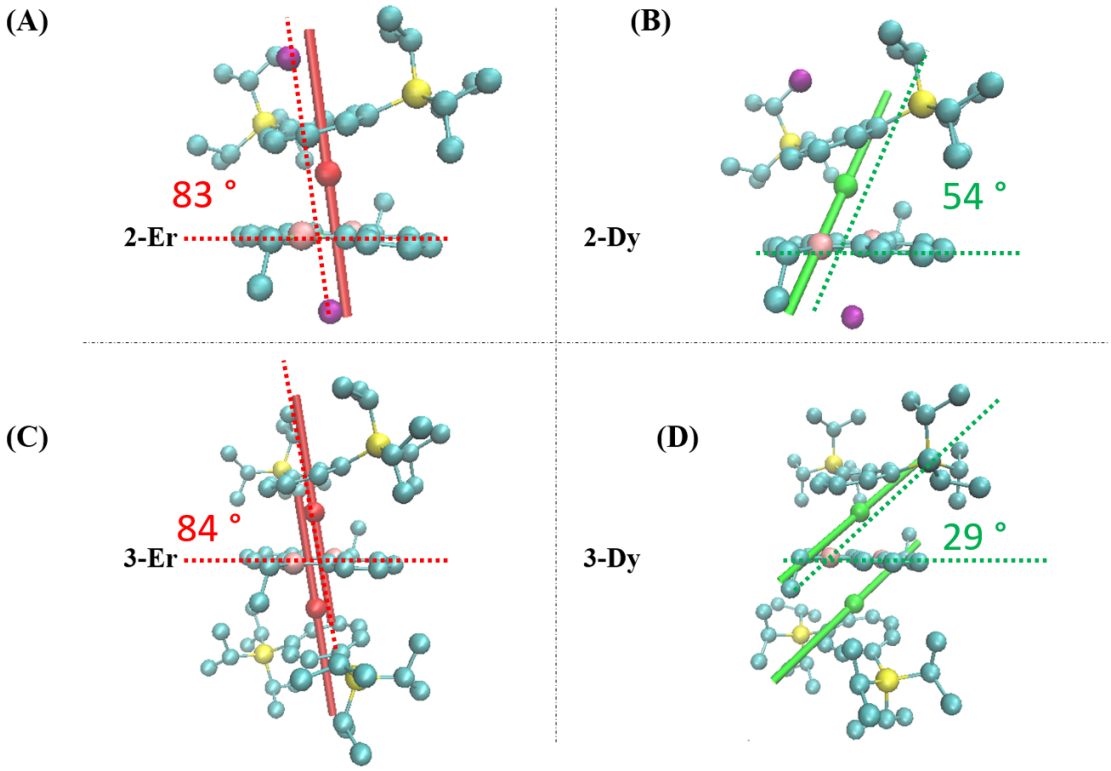

Figure 27: Plotted magnetic main axes of the ground KDs of 2-Er(A), 2-Dy(B), 3-Er(C) and 3-Dy (D). (C: cyan; Si: yellow; K: purple; B: pink; Er: red; Dy: green; hydrogen atoms are omitted for clarity)

	2-Er		2-Dy	
	g-values (g_x, g_y, g_z)	Energy level (cm^{-1})	g-values (g_x, g_y, g_z)	Energy level (cm^{-1})
1st KD	0.00 0.00 17.81	0.00	0.00 0.00 19.79	0.00
2nd KD	0.11 1.56 10.76	145.24	0.22 0.53 14.90	89.76
3rd K	1.73 3.99 8.81	148.02	0.30 1.04 15.61	114.33
4th KD	5.93 4.56 2.41	183.40	1.40 2.19 12.04	168.38
5th KD	0.33 0.77 11.42	224.61	4.22 5.99 10.56	193.72
6th KD	0.14 0.45 11.24	240.81	0.96 1.66 15.88	246.73
7th K	0.05 0.19 16.76	352.03	0.05 0.14 19.59	373.91
8th KD	0.07 0.16 16.81	374.43	0.01 0.03 19.73	425.79

Table 9: Calculated g-values of the first 8 KDs of 2-Er and 2-Dy with corresponding energy.

	3-Er		3-Dy	
	g-values (g_x, g_y, g_z)	Energy level (cm^{-1})	g-values (g_x, g_y, g_z)	Energy level (cm^{-1})
1st KD	0.00 0.00 17.88	0.00	0.01 0.03 19.41	0.00
2nd KD	0.01 0.02 16.44	147.99	0.83 1.71 16.38	75.81
3rd K	1.52 2.75 13.55	241.99	0.42 2.20 13.71	97.18
4th KD	0.16 2.40 10.45	269.35	8.45 6.78 4.63	134.27
5th KD	7.77 4.93 1.51	305.33	1.15 2.79 15.35	172.11
6th KD	1.44 2.16 8.45	337.34	0.53 1.04 14.14	206.20
7th KD	0.21 4.89 11.53	420.40	0.00 0.00 17.35	379.41
8th KD	0.03 4.73 11.78	431.21	0.00 0.00 19.86	845.89

Table 10: Calculated g-values of the first 8 KDs of 3-Er and 3-Dy with corresponding energy.

For dimers, the distance between the two spin centers is 4.5 Å in 3-Er and 4.6 Å in 3-Dy. The drop of $\chi_M T$ at low temperature indicates an antiferromagnetic coupling between two magnetic centers. The coupling behaviour between the two magnetic centers in dimers was further investigated. DFT-BS and CASOCI calculations were performed to calculate exchange and dipolar coupling constants between the magnetic centers in the dimers.

The isotropic exchange coupling constants J_{ex}^{Gd} (Ln^{3+} substituted by Gd^{3+}) of 3-Er and 3-Dy are -0.61 and -0.56 cm^{-1}, respectively. With the approach from Chibotaru *et al.*,[144] the exchange coupling constant of the model Gd complex can be converted to Ising type coupling constant between the ground doublets with eq. 79.[144] Where J_{Lines} and S_{real} are the coupling constant between the ground RS states and the real spin of the Ln^{3+}. J_{model} is the isotropic coupling constant calculated for the model complex (here Gd substitution was used) using the DFT-BS approach and S_{model} is the spin of Gd^{3+}. J_{Ising} is the coupling constant of the ground doublets, $S_{pseudospin}$ is the pseudospin of the doublets (here S_{pseudo}=1/2). ϕ is the angle between the two magnetic main axes of the ground states. First, to convert the coupling constant from the model system to the Lines model of the real complexes, the spin ground state S=3/2 and 5/2 need to be considered for Er^{3+} and Dy^{3+} ions. For the magnetic relaxation process, the low temperature interaction between the spin centers is of the most interest. Therefore, the Ising type coupling between the ground KDs is preferred, which can be calculated using S_{pseudo}=1/2. Here, the ground state main axes of the two centers are parallel (ϕ=0).

$$\begin{aligned} J_{Lines} &= \frac{S_{model}^2}{S_{real}^2} J_{model} \\ J_{Ising} &= \frac{S_{real}^2}{S_{pseudo}^2} cos\phi J_{Lines} \end{aligned} \tag{79}$$

The calculated dipolar coupling constants J_{dip} between the ground KDs of individual centers are 1.4 cm^{-1} and 0.49 cm^{-1} in 3-Er and 3-Dy, respectively. The total coupling constants of the ground doublets are the sum of exchange and dipolar coupling, which are -28.62 and -27.24 cm^{-1} for 3-Er and 3-Dy (Table 11), respectively. The interaction between the two ions is antiferromagnetic in both complexes.

	J_{ex}^{Gd} (S=7/2)	J_{ex}^{Ising} (S=1/2)	J_{dip} (S=1/2)	J_{total} (S=1/2)
3-Er	-0.61	-30.09	1.47	-28.62
3-Dy	-0.56	-27.39	0.15	-27.24

Table 11: Calculated coupling constants (cm^{-1}) of 3-Er and 3-Dy.

With the extended Stevens operators (ESOs) obtained from the CASOCI calculations (Table A14), $\chi_M T$ plots of the dimers were simulated using PHI[148] with various exchange coupling constants (see Figure 28). In the absence of exchange coupling, the simulated $\chi_M T$ from PHI[148] agrees well with the CASOCI results. The antiferromagnetic coupling in the low temperature regime is clearly overestimated according to the exchange coupling constant obtained from the DFT-BS approach (Figure 28 green curve). This phenomenon is known in literature.[149] Comparing $\chi_M T$-T plots with various J_{ex} values assuming the experimental curve and estimated experimental J_{ex}= -0.01 and -0.03 cm^{-1} were obtained.

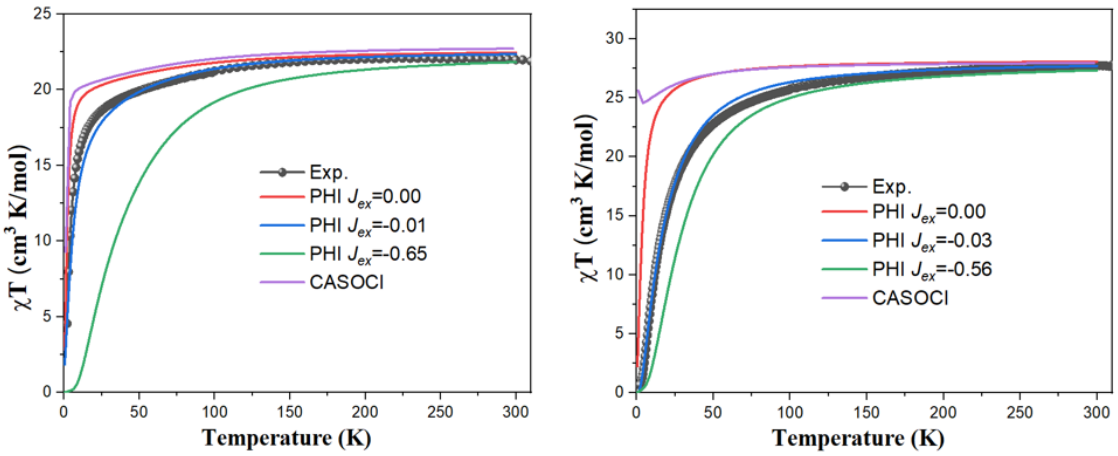

Figure 28: $\chi_M T$-T plots of complexes 3-Er (left) and 3-Dy (right). Black dots: Experiment; Purple curve: CASOCI including dipolar interaction of the ground state; Red curve: data simulated by PHI[148] with ESOs obtained from CAOSCI (in the absence of exchange coupling); Blue curve: data simulated with PHI[148] with the best fitting magnetic exchange coupling constants of J_{ex} = -0.01 cm^{-1} for Er and J_{ex} = -0.03 cm^{-1} for Dy, respectively. Green curve: data simulated with PHI[148] with the DFT-BS calculated isotropic exchange coupling constants.

The dynamic magnetic behaviour (Figure A2 and A3) of these complexes can be interpreted with the energies, g-factor and m_j compositions and coupling constants calculated in this section. The magnetic measurements were done by Dr. Kuppusamy from Prof. Ruben's group at Karlsruhe Institute of Technology and the data was analyzed by Dr. Moreno-Pineda at Universidad de Panamá. For 2-Er, 2-Dy and 3-Er, the temperature dependent relaxation time τ was fitted by eq. 80[150]

$$\tau^{-1} = \tau_0^{-1}\exp^{(\frac{U_{\text{eff}}}{k_B T})} + CT^n + \tau_{QTM}^{-1} \tag{80}$$

where U_{eff} is the magnetic reversal energy, k_B is Boltzmann constant, C and n are fitting parameters. The first to the third terms correspond to the Orbach, Raman and QTM relaxation processes.

In summary, 2-Er, 2-Dy and 3-Er show SMM characteristics, while 3-Dy shows no out-of-phase susceptibility signals. The presence of a second metal ion has opposite effects in 3-Er and 3-Dy. Notably, 3-Dy possesses the lowest excitation energy for the 2$^{\text{nd}}$ KD and the most mixed ground state. The weak coupling facilitates magnetic relaxation by further splitting the energy of the microstates, leading to smaller thermal barriers for the excited states, resulting in a loss of SMM behaviour. Additionally, 2-Er demonstrates superior SMM behavior compared to its Dy analogue, 2-Dy. Both complexes possess large ground state anisotropy. However, the excitation energy to the 2$^{\text{nd}}$ KD is higher in 2-Er than in 2-Dy. Lastly, when comparing 3-Er to its monomer counterpart, 2-Er, both the large anisotropy and the pure m_j=15/2 in the ground state are preserved in the dimer. While the coupling in the dimer also shifts the QTM process away from zero-field, resulting in even longer relaxation time because the QTM is quenched. This quenching of QTM is also observed in the alternating current (AC) magnetic susceptibility studies (Figure A3).

4.4 Diphosphaborole Lanthanide Complexes

In this section another four lanthanide sandwich complexes were investigated which were synthesized by Uhlmann from Prof. Roesky's group at Karlsruhe Institute of Technology. These complexes are similar to those in section 4.3 with the DBA ligand being replaced by the 2-phenyl-1,3,2-benzodiphosphaborole ligand (C4P2B). The C4P2B ligand carries a charge of -2, so as the COT$^{\text{TIPS}}$ ligand.

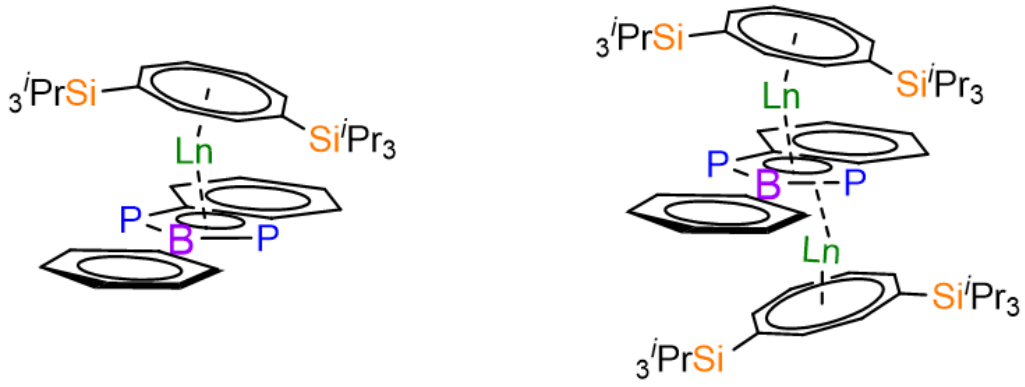

Figure 29: Structures of the four diphosphaborole rare-earth complexes investigated in this section.

Within one unit cell there are two counterion groups close to the molecule. The metal-Li distance is 5.2/5.1 Å for the nearest counterion and 5.7/5.6 Å for the second nearest in 4-Er/4-Dy. An investigation of the influence of counterions was carried out with three models in Figure 30. Ignoring the 2-phenyl group in the diphosphaborole ligand, the dimers possess C_s symmetry. The distances between the two spin centers are 4.8 Å and 4.7 Å in complex 5-Dy and 5-Er, respectively.

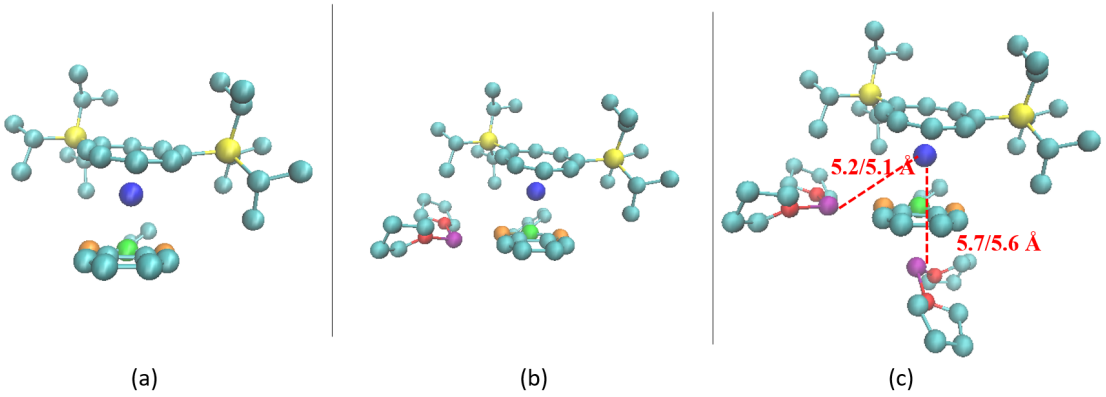

Figure 30: Illustration of three models for 4-Er/Dy are shown. The models are model A without counterion, model B with one counterion and model C with two counterions. (C: cyan; Si: yellow; Li: purple; B: green; P: orange; Er/Dy: blue; hydrogen atoms are omitted for clarity).

4.4.1 Energy Levels

The energy splitting of the $^4I_{15/2}$ state of 4-Er and $^6H_{15/2}$ of 4-Dy, calculated in the aforementioned model complexes, is depicted in Figure 31. The presence of counterions influences the energies of the first excited KD differently in 4-Er and 4-Dy. For 4-Er, the energy of the first KD increases from 70.1 cm^{-1} when no counterion is present, to 106.6 cm^{-1} with one counterion, and amounts to 116.6 cm^{-1} with both counterions present. However, the first excited energy is the highest in the model B with 77.2 cm^{-1} for 4-Dy. While the energies are 37.0 and 44.5 cm^{-1} in model A and model C, respectively.

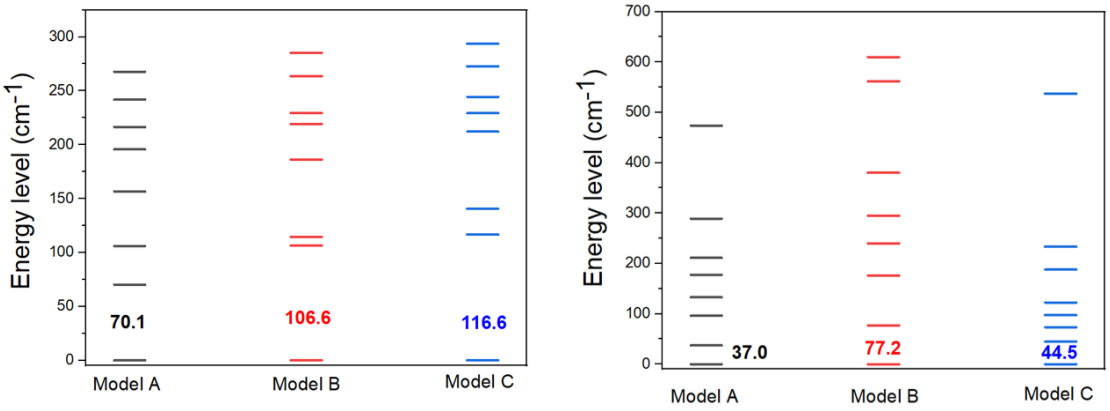

Figure 31: Calculated energy levels (cm^{-1}) of the ground 15/2 states of the 4-Er (left) and 4-Dy (right) complexes with no counterions (model A), one counterion (model B) and with two counterions (model C). Calculated with ROHF-optimized orbitals.

With the calculated ground KD g-factors in Table 12, more insights are obtained. For 4-Er, the ground state magnetic anisotropy increased slightly when more counterions were included. The g_z values increase from 17.71 to 17.76 while the g_x and g_y values decrease. For 4-Dy, the ground state is the least anisotropic when only one counterion is taken into account, with g_x=0.33, g_y=0.74 and g_z=18.69. The ground states of model A and model C possess similar magnetic anisotropy, with g_x=0.02, g_y=0.03 and g_z=19.51 for model A and g_x=0.01, g_y=0.02 and g_z=19.43 for model C.

The number of counterions around the molecule has an impact on the crystal field splitting and the ground state anisotropy, especially for 4-Dy. The magnetic anisotropy of the ground state is diminished when only one counterion is present (model B). The model B can not accurately describe the crystal structure nor the electronic state.

Therefore, it is excluded in the future discussion. In the following, we examine the results obtained with two counterions (model C), chosen due to its resemblance to the charge distribution in the crystal structure.

	4-Er			4-Dy		
	Model A	Model B	Model C	Model A	Model B	Model C
g_x	0.004951	0.002701	0.001663	0.02213	0.330644	0.01157
g_y	0.011333	0.005224	0.00318	0.029897	0.747279	0.015951
g_z	17.71924	17.75299	17.75723	19.50518	18.69209	19.43479

Table 12: Calculated g-factors of the ground KDs of 4-Er and 4-Dy in different models. Calculated with ROHF-optimized orbitals.

First of all, the energies calculated from each metal center with the other center as a diamagnetic substitution in the dimers are identical (Figure 32, Left). The metal centers are in equivalent coordination surroundings, which is also inferred from the molecular symmetry. Therefore, the future calculations are conducted for one of the center in the dimers. The energy levels of the lowest eight KDs of 4-Er, 4-Dy, 5-Er and 5-Dy are given in Figure 32. A similar trend can be observed in these four complexes as in the last section. First, the energies of the 2nd KDs are higher when calculated based on CASSCF-optimized orbitals in all complexes. Furthermore, the energy of the 2nd KD is the highest in 5-Er (173.94 cm^{-1}) and the lowest in 5-Dy with 11.8 cm^{-1} only (Figure 32). The energy is for 4-Er is 150.68 cm^{-1} while it is 54.37 cm^{-1} in 4-Dy.

It is shown from the work of Cucinotta *el al.*[147] that the energy of the second KD is influenced by the change of the water molecule orientation in the second coordination sphere. From the monomer to the dimer, a significant change occured in the second coordination sphere. The two negative charged counterions were replaced by another Dy^{3+} and COT ligand plane with a charge of -2. The change in the second coordination sphere from Dy monomer to Dy dimer caused the decrease the first excited energy. This phenomenon is also observed in the $Dy_2(COT")^3$ complex.[145]

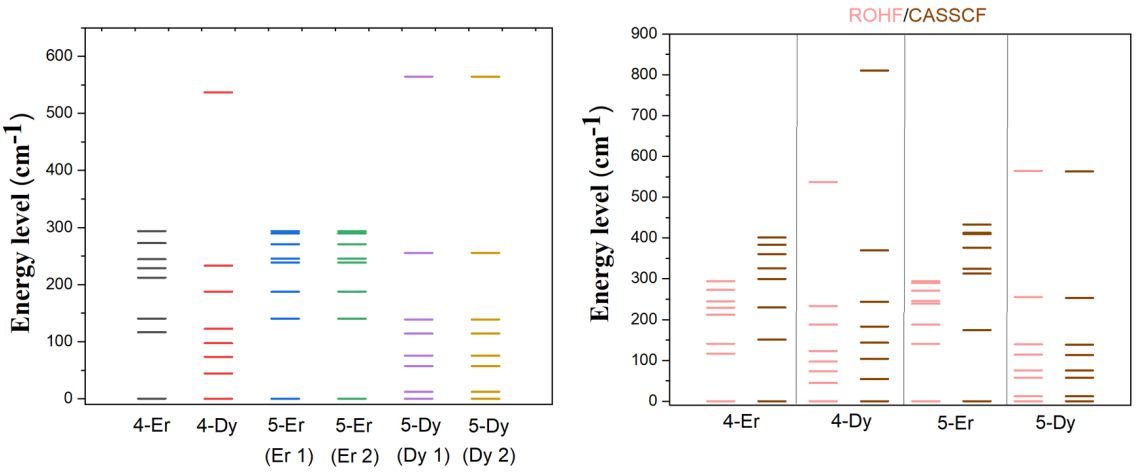

Figure 32: Left: Calculated energy levels (cm^{-1}) of the first eight KDs in 4-Er, 4-Dy, 5-Er and 5-Dy with ROHF-optimized orbitals (for 3-Er and 3-Dy, the calculation is done on one of the spin centers with the other center substituted by diamagnetic Y^{3+}). Right: Calculated energy levels (cm^{-1}) of the first eight KDs in 4-Er, 4-Dy, 5-Er and 5-Dy with ROHF-optimized (pink) and CASSCF-optimized (brown) orbitals.

4.4.2 Magnetic Properties

The calculated and measured temperature dependent molar magnetic susceptibility $\chi_M T$ verses temperature (T) of the four complexes are plotted in Figure 33. In all complexes, the room temperature $\chi_M T$ agrees with the measured magnetic data. In the low temperature range, a gap between the experimental and calculated $\chi_M T$ was observed in the dimers, which indicates an antiferromagnetic interaction.

The ground KDs of Er^{3+} possess large magnetic anisotropy in both 4-Er and 5-Er with g_x=g_y=0 and g_z=17.81 and 17.89, respectively. Notably, the ground KDs are predominantly composed of m_j=±15/2 states with 97.8% and 99.1%, respectively (Table A10 and A12). Furthermore, the magnetic main axes (Table A5) in the ground KDs of 4-Er and 5-Er are almost perpendicular to the C4P2B ligand plane with angles of 74 and 82 °, respectively (Figure 34).

However, for the Dy complexes 4-Dy and 5-Dy, the magnetic main axes of the ground KDs are more tilted, with 30.4 ° and 9 ° to the C4P2B ligand plane. The ground states are also less anisotropic with increased g_x and g_y values. For 4-Dy, the ground states g-values are g_x=0.04, g_y=0.05 and g_z=19.66 (Table 13). g_x and g_y in the ground state of 5-Dy further increase to g_x=0.36 and g_y=1.44 while g_z decreases

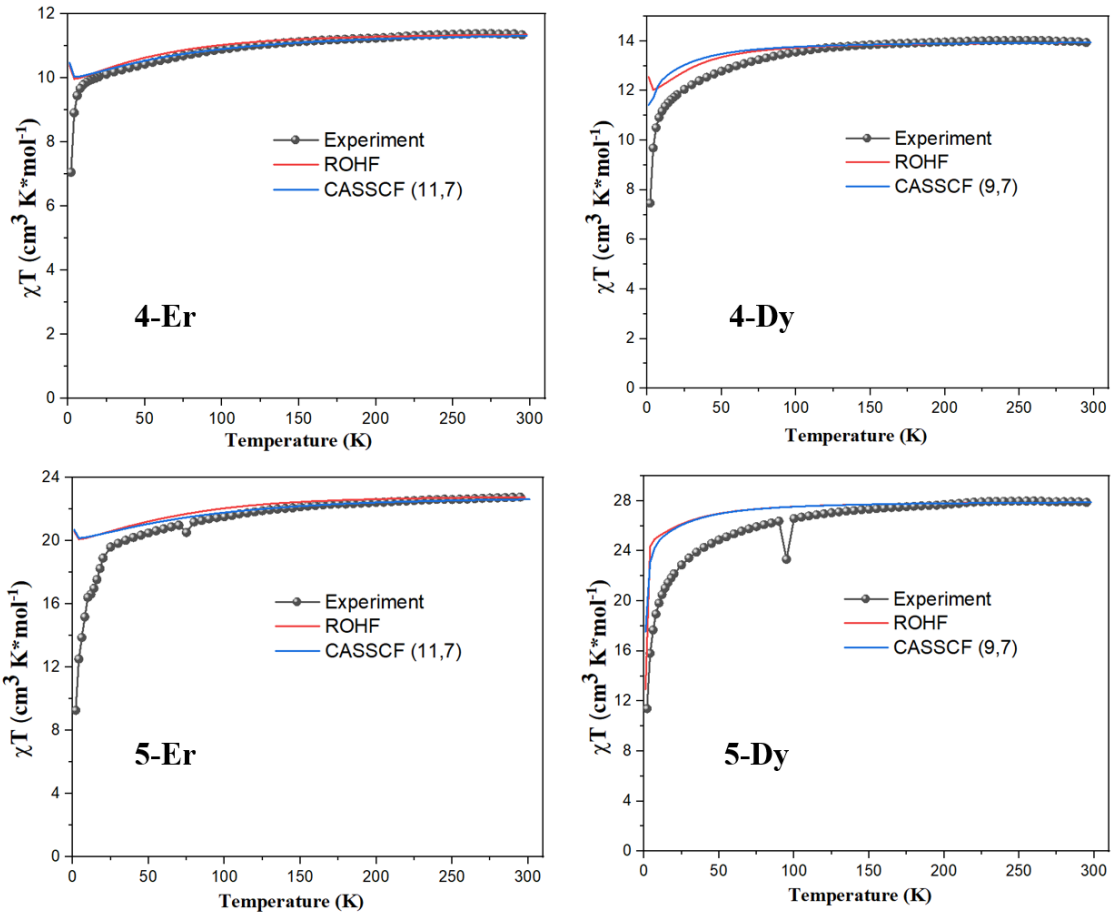

Figure 33: Measured and calculated magnetic susceptibility $\chi_M T$-T of 4-Er, 4-Dy, 5-Er and 5-Dy.

to 18.32 (Table 14). Although the dominant composition in the ground states is still m_j=±15/2 in both Dy complexes, with 98.3 % in 4-Dy (Table A11) and 80.1 % in 5-Dy (Table A13). But the percentage is significantly lower in 5-Dy comparing to other complexes. For 5-Dy, the ground state is a mixture of 80.1 % m_j=±15/2, 11.2% m_j=±11/2, 6.1 % m_j=±9/2, 1.2 % m_j=±13/2 and less than 1% from doublets with other m_j values.

As mentioned in section 4.3, The anisotropic axes of Dy^{3+} are sensitive to the second coordination sphere.[145,147] In the dimer 5-Dy, the loss of axial direction counterions further destabilize Dy^{3+} in the sandwich-type ligands.

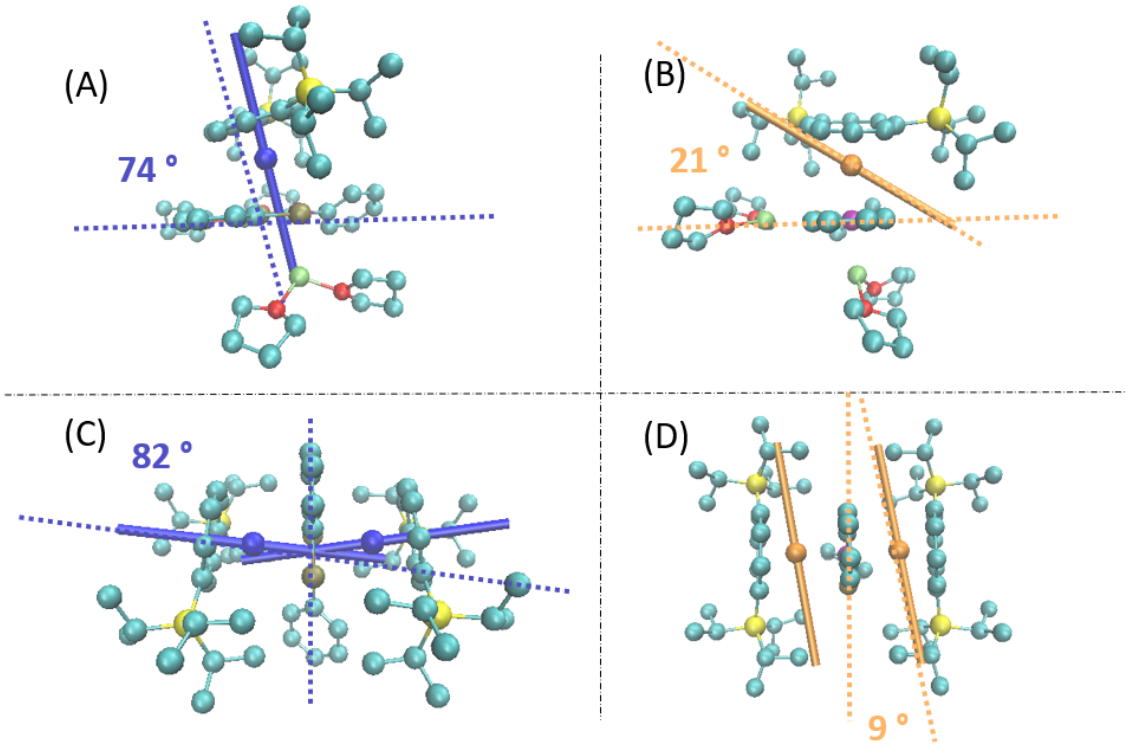

Figure 34: Plotted magnetic main axes of the ground KD of 4-Er complex (A), 4-Dy complex (B), 5-Dy (C) and 5-Er (D). (C: cyan; Si: yellow; O: red; Li: green; B: purple; Er: blue; Dy: orange; hydrogen atoms are omitted for clarity).

	4-Er		4-Dy	
	g-values (g_x, g_y, g_z)	Energy level (cm^{-1})	g-values (g_x, g_y, g_z)	Energy level (cm^{-1})
	0.00		0.04	
1st KD	0.00	0.00	0.05	0.00
	17.81		19.66	
	0.01		0.15	
2nd KD	0.01	150.68	0.25	54.37
	15.62		18.25	
	0.14		0.81	
3rd KD	0.35	229.64	1.60	103.88
	16.79		14.14	
	1.66		8.94	
4th KD	1.86	299.63	6.93	143.24
	11.18		3.73	
	3.01		0.97	
5th KD	4.99	325.97	1.80	182.87
	7.51		9.75	
	0.37		0.31	·
6th KD	3.53	360.04	0.45	243.45
	6.81		16.23	
	0.35		0.02	
7th KD	1.69	383.18	0.03	369.49
	9.75		17.11	
	0.69		0.00	
8th KD	1.91	401.11	0.00	810.45
	12.26		19.88	

Table 13: Calculated g-factors of the lowest 8 KDs of 4-Er and 4-Dy with corresponding energy.

	5-Er		5-Dy	
	g-values (g_x, g_y, g_z)	Energy level (cm^{-1})	g-values (g_x, g_y, g_z)	Energy level (cm^{-1})
1st KD	0.00 0.00 17.89	0.00	0.36 1.44 18.32	0.00
2nd KD	0.00 0.00 15.61	173.94	0.56 1.10 16.86	11.80
3rd KD	0.73 1.10 14.88	312.81	1.82 4.14 13.95	57.30
4th KD	0.09 1.11 11.79	324.61	2.93 6.12 9.77	75.13
5th KD	8.90 6.33 2.37	375.74	0.54 1.60 10.52	113.17
6th KD	0.88 2.14 4.99	409.46	0.45 0.71 17.09	· 138.50
7th KD	0.14 0.95 9.27	412.46	0.00 0.00 17.29	252.98
8th KD	0.47 1.44 8.23	432.79	0.00 0.00 19.89	562.77

Table 14: Calculated g-factors of the lowest 8 KDs of 5-Er and 5-Dy with corresponding energy.

The isotropic exchange coupling constants J_{ex}^{Gd} of the Gd model complex is -0.21 cm^{-1} for both 5-Er and 5-Dy. Following the procedure presented in eq. 79 from the section 4.3, the Ising type coupling constant is calculated. The angles between two ground KDs magnetic main axes are 16.5° and 6.9° for 5-Er and 5-Dy, respectively. Eventually, the exchange coupling constant are -9.8 and -10.2 cm^{-1} for the ground doublets of 5-Er and 5-Dy. The calculated dipolar coupling constant J_{dip} between the ground KDs are 1.8 cm^{-1} and -0.60 cm^{-1} in 5-Er and 5-Dy, resulting in total coupling constant of -8.52 and -10.8 cm^{-1}, respectively (see Table 15).

Figure 35 shows the simulations of $\chi_M T$ were also done by PHI[148] with *ab initio* calculated extended Stevens Operators (see Table A15). As expected the DFT-BS approach overestimated the exchange coupling constants. The best fitted isotropic exchange coupling constants are -0.01 cm^{-1} for 5-Er while for 5-Dy it differs at low and high temperatures.

	J_{ex}^{Gd} (S=7/2)	J_{ex}^{Ising} (S=1/2)	J_{dip} (S=1/2)	J_{total} (S=1/2)
5-Er	-0.21	-9.8	1.8	-8.52
5-Dy	-0.21	-10.2	-0.60	-10.8

Table 15: Calculated coupling constants (cm^{-1}) of 5-Er and 5-Dy.

The dynamic magnetic measurements were conducted by Dr. Demeshko at the University of Göttingen. The results are shown in Figure A4 and A5. Similar to those complexes in section 4.3, the Dy dimer (5-Dy) exhibits no SMM behaviour while the Er dimer (5-Er) shows the best SMM performance among them. The absence of AC magnetic susceptibility of 5-Dy can be explained by its small zero-field splitting (11.8 cm^{-1}) to the first excited microstate and a highly mixed ground state. The weak interaction between the Dy^{3+} further splits the quasi-degenerate first and second microstates of one Dy^{3+} into more states, which drives the energy of the first excited state further down. Although QTM might be suppressed, the almost barrier-free microstates provide more relaxation pathways. However, the presence of weak interaction in the Er dimer results in a shift of QTM to higher field, thus, QTM is quenched in zero-field.

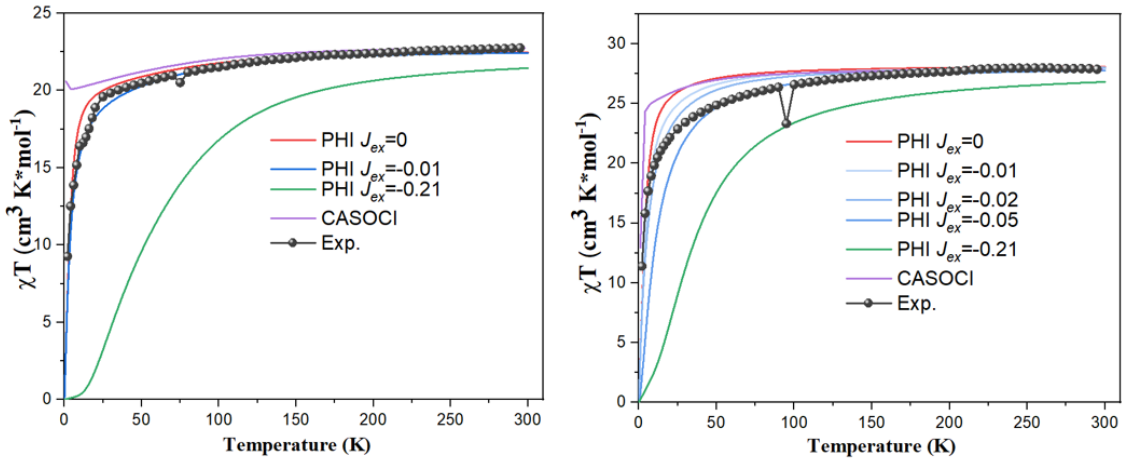

Figure 35: $\chi_M T$-T plots of complexes 5-Er (left) and 5-Dy (right). Black dots: Experiment; Purple curve: CASOCI including dipolar interaction of the ground state; Red curve: data simulated by PHI[148] with the Stevens parameters obtained from CAOSCI (in the absence of exchange coupling); Blue curve: data simulated with PHI[148] with the best fitting magnetic exchange coupling constants of J_{ex} = -0.01 cm^{-1} for 5-Er, but for 5-Dy no good fit across the measured temperature range was obtained by only one J_{ex} value. Green curve: data simulated with PHI[148] with the DFT-BS calculated isotropic exchange coupling constants.

4.5 Trinuclear Ion complex

In this section, a trinuclear ion complex (Figure 36) was investigated. This complex was synthesized by Dr. Gracia from Dr. Bizzari's group in Karlsruhe Institute of Technology. The complex contains three Fe^{2+} (d^6, high-spin configuration) cations as the metal centers. Each Fe^{2+} is in a distorted octahedral ligand field. The two iron centers on either side are in equivalent coordination environments with six nitrogen atoms in the first coordination sphere. The iron center in the middle has a different ligand field with four nitrogen and two sulfur atoms in the first coordination sphere. The trinuclear complex possess C_i molecular symmetry.

The mononuclear precursor was also investigated (Figure 37 A). The monomer differs from the mononuclear model (Model-Fe1/Fe3) of the trimer by one coordinating molecule. In the monomer, a pyridine molecule is coordinating while in the trinuclear compound it is acetonitrile (MeCN). Three mononuclear model complexes (see Figure 37) based on the simplified trinuclear complex were studied first. The metal-ligand distances are given in Table 16. For all model complexes, the metal centers are in a

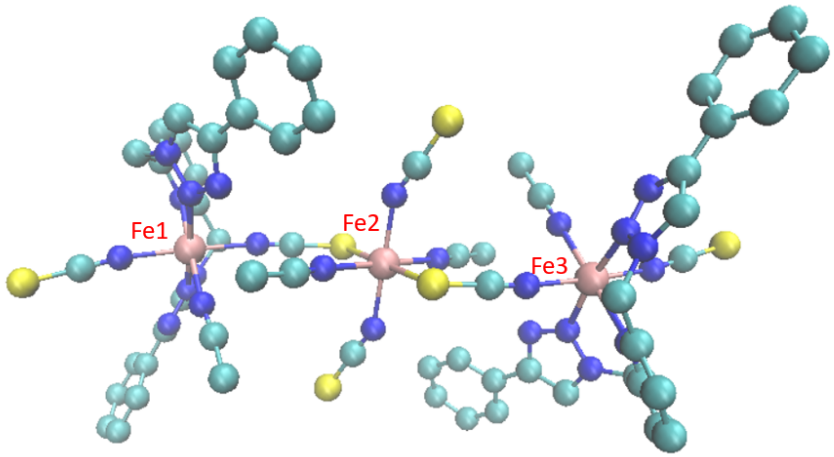

Figure 36: The crystal structure of trinuclear ion complex. (C: cyan; S: yellow; N: blue; Fe: pink; hydrogen atoms are omitted for clarity).

distorted orthorhombic ligand field. The electronic and magnetic properties of models with single spin centers were calculated separately. Finally, the interactions between pairs of spin centers were investigated.

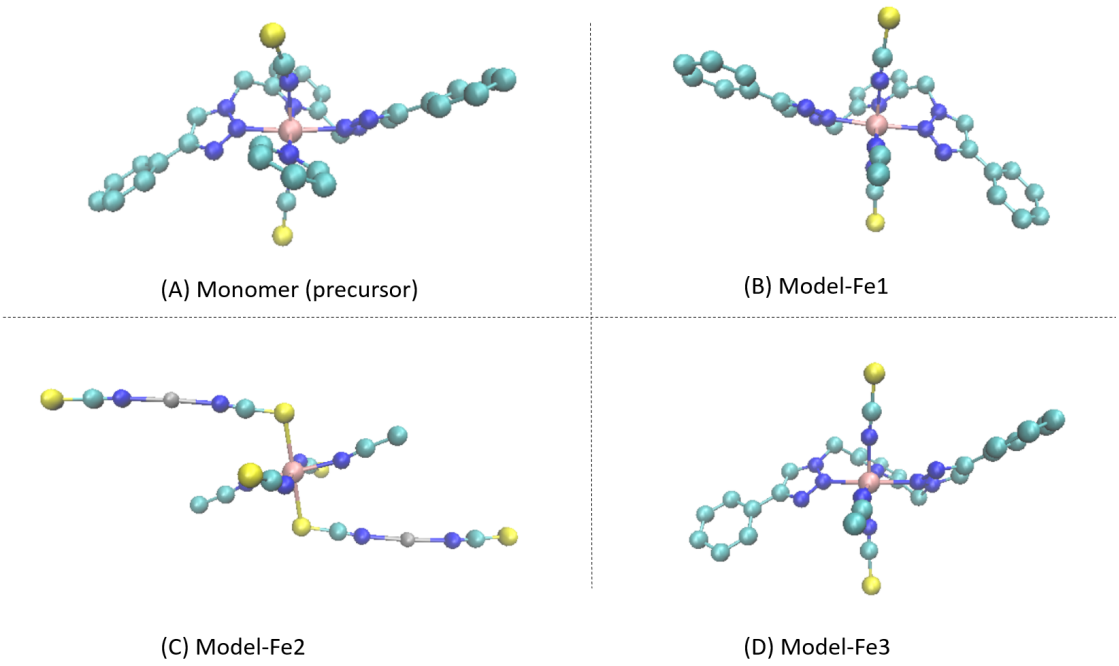

Figure 37: Structure of precursor mononuclear complex (A), mononuclear model complexes (B-D) taken from the trinuclear complex. (C: cyan; S: yellow; N: blue; Fe: pink; Zn: silver; hydrogen atoms are omitted for clarity).

Monomer	Model-Fe1	Model-Fe2	Model-Fe3
2.11	2.08	2.08	2.08
2.11	2.08	2.08	2.09
2.19	2.18	2.19	2.18
2.19	2.18	2.19	2.18
2.19	2.19	2.65*	2.19
2.31	2.30	2.65*	2.30

Table 16: The metal-ligand distance (Å) between Fe and its direct neighbouring atom. *: S is coordinated with Fe instead of N in other cases.

4.5.1 Energy Levels

Without the ligand field, Fe^{2+} with high spin configuration has a ^5D ground state. In octahedral coordination, the ^5D ground state is spitted into a three-fold degenerate $^5T_{2g}$ state and a two-fold degenerate ^5E_g state. In an orthorhombic distorted O_h symmetry, the degeneracy is further lifted (illustrated in Figure 38), resulting in three states close in energy, and another two that are energetically isolated from the first three states.

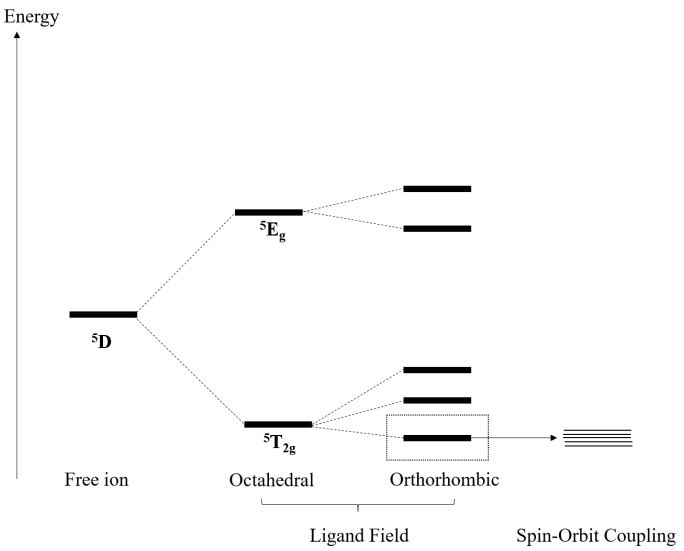

Figure 38: Illustration of the Energy Levels of Fe^{2+} high spin configuration. Adapted from reference[151] Figure 2.

In an octahedral field, $3d$ orbitals will split into three t_{2g} and two e_g orbitals with the t_{2g} orbitals being lower in energy (see Figure 39).

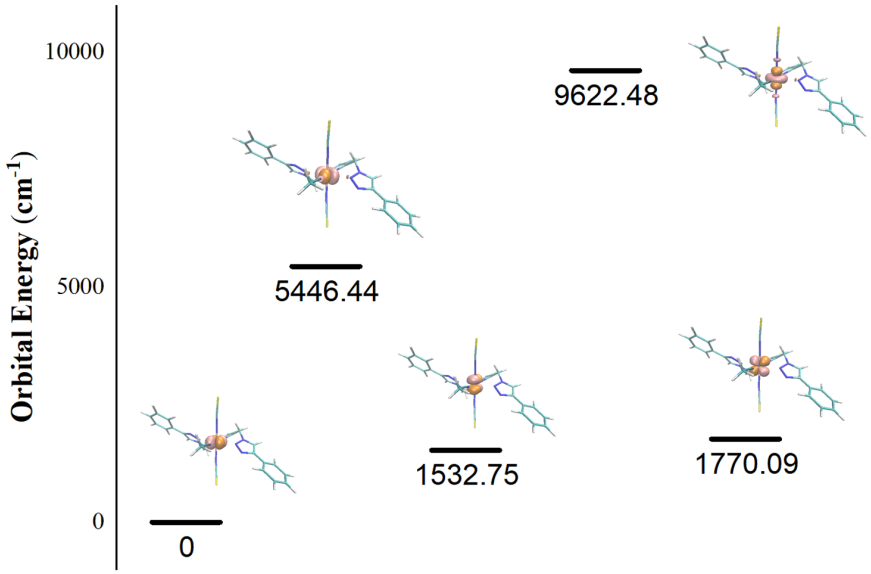

Figure 39: Plotted Fe 3d orbitals (ROHF optimized) of Model-Fe1 and their corresponding relative energy to the lowest orbital energy.

In the mononuclear complex and model complexes, the Fe^{2+} is in an orthorhombic surrounding. The calculated CASOCI energy levels (Table 17) agree with the energy splitting pattern of high spin Fe^{2+} in the orthorhombic field. When SOC is not considered, there are three $^5T_{2g}$ states lower in energy and two ^5E_g states well separated from the lower states, with each state being five-fold degenerate. The three $^5T_{2g}$ states exhibit a maximal energy gap up to around 2000 cm^{-1} (in monomer, Model-Fe1 and Model-Fe3) or 2800 cm^{-1} (in Model-Fe2). The ^5E_g states are separated from the highest $^5T_{2g}$ states by an energy gap of around 6000 cm^{-1} in monomer, Model-Fe1 and Model-Fe3 whereas it is 3000 cm^{-1} in Model-Fe2. Comparing the Energy Levels of Model-Fe1 and Model-Fe3, one can tell the chemical environments of the Fe1 and Fe3 are identical.

For 3d elements, SOC plays a minor role in the energy splitting. This effect can also be seen from our calculation. The maximum energy splitting for the ground $^5T_{2g}$ state caused by SOC is about 11 cm^{-1} for Model-Fe1/Model-Fe3 and around 22 cm^{-1} for Model-Fe2. However, for the monomer complex the energy splitting caused by SOC is up to 76 cm^{-1}. The energy levels of the first and second microstates are around 0 while the third microstate is separated by an energy gap of 52 cm^{-1}.

Monomer		Model-Fe1		Model-Fe2		Model-Fe3	
SOC free	SOC	SOC free	SOC	SOC free	SOC	SOC free	SOC
	0		0				0
	0.295		0.118		0.227		0.118
0	52.192	0	6.843	0	15.306	0	6.841
	60.572		9.157		17.779		9.155
	76.356		10.848		22.21		10.846
	1686.625		1727.335		2660.428		1727.222
	1689.614		1729.736		2661.829		1729.624
1726.607	1796.252	1825.315	1790.882	2793.342	2725.935	1825.188	1790.761
	1830.183		1834.363		2768.397		1834.246
	1870.173		1862.561		2814.332		1862.432
	2144.341		1994.751		2877.263		1994.67
	2169.936		2027.666		2931.561		2027.574
2035.842	2210.607	1962.3	2064.442	2849.883	2969.983	1962.219	2064.351
	2274.478		2136.732		3057.939		2136.635
	2277.701		2138.266		3058.471		2138.169
	8815.208		8404.294		5876.685		8404.216
	8815.57		8404.682		5876.996		8404.604
8768.775	8856.401	8356.197	8406.967	5817.602	5886.672	8356.118	8406.889
	8864.415		8409.364		5890.156		8409.286
	8875.864		8409.687		5892.427		8409.609
	11758.23		12497.17		12161.23		12497.1
	11767.51		12497.28		12161.64		12497.21
11659.96	11769.98	12115.31	12500.26	12115.31	12164.94	12455.03	12500.19
	11799.55		12501.53		12167.82		12501.46
	11799.59		12502.19		12168.35		12502.12

Table 17: Calculated CASOCI energy (cm^{-1}) of mononuclear model complexes.

Two one-spin-center complexes whose structures are based on the full complex with two Fe^{2+} centers substituted by Zn^{2+} (named Fe1-Zn2-Zn3 and Zn1-Fe2-Zn3 in Figure 40) were investigated. Energy levels were calculated and compared to those based on the model structures in Table 18. The energy deviation of the same ion center in

model and real complex is negligible in the lowest five states. The energy deviations are larger for higher energy states and amount to around 150 cm^{-1} when comparing between the peripheral ion center (Fe1) in model and full structure complexes. The deviation increases to around 500 cm^{-1} when comparing the energy calculated for the middle center (Fe2). However, the subsequent states are considerably distant from the lowest five states, exhibiting a gap ranging from 1000 to 3000 cm^{-1}. Regarding magnetic properties, the low-lying states are with particular attention because they can be thermally populated within the temperature range in which measurements are conducted.

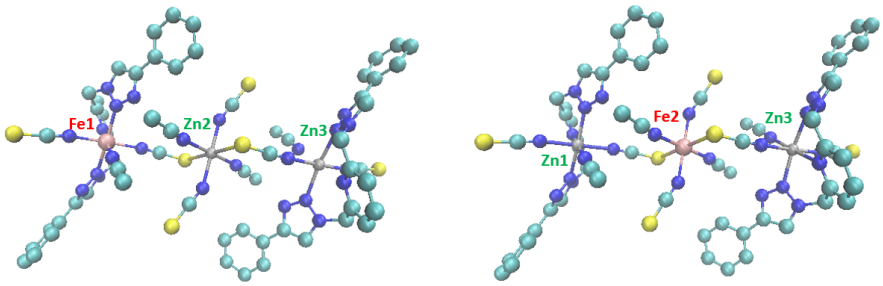

Figure 40: Illustration of one-spin-center complexes Fe1-Zn2-Zn3 and Zn1-Fe2-Zn3 based on the full complex with diamagnetic substitutions. (C: cyan; S: yellow; N: blue; Fe: pink; Zn: silver; hydrogen atoms are omitted for clarity).

Model-Fe1	Fe1-Zn2-Zn3	Model-Fe2	Zn1-Fe2-Zn3
0.00	0.00	0.00	0.00
0.12	0.18	0.23	0.41
6.84	5.90	15.31	11.71
9.16	9.07	17.78	15.73
10.85	10.28	22.21	18.62
1727.34	1570.05	2660.43	2181.75
1729.74	1572.91	2661.83	2185.54
1790.88	1631.15	2725.94	2229.39
1834.36	1676.29	2768.40	2269.67
1862.56	1700.26	2814.33	2282.76
1994.75	1851.90	2877.26	2533.58
2027.67	1880.75	2931.56	2550.86
2064.44	1917.03	2969.98	2595.02
2136.73	1986.02	3057.94	2655.09
2138.27	1987.78	3058.47	2659.24
8404.29	8422.47	5876.69	6101.35
8404.68	8422.87	5877.00	6101.37
8406.97	8425.16	5886.67	6110.46
8409.36	8427.61	5890.16	6111.61
8409.69	8427.93	5892.43	6114.24
12497.17	12344.80	12161.23	11651.67
12497.28	12344.92	12161.64	11651.97
12500.26	12347.83	12164.94	11655.50
12501.53	12349.16	12167.82	11657.95
12502.19	12349.79	12168.35	11658.60

Table 18: Calculated CASOCI energy (cm^{-1}) of mononuclear model complexes Model-Fe1, Model-Fe2, and one-spin-center complexes Fe1-Zn2-Zn3 and Zn1-Fe2-Zn3 based on the full complex.

4.5.2 Magnetic Properties

The calculated $\chi_M T$-T of one-spin-center and multi-spin-center complexes are plotted in Figure 41 and Figure 43. The room temperature $\chi_M T$ of Model-Fe2 exhibits

notable differences from those calculated in other one-spin-center complexes. The drastic structure simplification in Model-Fe2 underestimates $\chi_M T$ compared to the real complex.

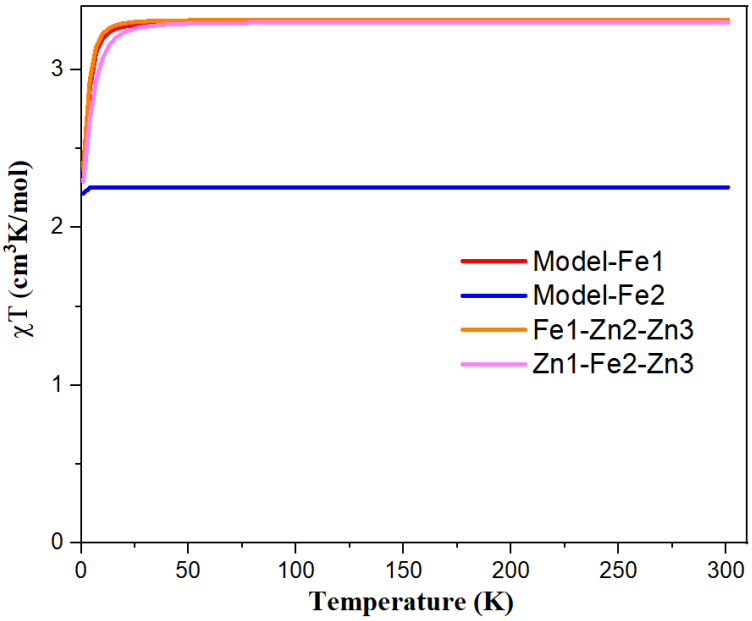

Figure 41: Calculated $\chi_M T$-T of mononuclear models and one-spin-center complexes based on the structure of full complex.

Two-spin-center complexes (Fe1-Fe2-Zn3 and Fe1-Zn2-Fe3 in Figure 42) were also investigated to study the magnetic coupling between each pair of spin centers separately. The $\chi_M T$ of two-spin-center complexes is plotted in Figure 43 (A). The calculated $\chi_M T$ for Fe1-Zn2-Fe3 completely overlaps with the $\chi_M T$ of the single-center complexes Fe1-Zn2-Zn3 multiplied by two. For the complex Fe1-Fe2-Zn3, where Fe^{2+} ions are direct neighbours, the calculated $\chi_M T$ decreases more than in Fe1-Zn2-Fe3 at low temperatures. The decrease of $\chi_M T$ in Fe1-Fe2-Zn3 indicates an antiferromagnetic coupling between Fe1 and Fe2 and the constant $\chi_M T$ in Fe1-Zn2-Fe3 indicates negligible coupling between Fe1 and Fe3. The J_{ex} calculated by DFT-BS/CASOCI are -6.69/-0.16 cm^{-1} and 0.17/0.00 cm^{-1} between Fe1-Fe2 and Fe1-Fe3, respectively. The DFT-BS approach overestimates the exchange coupling constants while CASOCI underestimates them due to a lack of dynamic correlation.[65]

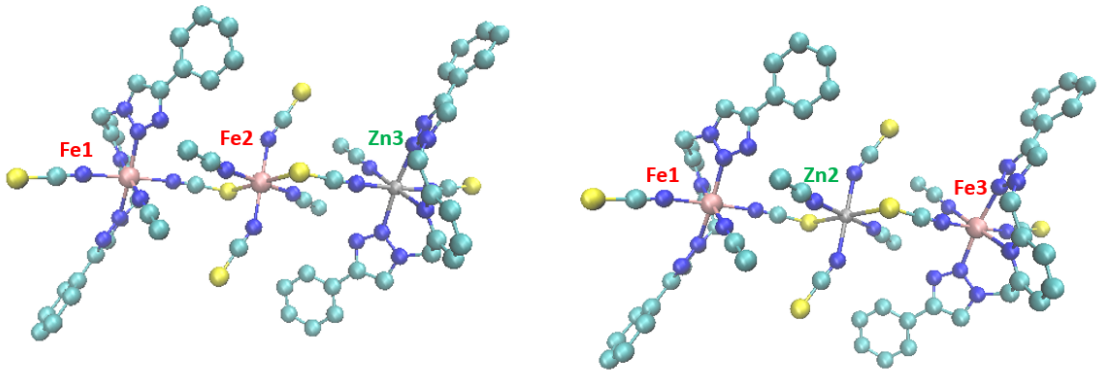

(A) Fe1-Fe2-Zn3 (B) Fe1-Zn2-Fe3

Figure 42: Illustration of two-spin-center complexes Fe1-Fe2-Zn3 and Fe1-Zn2-Fe3 based on the full complex with diamagnetic substitutions. (C: cyan; S: yellow; N: blue; Fe: pink; Zn: silver; hydrogen atoms are omitted for clarity).

The $\chi_M T$ of the full complex with three spin centers cannot be calculated directly due to computational limitation but can be approximated by the addition of each individual center and the coupling between Fe1-Fe2 and Fe2-Fe3. At room temperature, the calculated $\chi_M T$ reaches around 10.

g-factors, D and E parameters of individual spin center were obtained for the lowest five states (Table 19) because the next state is energetically separately by 1000 cm^{-1}. With these crystal field parameters, $\chi_M T$ of Fe complexes containing one, two and three high-spin Fe^{2+} centers were simulated with PHI.[148] These are compared with the CASOCI results in Figure 43. Due to the instability of samples, no experimental values were obtained for the Fe^{2+} trimer. In the absence of exchange couplings, the $\chi_M T$ simulated from PHI[148] and those calculated by the CASOCI program[16] show good agreement for systems with two Fe^{2+} centers (Figure 43, left). The simulated $\chi_M T$ values of the trimer are marginally elevated in the low-temperature regime (Figure 43, right). However, incorporating the exchange coupling constants derived from CASOCI energies to the simulation of $\chi_M T$ yields a close alignment with values calculated directly by the CASOCI method. The inclusion of exchange coupling constants obtained from the DFT-BS approach results in a notable reduction in the simulated $\chi_M T$ values. The measured $\chi_M T$ values are expected to fall between those simulated using exchange coupling derived from the DFT-BS method and those obtained from CASOCI energies with the shape similar to the form from DFT-BS.

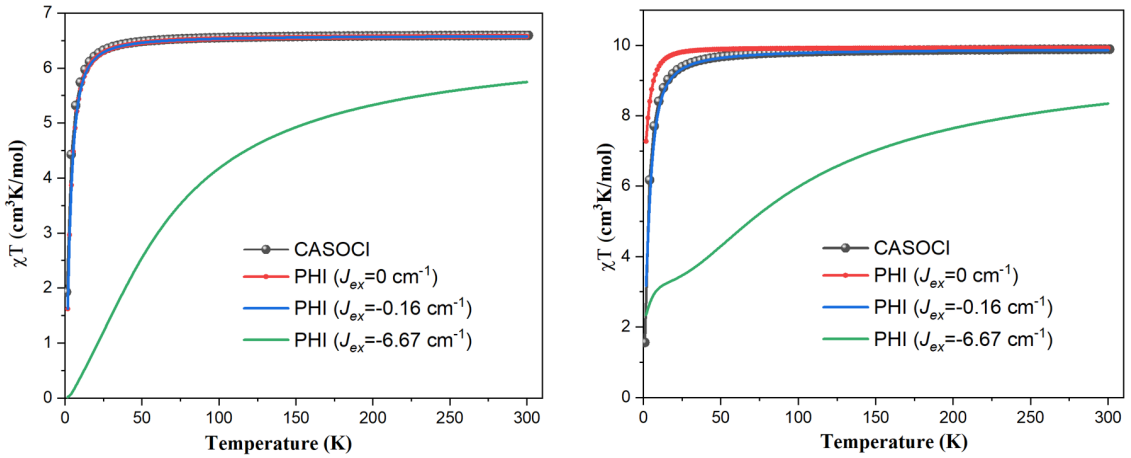

Figure 43: PHI[148] simulated and CASOCI calculated $\chi_M T$-T of two-spin-center complexes (left) and three-spin-center complexes (right). g-factors, D and E parameters used for PHI simulations are given in Table 19 4th and 5th columns.

	Monomer	Model-Fe1	Model-Fe2	Fe1-Zn2-Zn3	Zn1-Fe2-Zn3
g_x	2.01	2.11	2.06	2.12	2.07
g_y	2.08	2.11	2.08	2.11	2.09
g_z	2.37	2.07	2.13	2.07	2.12
D	-18.84	-2.62	-5.48	-2.39	-4.47
E	-1.34	-0.41	-0.42	-0.56	-0.67

Table 19: Calculated g-factors of the lowest five states in mononuclear model complexes and one-spin-center complexes.

4.6 Conclusions

Rinehart and Long[146] demonstrated that the electron density shape of lanthanide ions offers valuable insights into whether the ligand environment leads to high ground-state magnetic anisotropy. Er^{3+} exhibits a prolate-shaped electron density, whereas Dy^{3+} features an oblate-shaped electron density. An equatorial ligand coordination combined with a prolate-shaped electron density ion can lead to a highly anisotropic ground state.[146] Conversely, axial ligand coordination is more suitable for ions with an oblate-shaped electron density.[146] The lanthanide complexes investigated in this chapter

are equipped with equatorial ligand coordination (sandwich type), thus favouring the magnetic anisotropy of Er^{3+}. The metal-metal interactions can be utilized to suppress QTM,[5] even weak interaction can have a large influence.[152] The calculated energy barrier between the ground and first excited doublets is higher for Er complexes in most of the cases. Er-dimers generally exhibit higher energy barriers compared to their corresponding monomers. However, a decrease of the energies of the first excited KDs in dimers emerged in the Dy analogues. *Ab initio* calculations suggest that Er dimers are likely to exhibit favourable SMM characteristics, whereas Dy-dimers are anticipated to be less effective.

In experiments, all Er complexes are better SMMs compared to their Dy analogues, which collaborates with *ab initio* calculations. This phenomenon is known from complexes investigated previously in other research groups featuring similar ligands.[153] For Er monomers, Orbach, Raman and QTM were observed. QTM is suppressed in Er dimers (Figure A3 and A5). For Dy complexes, Orbach relaxation is absent and only Raman and QTM relaxation pathways were observed (Figure A2 and A4).

In most of the studied lanthanide complexes, the ground KDs exhibit significant magnetic anisotropy, with the m_j= 15/2 state being the predominant component. An exception is found in the case of the 5-Dy complex. Since Dy^{3+} possesses large anisotropy in the ground state, some complexes still show some SMM behaviour. The reduced zero-field SMM behaviour of Dy complexes is a consequence of smaller energy barrier, which was facilitated by the instability of oblate-shaped Dy^{3+} in equatorial ligands. In general, such a sandwich-type ligand surrounding is more suitable for Er^{3+} instead of Dy^{3+} for a good SMM performance. The influence of a neighbouring metal on the SMM performance varies between Er and Dy complexes. Although a weak coupling between the ground states of each ion exist in both Er and Dy dimers, the exchange-bias suppressed QTM only appeared in Er dimers. In contrast, the coupling facilitates magnetic relaxation by lowering the already small first excited state energy barrier in Dy dimers.

A trinulclear ion complex was investigated for its magnetic properties. The magnetic anisotropy of the ground state is not significant. The application as a SMM is limited. The nearest neighbors exhibit antiferromagnetic coupling, with the coupling strength likely falling between the estimates obtained from DFT-BS and CASOCI methods. Magnetic measurements on a stable sample would clarify the issue.

5 Optical and Magnetic Properties of Oxides Containing Ln Elements

5.1 Introduction

5.1.1 High Entropy Oxide

The concept of high-entropy material was first presented by two research groups in producing stable multi-component alloys.[154,155] For a system with n types of distinct metal ions, the per mole ideal configurational entropy is defined as[156]

$$\Delta S_{conf} = -R \sum_{i=1}^{n} X_i \ln(X_i) \tag{81}$$

where R is the gas constant, X_i is the mole fraction of the i^{th} component. ΔS_{conf} is maximized when the n components are equiatomic. The material is defined as high-entropy when $\Delta S_{conf} > 1.5\text{R}$.[157] The Gibbs energy of the formation for mixing several components can be written as[156]

$$\Delta G_{mix} = \Delta H_{mix} - T\Delta S_{mix} \tag{82}$$

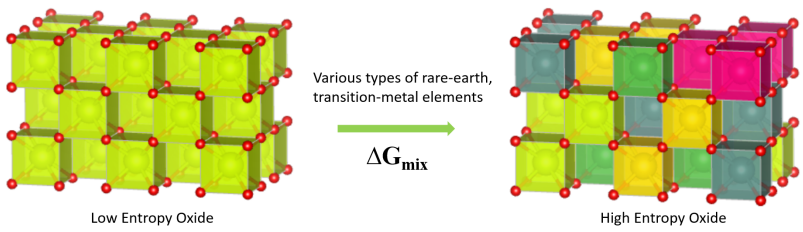

Figure 44: Conceptual illustration of high-entropy oxides. Red: oxygen; other colors: metal atoms.

It is clear that when the entropy increases, the process is energetically favoured and the formation is stabilized. Inspired by the synthesis of high-entropy alloys, high-entropy oxides (HEOs) were first introduced by Rost *et al.*[158] as "entropy-stabilized oxides". The configurational disorder facilitates the formation of multi-component single-phase oxides.[157] HEOs exhibit a high concentration of oxygen vacancies and higher oxygen mobility comparing to low and medium entropy metal oxides.[159] The structural and chemical complexity of HEOs leads to applications such as selective catalysts in CO_2 hydrogenation[160] and energy storage materials.[157] Although the complexity presents significant challenges to computational research,[160] it opens up considerable opportunities to tailor properties, such as the bandgap[161] of materials.

In order to engineer the properties of HEOs, a theoretical investigation of the structural and electronic properties of HEOs is essential and will potentially provide valuable insights to these complex systems. In this chapter, we explore the structural and electronic properties of cerium oxide, with particular emphasis on the role of oxygen vacancies. Additionally, the magnetic and optical properties of individual Ln^{3+} were investigated in cerium oxide model system.

5.1.2 Embedded Cluster Model

To study periodic system such as oxides, it is common to use Density Functional Theory (DFT)[162] with periodic boundary condition[163] for the geometry optimization and to calculate other properties. However, in the case of strongly correlated systems such as oxides containing open-shell 3d or 4f elements, the local density approximation (LDA) and generalized gradient approximation (GGA) functionals, which predict delocalized f electrons[164], fail to give reasonable descriptions of electronic structures of 4f containing oxides due to the self-interaction error.[165]

Within the framework of periodic DFT, two primary methods are employed to mitigate the self-interaction error: the introduction of the Hubbard U parameter and the utilization of hybrid functionals. Each of these approaches comes with its own set of advantages and disadvantages. The Hubbard U parameter was introduced to take the on-site Coulomb interaction into account[166] which makes the localization of 3d and 4f electrons possible.[164] Nevertheless, calculated band gaps and lattice constants were found to strongly depend on the parameter U.[167] As for the solution of employing hybrid functionals,[168] the computational cost of using them in periodic system

becomes unbearable.[167] In the majority of periodic DFT calculations, plane-wave basis sets are used.[169]

The alternative approach to calculate properties of periodic systems is to employ embedded cluster models. This strategy allows the treatment of local features with high-level quantum chemical methods within an extended, yet finite, environment to effectively mimic the periodicity of the system.[167] With embedded cluster methods, computationally more demanding methods including DFT with hybrid functionals as well as wave function methods such as second order Møller–Plesset perturbation theory (MP2) and Coupled Cluster (CC) methods can be used to calculate local features of periodic systems at a moderate cost.[167,170–173] This feature makes it possible to give insights to what is experimentally challenging to measure.[174,175] The main part of the periodic system is represented by a finite set of point charges in the experimentally determined ionic sites.[174] The finite set of point charges is generated to represent the Madelung potential.[176] Fractional charges are used to stabilize the potential and to correct the poor convergence of the Madelung series.[177]

An illustration of different regions in the embedded cluster model is shown in Figure 45. The quantum cluster is further divided into boundary region and high level region (see Figure 45). Normally, small basis sets or Effective Core Potentials (ECPs) are applied to atoms in the boundary region while larger basis sets are used in the high level region.

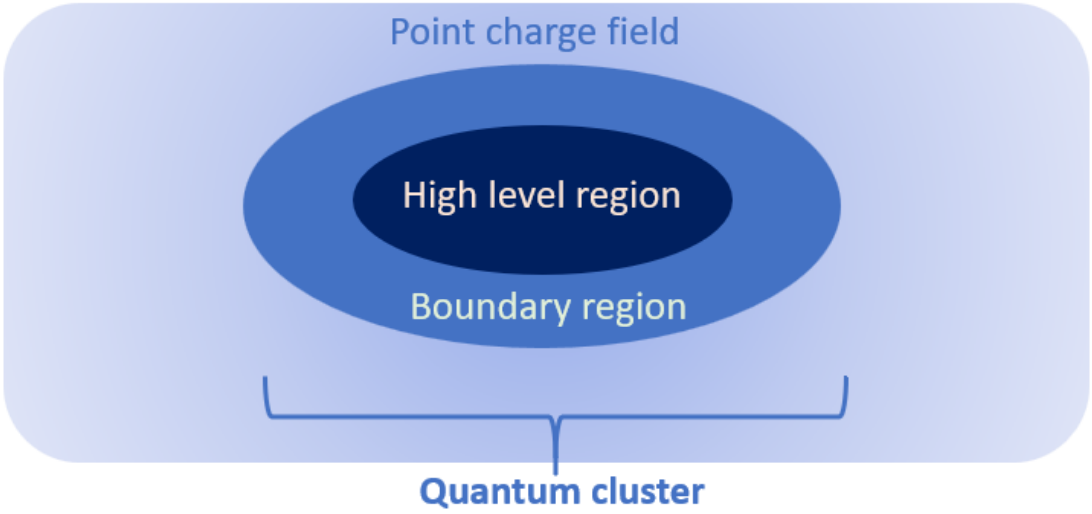

Figure 45: Illustration of the embedded cluster model.

5.2 Computational details

In this chapter, three different sizes (2-center, 4-center and 6-center) of model clusters were considered as can be seen from Figure 46. The model clusters were constructed based on the crystal structure of CeO_2. The point charge field was generated according to the lattice parameters of CeO_2 using the EVJEN program developed in Bochum. Geometry optimization and electronic structures are calculated by the computational chemistry package Turbomole.[107] The energy level with SOC included, so as spectra and magnetic properties are calculated with CASOCI program.[16]

Geometry optimizations were carried out at DFT level with the PBE0[116,117] functional and three different basis sets. Dispersion corrections were considered with Grimmes D3 correction combined with Becke-Johnson damping.[110,111] The RI approximation[112,113] with the corresponding auxiliary basis sets was applied in the cases. The basis sets used are listed below:
1. SVP: [Ce, O: def2-SVP[115]; Ti: ecp-18-mhf[178]],
2. TZVP: [Ce, O: def2-TZVP[115]; Ti: ecp-18-mhf[178]] and
3. F-CORE: [O: def2-TZVP[115] ; Ce: ECP46MVB[179]; Ti: ecp-18-mhf[178]].
F-CORE indicates that the energy-adjusted pseudopotentials[179] with 46 electrons in core is used for Ce.

The electronic structures are calculated at B3LYP[108,142,143]-D3(BJ)[110,111]/x2c-TZVPall level.[139] This strategy of employing different functionals is grounded in literature findings where the PBE0 functional is shown to deliver superior performance in terms of structural parameters, while B3LYP is noted for its better accuracy in electronic properties.[180] Molecular orbitals of clusters containing open-shell Ce^{3+} were optimized using the ROHF with Roothaan parameters for the electron configuration $[Xe]4f^1$ (Table A1). In all-electron calculations, fourth-order Douglas-Kroll[140,141] was used for the optimization of ROHF orbitals to incorporate relativistic effect. CASSCF (n/m) calculations (Bochum) were carried out based on ROHF optimized orbitals with n as the number of electrons in the active space and m as the number of active orbitals.[30]

The cluster is formed such that each Ce atom is surrounded by eight oxygen atoms, and each oxygen atom is surrounded by four metal atoms. The boundary region between the point charges and the quantum cluster is chosen to be Ti^{4+} ions, because the formal charge is also 4+ and the ionic radius is similar to that of Ce^{4+} ions.

Atoms in the boundary region are fixed during optimization. Outside the boundary lies the point charge field, which, together with the quantum cluster, achieves charge neutrality. Point charges are omitted in the figure for clarity.

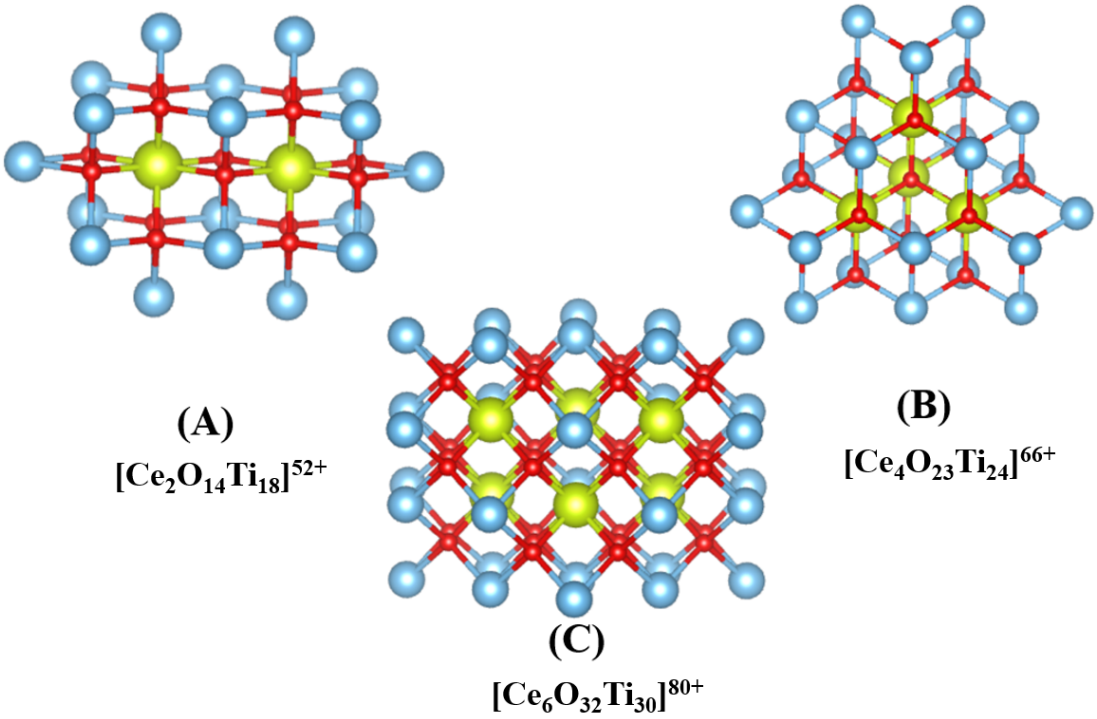

Figure 46: Illustration of model clusters for CeO_2 with various sizes. Blue: Ti; Yellow: Ce; Red:oxygen.

In this section, the chemical structures are visualized by VMD[119] and VESTA[181] and the graphs are plotted with Origin[121] and Matplotlib.[182]

5.3 Geometry Optimization

Geometry optimizations were carried out for three sizes of clusters and with different basis sets. Both defect-free model clusters and defect model clusters with one oxygen vacancy (V_O) are optimized.

5.3.1 Defect-free Model Clusters

The calculated Ce-O (with its direct neighbouring O) distance varies marginally in the range of 2.37-2.42 Å in all clusters. Optimized Ce-Ce distances are compared in Figure 47.

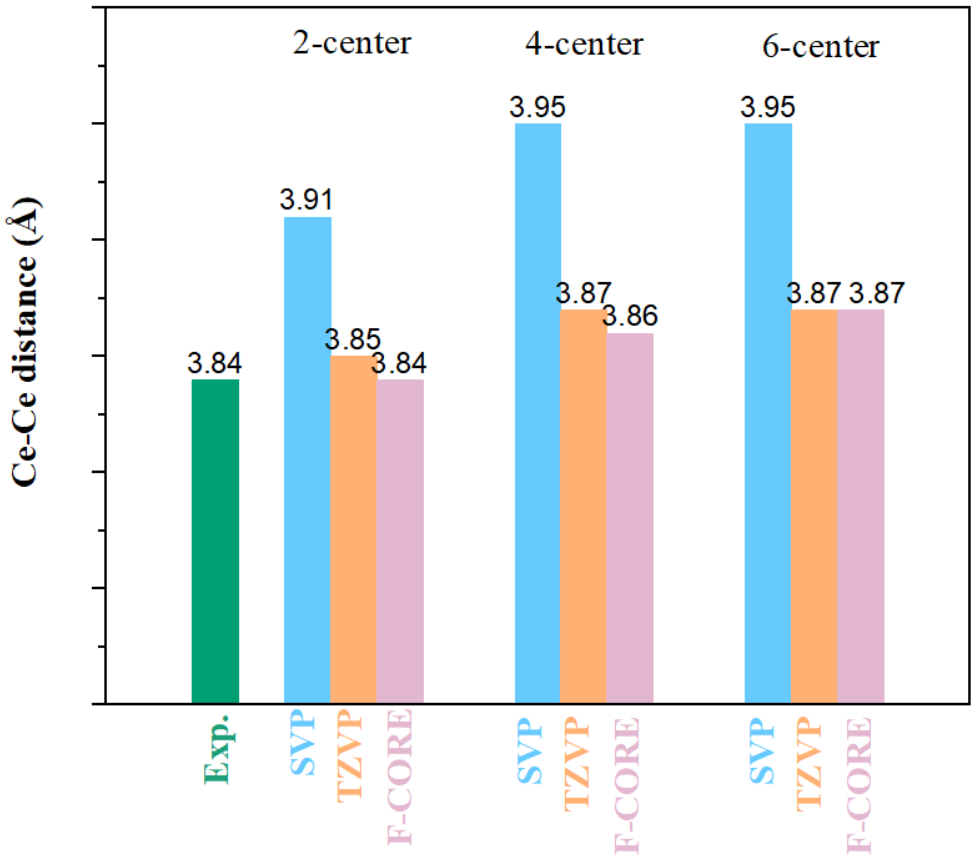

Figure 47: Calculated (average) Ce-Ce distances (in Å) determined across various cluster sizes, employing three distinct basis sets at PBE0-D3(BJ) level.

In all clusters, both TZVP and F-CORE basis sets give good agreement to the experimental value for the Ce-Ce distance while SVP overestimates the metal-metal distance. The influence of cluster size on the Ce-Ce distances is negligible. A good agreement with the experimental value is already achieved in the smaller 2-center cluster. Therefore, mainly the 2-center cluster is considered to calculate the electronic structure and other properties to reduce the computational effort.

5.3.2 Defect Model Clusters with One Oxygen Vacancy

There are two types of oxygen sites in the model clusters depending on the number of Ti and Ce in the first coordination sphere. The oxygen vacancy position is always chosen to be the site with more real ions in the surrounding of oxygen vacancy (see Figure 48, oxygen vacancy is marked as purple circle).

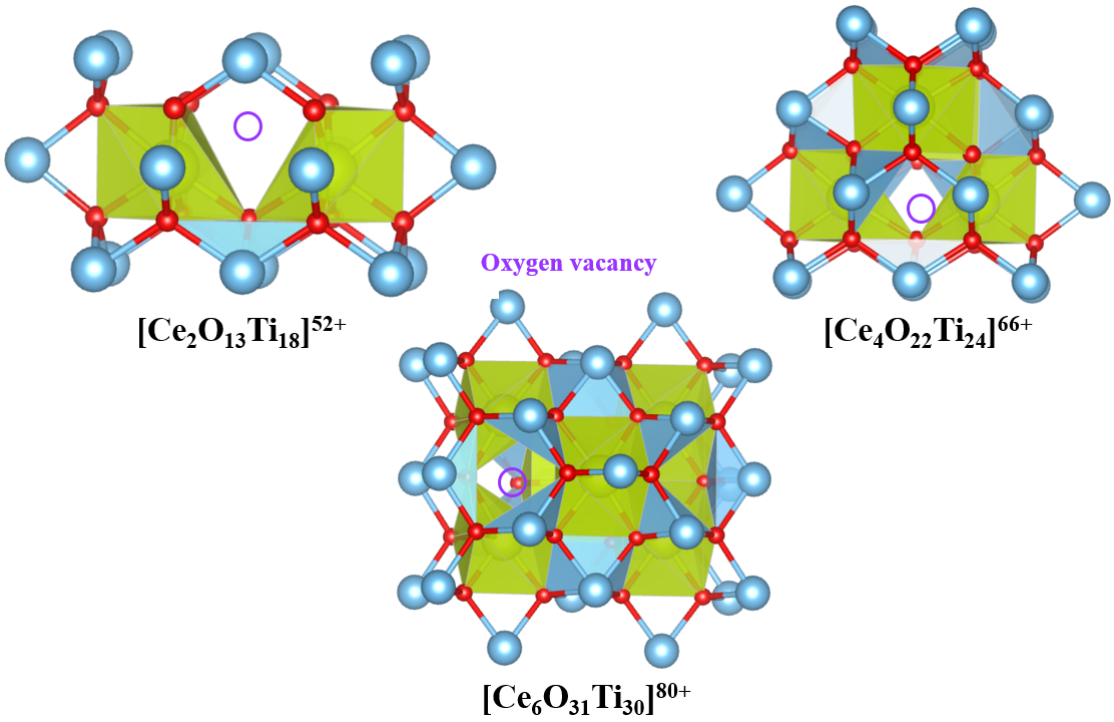

Figure 48: Illustration of oxygen vacancy positions (in purple circle) in 2-,4- and 6-center clusters. Blue: Ti; Yellow: Ce; Red:oxygen.

After the removal of O^{2-}, two electrons are left in the quantum clusters, leading to three potential electronic states for the defect clusters: closed-shell, singlet, and triplet states. Defect clusters of three possible states were all optimized and compared to the geometries of defect-free clusters. The Ce-Ce distances between Ce centers optimized in TZVP level in defect clusters are longer. When O^{2-} is removed, only the repulsive electrostatic interaction between two positively charged Ce ions remains, while the attraction of the O^{2-} is missing. Therefore, the distance increases. Exceptions appeared in the closed-shell state optimized at F-CORE level in 2 and 4-center clusters. Although F-CORE performs well in predicting the structure of perfect clusters, it is questionable whether it can properly describe the defect clusters.

There are several reasons that F-CORE can not give a good description of the

cluster structures. Firstly, all f-electrons were put into the core in F-CORE. As a result, there is no basis functions to properly describe the electronic structure change in the f-shell of Ce. Secondly, the energy-adjusted pseudopotentials[179] distinguishes between different oxidation states of the same element, consequently, can not accurately describe a process that involves the change of oxidation states. Therefore, the TZVP optimized clusters are used to study oxygen formation energies and electronic structures of the defect clusters.

	2-center-vac			4-center-vac			6-center-vac		
	closed-shell	singlet	triplet	closed-shell	singlet	triplet	closed-shell	singlet	triplet
TZVP	3.92	4.06	4.06	4.04	4.12	4.12	4.04 *	4.12*	4.12*
F-CORE	3.77	3.99	4.01	3.76	4.08	4.09	3.95	4.09	4.10

Table 20: Calculated average Ce-Ce distance (Å) in 2, 4 and 6-center defect clusters (oxygen vacancy in the middle between Ce atoms) in different electronic states at PBE0-D3(BJ) level. *: the Ce atoms surrounding the oxygen vacancy were considered to calculate the average Ce-Ce distances.

5.3.3 Defect Model Clusters with Diamagnetic Substitution

DFT as a single reference method poorly describes the electronic states of Ln^{3+} with more than one electron in the f-shell. However, it should be noted that multi-reference methods are primarily employed for electronic structure analysises, while for the geometry optimization DFT is the method of choice. Therefore, diamagnetic substitution of the metal centers was used in order to optimize the geometries at DFT level without involving multi-reference problems. The influence of different crystal radii and charges of substitution ions on the local geometry was investigated.

Ce^{4+}/La^{3+}/Y^{3+} were chosen as diamagnetic substitutions for their various charges and ionic radii. The optimized Ln-Ln distances are given in Figure 49. The 8-coordinate ionic radii are 0.97, 1.16 and 1.02 Å for Ce^{4+}, La^{3+} and Y^{3+}.[183] Calculated Ln-Ln distances exhibit minor variations, ranging from 3.98 Å for Y^{3+}_Y^{3+} as the shortest distance to 4.17 Å for the Ce^{4+}_Ce^{4+} cluster. Due to the stronger electrostatic repulsion between two Ce^{4+} ions than between 3+ ions, the metal-metal distance is longer for the two 4+ ions. In the case of Y^{3+} and La^{3+} that share the same charge, the

larger ionic radius of La^{3+} results in a slight expansion of the metal-metal distance. The metal-oxygen distances reflect the local distortion of the first coordination sphere. For the three clusters optimized (La^{3+}_La^{3+}, Y^{3+}_Y^{3+}, La^{3+}_Y^{3+} vacancy clusters), the La-O and Y-O distances remain almost unchanged in all clusters (see Figure A6 in Appendix C).

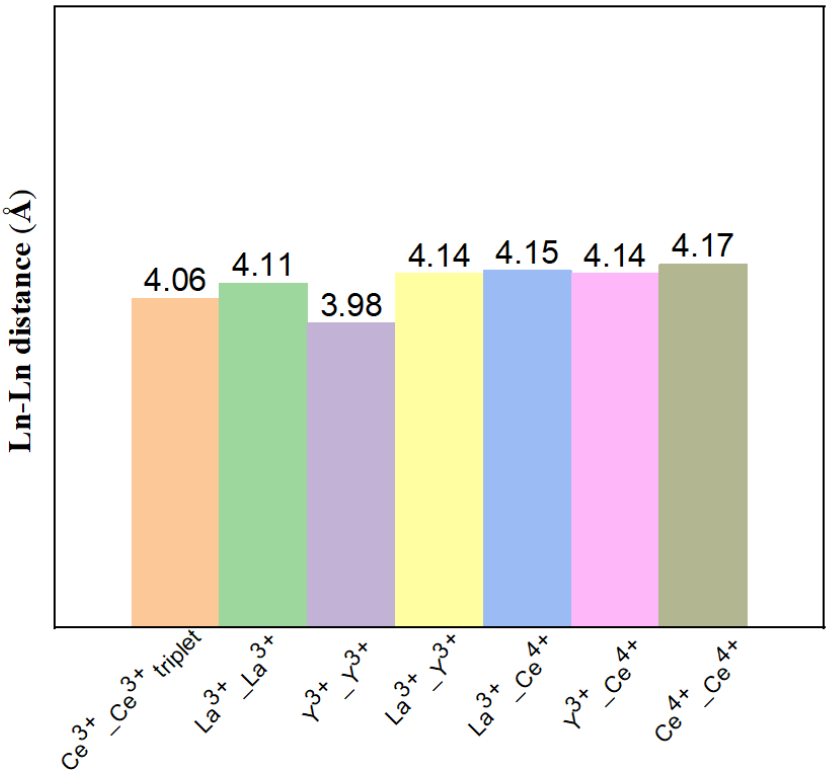

Figure 49: Ln-Ln distance (Å) in optimized 2-center vacancy clusters with different diamagnetic substitutions at PBE0-D3(BJ)/TZVP level.

5.4 Electronic Structures

5.4.1 Oxygen Vacancy Formation

The estimated oxygen vacancy formation energy from experiments is 4.2±0.3 eV.[184,185] Both periodic DFT and the embedded cluster model were applied to calculate the oxygen vacancy formation energy in CeO_2, as summarized in a comprehensive review.[167] Periodic DFT with hybrid functional HSE[186,187] and PBE+U(4.5) underestimates the formation energy by 0.5 eV and 1.4 eV.[167] The oxygen formation energy calculated by Burow *et al.*[188] in bulk Ce_4O_{18} quantum clusters at PBE0/DZVP-46 level is 3.00

eV to form a triplet state.

The oxygen formation energies (ΔE_f) to form closed-shell, singlet and triplet states (Table 21) were calculated in various clusters using the embedded cluster method according to eq. 83. With the increase of the size of the quantum cluster, the oxygen vacancy formation energy for the triplet structure decreased from 2.63 eV in the 2-center cluster to 1.18 eV in the 4-center and to 0.72 eV in the 6-center cluster. The formation energy of oxygen vacancy is systematically underestimated from the by model clusters. Importantly, in all clusters it is energetically more favoured to form open-shell singlet/triplet states. In conclusion, the calculated oxygen vacancy formation energies of different electronic states support with the removal of oxygen, the two electrons left in the cluster should form an open-shell state.

$$\Delta E_f = E(\mathrm{Ce_mO_{n\text{-}1}}) + E(\frac{1}{2}\mathrm{O_2}) - E(\mathrm{Ce_mO_n}) \tag{83}$$

	Closed-shell	Singlet	Triplet
2-center	6.16	2.63	2.62
4-center	3.60	1.18	1.19
6-center	3.20	0.72	0.72

Table 21: Calculated oxygen vacancy formation energy (ΔE_f) in eV at B3LYP-DJ(B3)/x2c-TZVPall level based on PBE0-D3(BJ)/TZVP optimized structure.

5.4.2 Spin Density

The spin densities of singlet and triplet states of various vacancy clusters are plotted in Figure 4. In both singlet and triplet states, unpaired electrons tend to localize on the two Ce atoms neighbouring the oxygen vacancy.

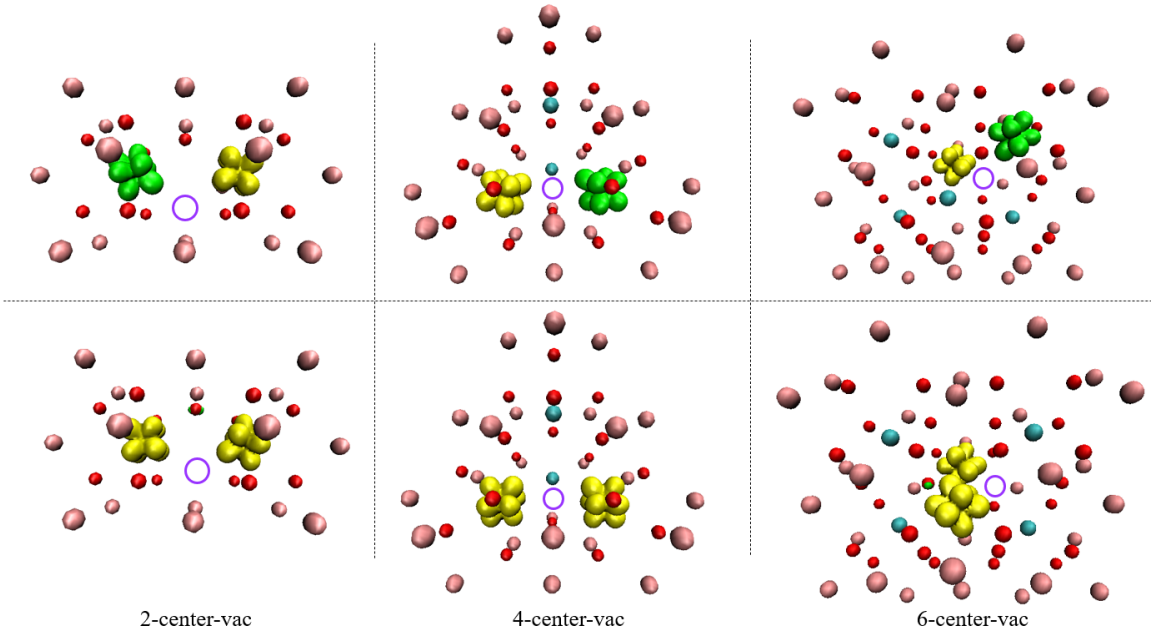

Figure 50: Plotted spin density (isovalue=±0.005 a.u.) of the singlet (above) and triplet (below) states of the 2, 4 and 6-center vacancy clusters at B3LYP-D3(BJ)/x2c-TZVPall level. The oxygen vacancy position is marked in puple circle. Red: O; blue: Ce; Pink: Ti.

With the oxygen removal, no basis functions were located at the vacancy position and consequently the electron density at this place is zero. The spin density of the 2-center-vac cluster with a dummy atom and basis set at the vacancy site is shown in Figure 51. In this case, the existence of the basis set in the oxygen vacancy site did not change that the electrons remain localized on the metal centers. Therefore, the deduction can be made that the oxidation state of the neighbouring Ce is reduced to 3+ due to the formation of the oxygen vacancy.

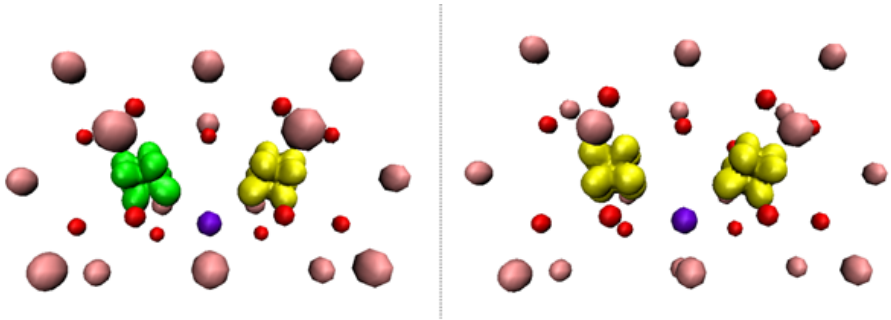

Figure 51: Plotted spin density (isovalue=±0.005 a.u.) of the singlet (left) and triplet (right) of 2-center-vac clusters with dummy oxygen atom in violet (B3LYP-D3(BJ)/x2c-TZVPall level). Red: O; blue: Ce; Pink: Ti.

The distribution of the excess electrons in the defect cerium oxide with oxygen vacancies has been debated by many groups using different methods.[189] Ganduglia-Pirovano *et al.*[190] stated the next-nearest neighbour (NNN) Ce to the oxygen vacancy is the most energetically favoured sites for the excess electrons. This result agrees with earlier research using DFT+U methods[191–193] and embedded cluster model with the PBE0 functional.[188] However, Han *et al.*[194,195] reported the excess electrons are localized on the nearest neighbour (NN) which agrees with the results from some other research groups.[196–198] Both Han *et al.* and Ganduglia-Pirovano *et al.* calculated the one oxygen vacancy formation energy in a (2×2×2) supercell using the HSE06[186,187,199] hybrid functional. The results from Ganduglia-Pirovano *el al.*[190] demonstrated that the configuration featuring both excess electrons localized at the NNN location is 0.05 eV (4.82 kJ/mol) lower in oxygen vacancy formation energy compared to that featuring Ce^{3+} at the NN position. Contrarily, the oxygen formation energy is 0.017 eV (1.6 kJ/mol) lower for the configuration with electrons at the NN positions was calculated by Han *et al.*.[195] According to Han *et al.*,[195] the discrepancy can be attributed to the different lattice relaxation schemes. A full relaxation of the shape, volume and atomic positions was applied by Han *et al.*[195] while the HSE06 optimized lattice parameter 10.7875 Å was also applied to reduced cerium oxide and the atomic positions were relaxed from Ganduglia-Pirovano *el al.*.[190]

Our calculations show that within a 6-center-vac cluster featuring both NN and NNN positions, the two excess electrons are localized at the NN positions in the absence of further constraints on geometry relaxation. Further investigations were carried out applying a two-step approach[200] for the geometry optimization. First, a 6-center-vac cluster $[La_2Ce_4O_{32}Ti_{30}]^{80+}$ with two La^{3+} ions at the NNN positions was optimized at PBE0-D3(BJ)/F-CORE level. Second, with this structure as a starting geometry, a 6-center-vac cluster containing six Ce atoms $[Ce_6O_{32}Ti_{30}]^{80+}$ is fully relaxed at PBE0-D3(J)/TZVP level for a triplet state. This two-step approach assumes the two excess electrons to be at the NNN positions. A minor increase of the Ce-Ce distance (Ce at NN positions) optimized by the two-step approach compared to the direct relaxation was observed (Table 22). With the structure optimized to facilitate the Ce^{3+} at the NNN positions, the spin density shows that the unpaired electrons are localized at the NNN positions. However, the electronic energy (calculated at B3LYP-D3(BJ)/x2c-ZTVPall level) is 7.5 kJ/mol higher comparing to the the electronic energy from directly relaxed structure. The absorption spectra of both Ce^{3+} at NN/NNN positions were also calculated, details will be given in section 5.5.2.

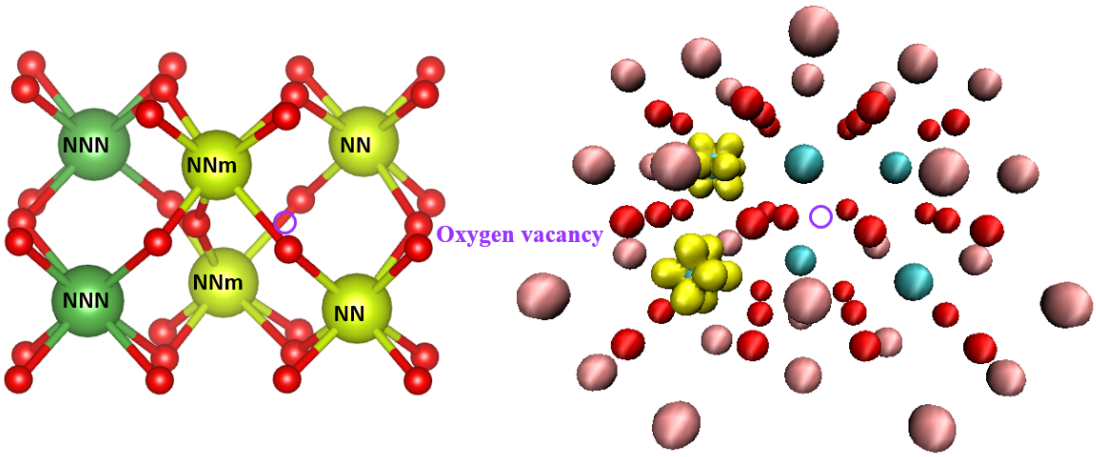

Figure 52: Left: Illustration of NN (yellow) and NNN (green) positions in a 6-center-vac cluster. NNm: nearest neighbour middle. Right: Plotted spin density (isovalue=±0.005 a.u.) of the triplet $[Ce_6O_{32}Ti_{30}]^{80+}$ (optimized with the two-step approach). Red: O; blue: Ce; Pink: Ti; Purple circle: oxygen vacancy position.

	$[La_2Ce_4O_{32}Ti_{30}]^{80+}$	$[Ce_6O_{32}Ti_{30}]^{80+\ *}$	$[Ce_6O_{32}Ti_{30}]^{80+}$
NN-NN	4.19	4.17	4.13
NN-NNm	4.16	4.15	4.12
NN-NNm	4.16	4.15	4.05
NN-NNm	4.16	4.14	4.12
NN-NNm	4.16	4.14	4.19
NNm-NNm	4.24	4.22	4.14
NNN-NNN	3.93	3.94	3.91
NNN-NNm	3.93	3.94	3.87
NNN-NNm	3.93	3.94	3.88
NNN-NNm	3.93	3.94	3.89
NNN-NNm	3.93	3.94	3.88
Relative energy$^!$	6.79 kJ/mol	7.5 kJ/mol	0

Table 22: The optimized Ln-Ln distances (Å) in the $[La_2La_4O_{32}Ti_{30}]^{80+}$ cluster (closed-shell), $[Ce_6O_{32}Ti_{30}]^{80+\ *}$ cluster (triplet) and $[Ce_6O_{32}Ti_{30}]^{80+}$ (triplet) and their relative energies to $[Ce_6O_{32}Ti_{30}]^{80+}$. *: the geometry is optimized by the two-step approach mentioned in the text. Relative energy$^!$: the reference is the electronic energy of $[Ce_6O_{32}Ti_{30}]^{80+}$.

5.4.3 Energy Levels

The electron configuration of Ce^{4+} is $[Xe]f^0$ which is transformed to $[Xe]4f^1$ for Ce^{3+} as a consequence of the introduction of oxygen vacancies. In order to capture the multi-reference characteristics of open-shell Ln^{3+} ions, CASSCF calculations were conducted for the vacancy clusters. The CASSCF calculation was performed on the vacancy clusters with two Ce^{3+} (CAS 2/14). CASOCI calculation was performed based on CASSCF optimized orbitals to take SOC into account. The calculated energy levels are shown in Figure 53.

For one individual center, Ce^{3+} has a $[Xe]4f^1$ configuration with spin s=1/2 and angular momentum l=3. SOC lifts the degeneracy in the ground state ^2F to $^2F_{5/2}$ and $^2F_{7/2}$ states, with $^2F_{5/2}$ lower in energy. SOC results in energy splitting of 2253 cm^{-1} in the free ion.[126] The energies of individual centers are shown by yellow and green lines. Ce^{3+} is a Kramer's ion. Each line corresponds to a two-fold degenerate state in energy level graph of the individual centers. As a result of the presence of the crystal field, $^2F_{5/2}$ and $^2F_{7/2}$ states are further split into three and four substates, respectively.

The coupling between two centers can be probed by comparing the energy of the two-center calculation and the individual center calculations. The coupling of the ground states is shown more in detail in the blue box in Figure 53. The largest energy splitting caused by the coupling is less than 1 cm^{-1} at the ground state. It is expected from CASOCI to underestimate the coupling energy because the charge transfer states energies are overestimated by CASSCF wave functions.[65] However, the coupling between the two neighbouring metal ions is weak. The negligible coupling between the two nearest spin centers indicates the magnetic susceptibility of the 2-center-vac clusters can be reduced to calculate the properties at individual centers (with diamagnetic substitution of the other spin centers).

To assess the impact of different ionic radii and charges of neighbouring metal center on the energy of the Ce^{3+}, Y^{3+}, La^{3+} and Ce^{4+} were used as diamagnetic substitutes. The calculated energy levels of the Ce^{3+} in vacancy clusters with different diamagnetic substitutions are compared in Figure 54. The energy levels were calculated based on CASSCF and ROHF optimized orbitals. The difference between the energies calculated by CASSCF and ROHF orbitals is negligible in all three types of vacancy clusters.

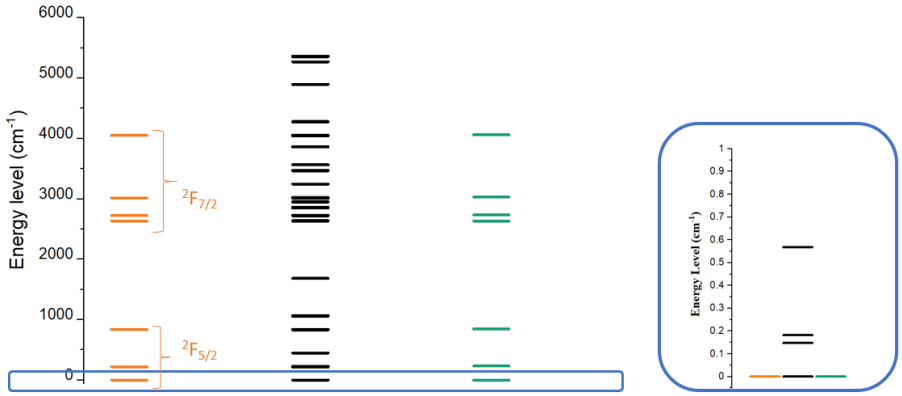

Figure 53: Calculated energy levels (cm^{-1}) of the 2-center-vac cluster. Yellow and green lines are energies of individual centers, black lines are energies calculated with two open-shell centers.

ROHF is the preferred method to obtain open-shell orbitals due to the advantage of its reduced computational cost. The calculation also reveals that the different charge 3+ ions (Y^{3+} and La^{3+}) as diamagnetic substitutions has no impact on the computed energy levels. A slight deviation was observed between the energy calculated with Ce^{4+} as a substitution, however, the deviation remains insignificant.

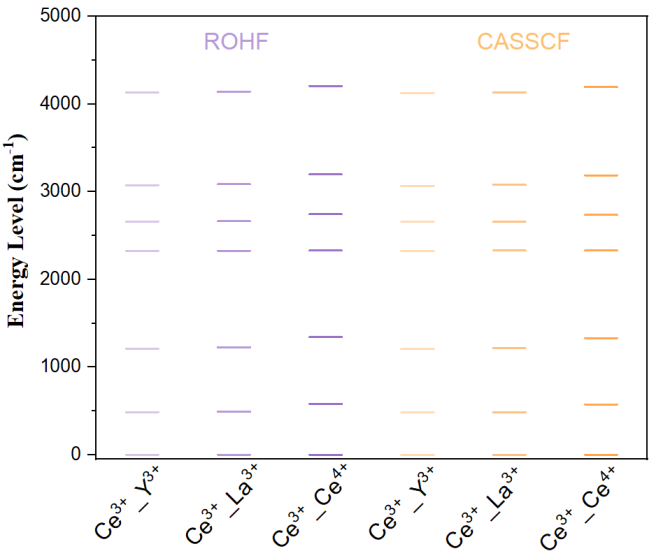

Figure 54: Calculated energy levels (cm^{-1}) of Ce^{3+} in 2-center-vac clusters with various diamagnetic substitutions on the neighbouring center. Purple: calculations based on ROHF optimized orbitals. Yellow: calculations based on CASSCF optimized orbitals.

5.5 Optical Properties

For the free ion, the $^2F_{5/2} \rightarrow {}^2F_{7/2}$ transition is Laporte forbidden[89] in gas phase because of its high symmetry. However, oxygen vacancies in the reduced CeO_2 consequently lead to the reduction of symmetry in the first coordination sphere for the Ce centers. The $^2F_{5/2} \rightarrow {}^2F_{7/2}$ transition in reduced CeO_2 can gain intensities. These transitions of Ce^{3+} are probed in experiments in the infrared region.

Spectra of Ce^{3+} in lower symmetry sites were reported previously. Weber[201] reported the infrared spectrum of Ce^{3+} doped in $YAlO_3$ (C_1 symmetry) , with four energy levels of 2085, 2485, 2695 and 3250 cm^{-1} identified as from the ground state to the $^2F_{7/2}$ state. Buchanan *el al.*[202] reported four absorption lines at the 2160, 2240, 2635 and 2845 cm^{-1} of Ce^{3+} in LaF_3 (D_{3h} symmetry at La site) that are identified as transitions from the ground state to the four Kramers levels in the $^2F_{7/2}$ state. Afrin *et al.*[203] demonstrated the non-forbidden nature of the $^2F_{5/2} \rightarrow {}^2F_{7/2}$ transition of Ce^{3+} in reduced CeO_2 (C_{3v} site) using group theory and utilized the well-defined 2150 cm^{-1} band to probe the vacancy densities *in situ* and quantitively by monitoring H_2-D_2 exchange and tert-butanal dehydration.

5.5.1 Spectra of Testing Clusters

The absorption spectra of Ce^{3+} in various crystal fields in model clusters were calculated and compared to the experimental values.

Spectra of model clusters $[CeF_8]^{5-}$ and $[CeF_9]^{6-}$ where Ce^{3+} is in $YAlO_3$ and LaF_3 crystal structures with only the first coordination sphere are shown in Figure 55. In $YAlO_3$ crystal field, only the transitions between the ground KD to the four KDs of $^2F_{7/2}$ state are considered. There are four peaks at 2360, 2600, 3010 and 3390 cm^{-1} (black curve). For the spectrum of model clusters based on the La site in LaF_3 crystal field, transitions from the ground state to $^2F_{7/2}$ are found at 2350, 2550, 2910 and 2970 cm^{-1}.

Comparing to the experimental values from Weber[201] and Buchanan *el al.*[202] (see Figure 55 blue lines), our calculated spectra show a blue shift of 100 to 300 cm^{-1}. However, the model clusters consider only the first coordination sphere without extra point charges to reproduce the periodicity of the crystal.

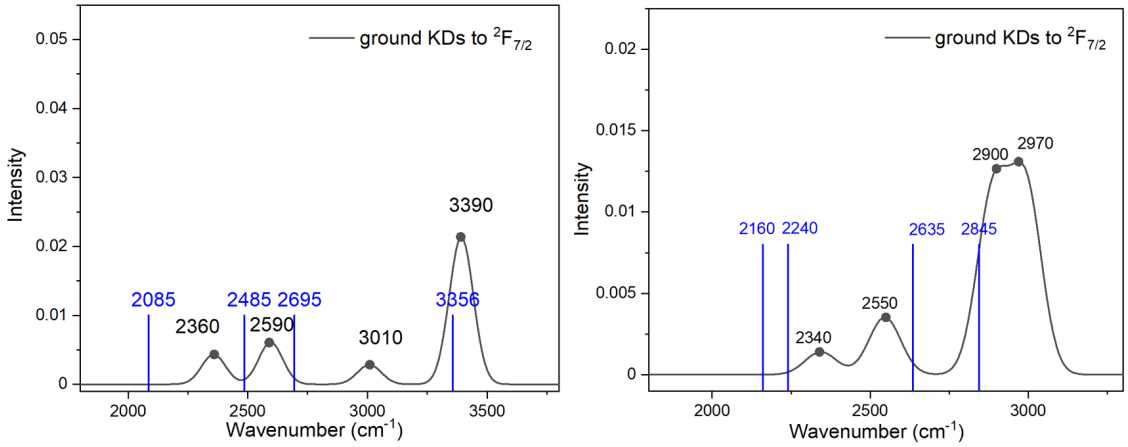

Figure 55: Calculated IR spectra of model clusters $[CeF_8]^{5-}$ and $[CeF_9]^{6-}$ in $YAlO_3$ (left) and LaF_3 (right) crystal field. Black curve: only transitions from ground the KDs to $^2F_{7/2}$ are included; Blue lines: experimental results from the references.[201,202]

5.5.2 Spectra of Cerium Oxide Defect Clusters

Three distinct model clusters were employed to capture the local environments of Ce^{3+} in perfect CeO_2 (O_h symmetry in Figure 56, O_h), in reduced CeO_2 without a local structure relaxation (C_{3v} symmetry in Figure 56, C_{3v}) and with relaxation (C_1 symmetry in Figure 56, OPT). The structures considered to calculate the absorption spectra were obtained by optimizing the triplet structures of defect clusters at PBE0-D3(BJ)/TZVP level. The cluster size varies from containing one, two, four and six Ce centers. Upon the introduction of an oxygen vacancy, the initial O_h symmetry surrounding (Figure 56, O_h) in the perfect CeO_2 was reduced to C_{3v} (Figure 56, C_{3v}). After geometry optimization of the vacancy clusters, the symmetry is further reduced due to the unequal bond length and angles (Figure 56, OPT). In 2-center and 4-center clusters, a second Ce should be reduced to 3+ with the creation of the oxygen vacancy, thus one other Ce center was substituted by Y^{3+} in both clusters. The calculated energy levels of Ce^{3+} in O_h, C_{3V} and OPT sites with different cluster sizes are shown in Figure 57. The spectra in the range of 1500-4500 cm^{-1} are shown in Figure 58.

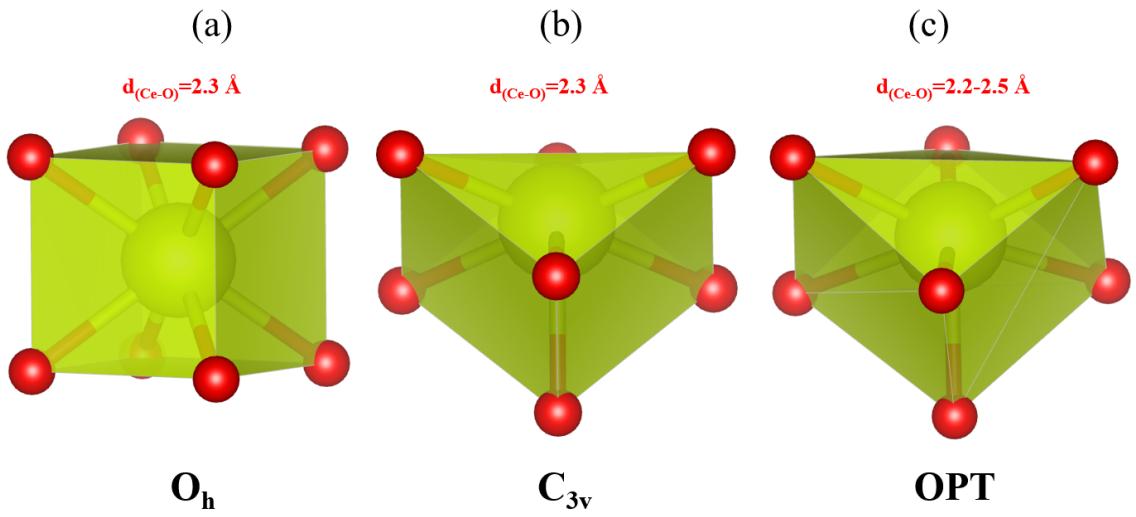

Figure 56: The crystal field of Ce^{3+} in perfect CeO_2 (O_h symmetry at the metal site, corresponds to O_h), reduced CeO_2 (C_{3v} symmetry at the metal site, corresponds to C_{3v}) and optimized reduced CeO_2 (C_1 symmetry at the metal site, corresponds to OPT) model clusters.

With SOC, the ground ^2F state is split into the $^2F_{5/2}$ and $^2F_{7/2}$ states with a gap of 2253 cm^{-1} in the free ion.[126] When the crystal field is considered, the two states will be further split into several microstates. The calculations reveal the presence of three KDs corresponding to the $^2F_{5/2}$ state and four KDs corresponding to the $^2F_{7/2}$ state. In the case of Ce^{3+} in the C_{3v} site, the energies of the KDs are notably higher that those calculated for Ce^{3+} in the other two sites. In addition, the transition from the first KD to the fourth KD is 4208, 2686 and 2556 cm^{-1} within 1-center, 2-center and 4-center-vac clusters of Ce^{3+} at the C_{3v} site, respectively. This transition from $^2F_{5/2}$ to $^2F_{7/2}$ is expected to be around 2150 cm^{-1} from experiments. The unrelaxed C_{3v} model overestimates the energies expected for a Ce^{3+} in a symmetry reduced crystal field surrounding. A local geometry optimization is necessary to obtain a good description for the zero-field splitting of Ce^{3+}.

The spectra of Ce^{3+} at O_h and optimized crystal field (OPT) are calculated and compared in Figure 58. The calculated spectra show that the transitions are not allowed when Ce^{3+} is at O_h symmetry sites (Figure 58, black curve). The peak within the infrared range is found at around 2360 cm^{-1} in the OPT model cluster regardless of the cluster size. In comparison to the experimental value,[203] the transition exhibits a blue shift of approximately 200 cm^{-1}. Another transition with high intensity is found in the range of 3600-4200 cm^{-1}. However, the energy lies beyond the detected range

in experimental observations. Up to this point, our calculation using the embedded cluster model can well describe Ce^{3+} spectra in an oxygen defect crystal field. The analysis shows that the transition becomes significant only when the local symmetry around the metal center is reduced.

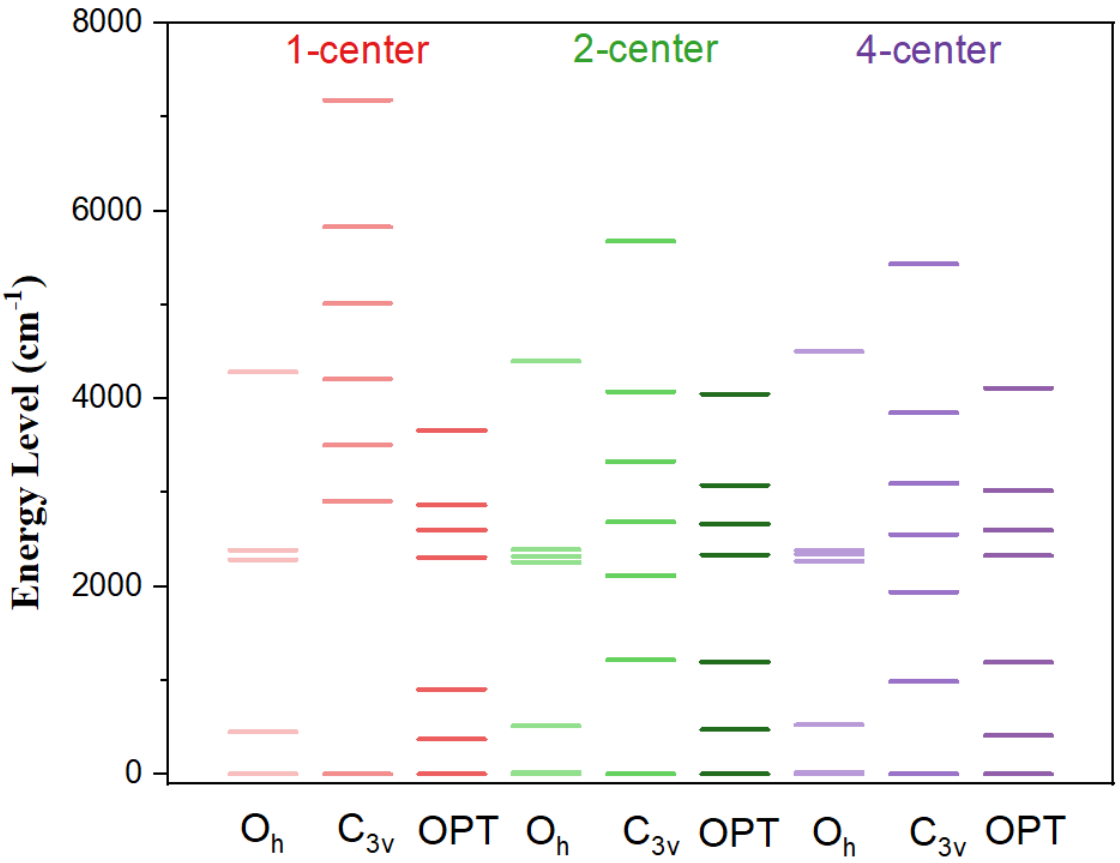

Figure 57: Calculated energy levels of the ^{2}F state of Ce^{3+} in various clusters. The lowest lying lines of Ce^{3+} in O_h symmetry are four-fold degenerate. The rest of the lines are two-fold degenerate (KDs).

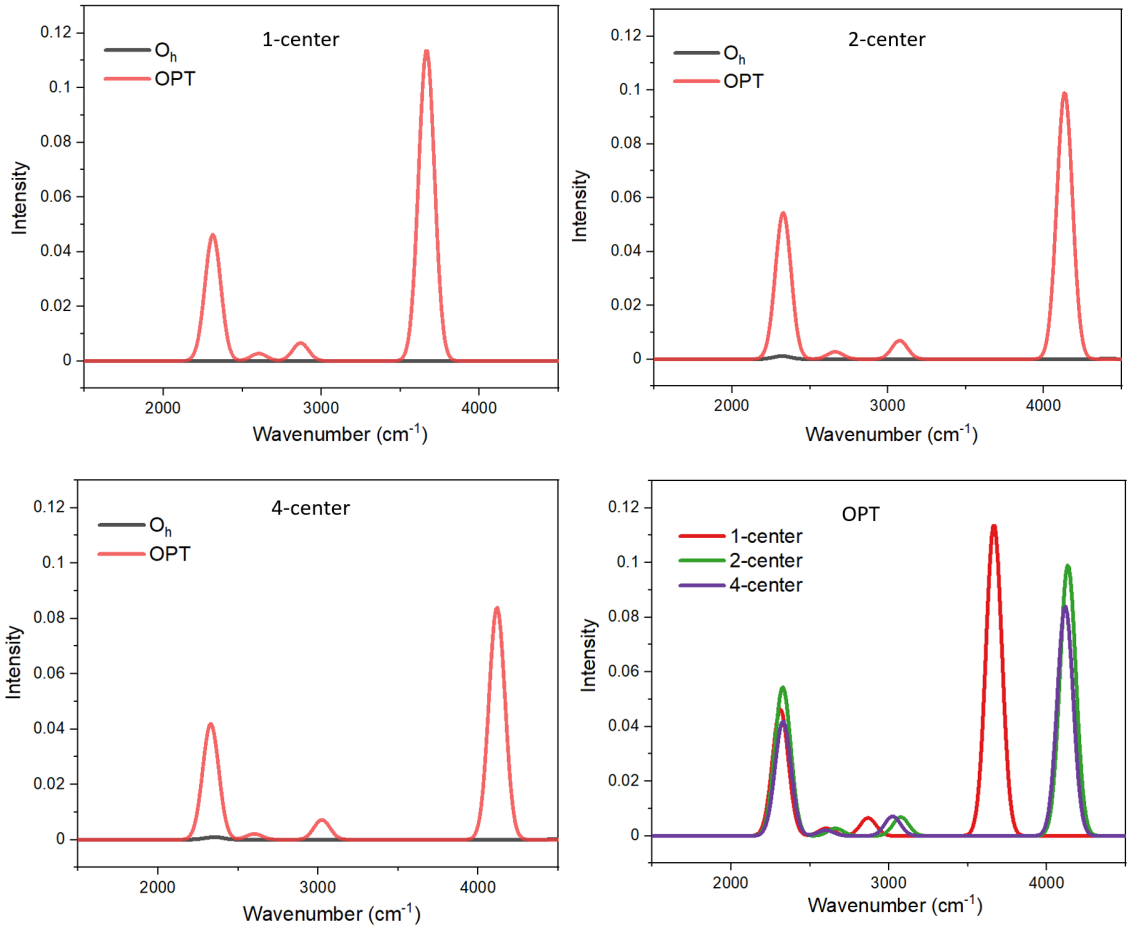

Figure 58: The calculated absorption spectra of 1-center, 2-center and 4-center clusters (defect-free and with one oxygen vacancy) with Ce^{3+} in O_h symmetry and in optimized crystal fields with oxygen vacancy.

The distribution of the two excess electrons when a oxygen vacancy is introduced was discussed in section 5.4.2. It is possible for the Ce^{3+} to be located at both NN or NNN positions. However, the NN position is energetically favoured by 7.5 kJ/mol. The absorption spectrum of Ce^{3+} at NNN position shows no absorption bands in the 2000-3000 cm^{-1} range. Contrarily, the spectrum of Ce^{3+} at the NN position shows the signature absorption band at around 2300 cm^{-1}. In a model cluster based on the bulk structure, both NN and NNN positions are possible for the excess electrons to be localized at. However, only the NN position Ce^{3+} gives optical signals in the expected range.

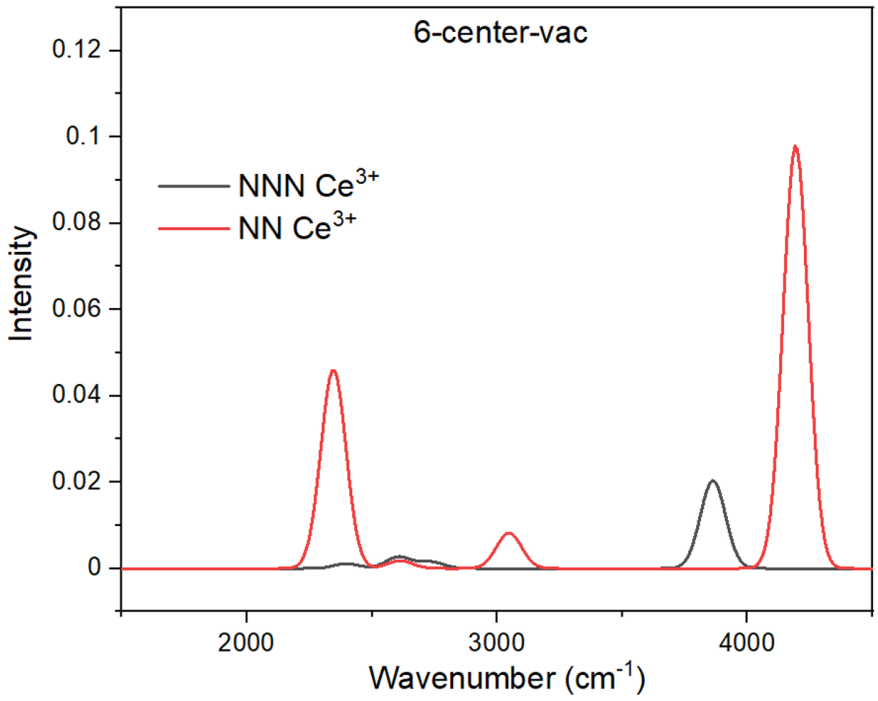

Figure 59: The calculated absorption spectra of Ce^{3+} at NN/NNN positions in the 6-center-vac model cluster.

5.6 Magnetic Properties of Cerium Oxide Model Cluster

Magnetism also emerges as a consequence of the transformation of diamagnetic Ce^{4+} $[Xe]4f^0$ to Ce^{3+} with $[Xe]4f^1$ configuration. As a result of the insignificant coupling between neighbouring metal centers shown in section 5.4.3, magnetic properties were calculated for individual Ce^{3+} in vacancy clusters.

The temperature dependent molar magnetic susceptibility $\chi_M T$ was calculated for the ^{2}F state. Figure 60 shows the comparison of the $\chi_M T$ calculated in 2-center-vac clusters with different ions. $\chi_M T$ of the vacancy cluster containing two open-shell Ce^{3+} is calculated directly considering both ions. For vacancy clusters containing only one Ce^{3+}, the total $\chi_M T$ is computed with only one open-shell Ce^{3+} multiplying by two. There is a small deviation between $\chi_M T$ calculated based on the orbitals optimized for the two-open-shell-center cluster and the one-open-shell center clusters. The negligible deviation in $\chi_M T$ indicates the total $\chi_M T$ of the clusters can be calculated as a linear combination of $\chi_M T$ from individual open-shell centers.

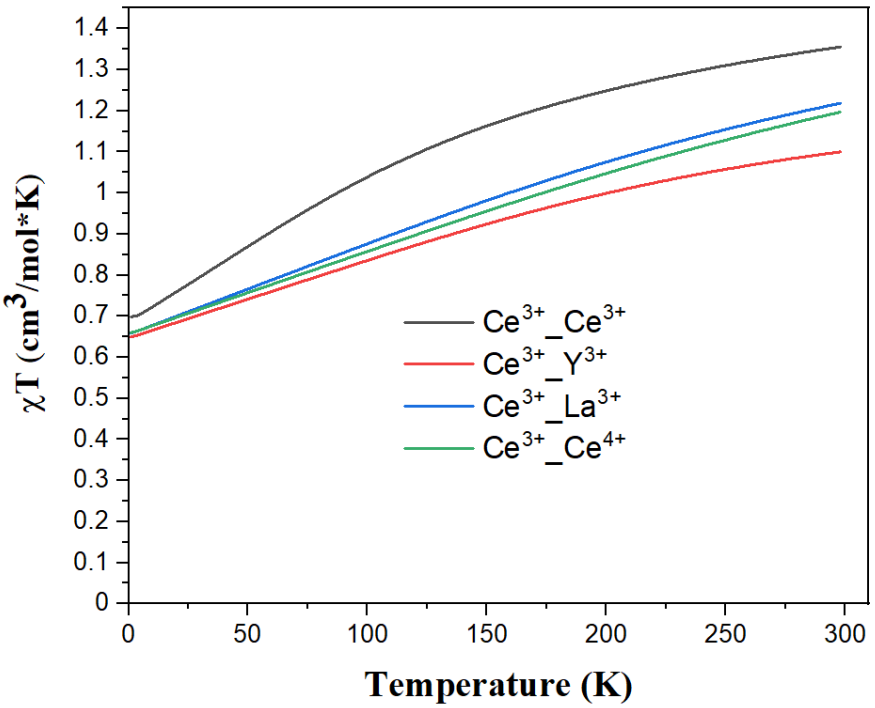

Figure 60: Calculated $\chi_M T$-T of two-open-shell-center vacancy cluster (Ce^{3+}_Ce^{3+} vacancy) and one-open-shell-center vacancy clusters mulriplied by two(Ce^{3+}_Y^{3+} and Y^{3+}_Ce^{3+} vacancy).

5.7 Optical Properties of Model Clusters containing other Ln

Earlier calculations of Ce^{3+} 4f-4f transition in vacancy clusters indicated that it is adequate to compute the absorption spectra of Ln^{3+}centers within a 2-center-vac cluster and comparable to the experimental spectra. In this session, the spectra of other Ln^{3+} in a 2-center-vac model cluster are calculated with the other center substituted by La^{3+}.

The energy levels of 4f-4f transitions are calculated based on ROHF optimized orbitals and SOC is then included with CASOCI. Nevertheless, only static correlation is incorporated while dynamic correlation is left unaccounted in this approach. It is well-known that the lack of dynamic correlation causes a drastic overestimation of excitation energies. To include dynamic correlation, methods such as the second order multi-configurational perturbation theory (CASPT2)[204,205] are used, in which multi-reference wave functions are used as reference for a second order perturbation theory calculation. However, these methods are computationally costly. The f-orbitals are mainly localized and f electrons are shielded by closed-shell 5s and 5p electrons, as a result, the ligand field splitting plays a minor role in the energy scheme. Therefore, in order to obtain reasonable excitation energies without a great amount of computational cost, the energies were calculated with CASOCI but shifted according to the atomic absorption spectra from the NIST[126] database.

The energy levels calculated for Ln^{3+} (Ln=Pr, Nd, Pm, Sm, Eu, Gd, Tb, Dy, Ho, Er, Tm, Yb) free ion and Ln^{3+} (Ln=Pr, Nd, Pm, Sm, Eu, Gd, Tb, Dy, Ho, Er, Tm, Yb) in La^{3+}_La^{3+} vacancy cluster crystal field together with the absorption spectra are given in Figure A7 to A17. Only 4f-4f transitions are considered and the transitions from the ground state to excited states are taken into account in the absorption spectra.

In the calculated spectra, precise peak assignments are possible due to the explicit consideration of the surrounding crystal field. For instance, in the spectrum of Gd^{3+} in the vacancy cluster in Figure 61, three peaks are found corresponding to the transitions of the $^8S_{7/2}$ ground state to $^6P_{7/2,5/2,3/2}$ states.

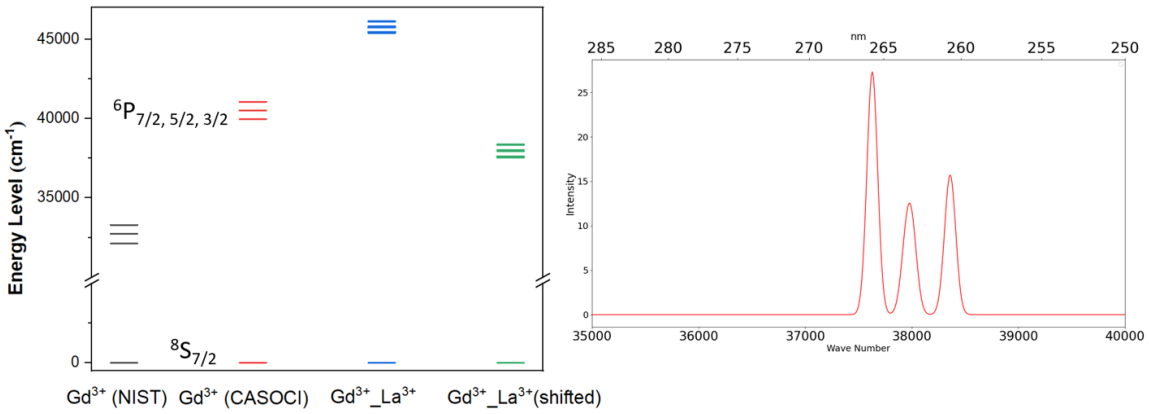

Figure 61: Calculated energy levels and the absorption spectrum of Gd^{3+} in the crystal field of the La^{3+}_La^{3+} vacancy cluster.

However, these calculated spectra provide only preliminary information about the possible observable optical signal due to 4f-4f transitions in Ln^{3+} containing HEOs. The limitations include, the lack of dynamical correlation of the method which leads to the overestimation of excitation energies, especially at higher energy levels, and the omission of 4f-5d transitions. Additionally, energy transfer in a complex system with the presence of many Ln^{3+} open-shell ions[206] were not taken into account. It has been shown that energy transfer can significantly affect the optical properties of HEOs[207]. To fully understand the optical properties of HEOs, further research is required, which will necessitate detailed knowledge of their specific compositions and consideration of the aforementioned factors.

5.8 Magnetic Properties of Model Clusters Containing Other Ln

Due to the restricted interaction between metal centers, the energy can be calculated separately for individual centers and overall magnetic susceptibility of the model clusters can be approximated as the sum of the individual centers. The magnetic susceptibility for Ln^{3+} based on optimized La^{3+}_La^{3+} vacancy clusters. In the vacancy cluster, one of the metal center is substituted by an open-shell Ln^{3+} ion, the other one by La^{3+} or Ce^{4+} ions. In Figure 62, the $\chi_M T$ of all the Ln^{3+} ions calculated in the optimized La^{3+}_La^{3+} vacancy structure is shown. Here, the magnetic susceptibilities are invariant for the same Ln^{3+} with different neighbouring charge. Previous investigations already indicated that various diamagnetic substitutions have minimal

impact on the crystal field splitting. The negligible effect on magnetic susceptibility was shown in this section.

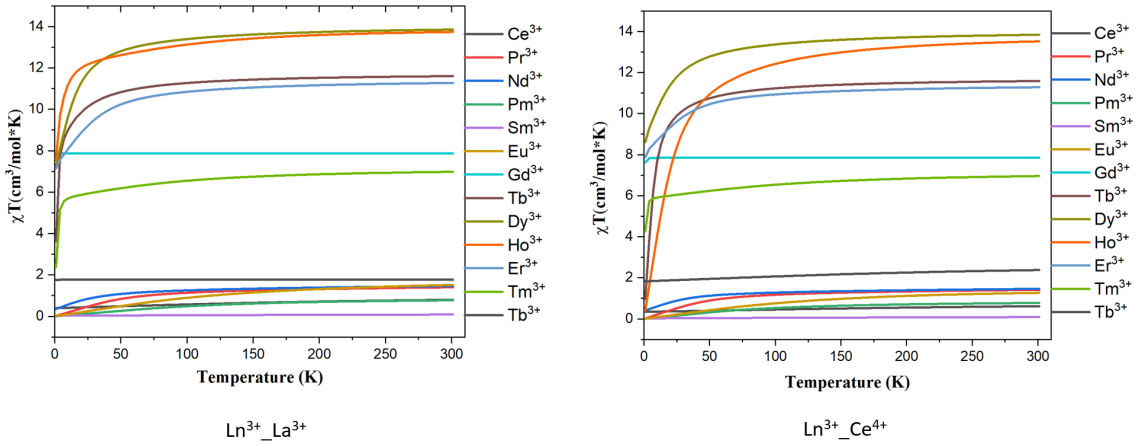

Figure 62: Calculated temperature dependent molar magnetic susceptibility of Ln^{3+}_La^{3+} (left) and Ln^{3+}_Ce^{4+} (right) vacancy clusters.

5.9 Conclusion

In this chapter, the structural, magnetic and optical properties of model clusters based on CeO_2 structures were investigated using embedded cluster models.

At first the structural properties of the model clusters were investigated. The dimensions of the model clusters were evaluated to ascertain a size that rapidly converges, utilizing geometrical parameters as a descriptor. It was determined that a cluster containing two metal centers suffices to closely match the experimental structure, and thus, this model cluster was selected for the majority of the calculations. Moreover, the significance of local geometry relaxation was emphasized. Geometry relaxation of local environment surrounding Ce^{3+} ions is crucial for achieving a reasonable estimation of zero-field splitting.

Following the initial investigations, the focus shifted to studying clusters containing oxygen vacancies as the next step. In model clusters featuring a single oxygen vacancy, electronic structure calculations revealed that unpaired electrons tend to localize on the cerium atom adjacent to the vacancy. This localization results in the reduction of Ce^{4+} being reduced to Ce^{3+}.

Leveraging insights from oxygen vacancy clusters, the optical and magnetic properties of Ce^{3+} in a symmetry-reduced environment were computed. The emergence of 4f-4f excitations within the infrared range in these vacancy clusters is attributed to alterations in the electronic structure of cerium and the reduction of symmetry in its surrounding. Additionally, the magnetic properties observed are a consequence of the presence of open-shell Ce^{3+}.

In an attempt to clarify the properties of high-entropy oxides, a series of two-center model clusters containing various Ln^{3+} ions were also investigated. Due to the negligible coupling between neighbouring metal centers, calculating magnetic properties of a system with many Ln^{3+} can be simplified by treating each centers within an optimized surrounding individually. Preliminary results were obtained to simulate the absorption spectra of various Ln^{3+} centers in model cluster which can contribute to interpret spectra of complex systems.

6 Summary and conclusion

This thesis conducts a quantum chemical investigation of the structural, optical and magnetic properties of complexes containing transition metal or lanthanide ions employing various methods, including DFT, TDDFT, sTDA, ROHF, CASSCF and CASOCI. A good description of the electronic structure is crucial for interpretation and prediction of experimental spectra and magnetic measurements. It offers vital understanding of the fundamental mechanisms and can guide the development of strategies for enhancement.

In Chapter 3 the intramolecular interaction and optical properties of two lanthanide-coinage metal complexes were studied. Computational studies were conducted to examine both ground and excited state characteristics. Firstly, calculations in the ground state clarified that the short metal-metal distances in both complexes arise from ligand-ligand dispersion interactions, rather than direct metal-metal interactions. Furthermore, excited state calculations were carried out to interpret the photoluminescent emission spectra. TDDFT calculations of a simplified model complex demonstrated LMMCT in the lowest excited state and a dependency of the excitation energy decrease to shortened metal-metal distances. The results from the model complex inspired us to optimize the triplet structure of the full complexes with a shortened metal-metal distance. In the triplet structure of the full complexes, a significantly shortened Au-La distance was obtained, a LMMCT was observed and can be identified as the HOMO-LUMO transition specifically in the Au-La complex, while such an effect was absent in the Ag-La complex. The observation of LMMCT within the triplet structure indicated the potential for metal-metal interaction in the excited state. However, a direct correlation between the computed results and the emission spectra could not be established, attributed to the absence of optimized excited state structures. This limitation arose from considerations of computational cost and complexity.

In Chapter 4 the magnetic properties of two groups of lanthanide sandwich complexes containing Er^{3+} or Dy^{3+} and a trinuclear ion complex with three high spin Fe^{2+} were

investigated. The zero-field splitting, molar magnetic susceptibility and g-factors of each metal center and the coupling constants between different metal centers were calculated and compared. In experiment it was demonstrated that within the group of lanthanide complexes with the same coordination sphere, Er (3-Er and 5-Er) dimers consistently outperform both their mononuclear counterparts and Dy analogues as SMMs. These results were supported by our calculations. First of all, both 3-Er and 5-Er possess highly anisotropic and pure m_j=15/2 ground states and the highest energy to the first excited state within its own group. In general, the Er^{3+} benefits from such a sandwich-type ligand surrounding, achieving higher energy for the first excited state and ground state magnetic anisotropy. Additionally, the orientation of ground state magnetic main axes changed from rather perpendicular to the central ligand plane in the Er complexes to more tilted main axes in the Dy analogues. This is a result of Dy^{3+} being sensitive to the ligand structure outside of the first coordination sphere. Lastly, the impact of another metal center was evaluated by comparing the mononuclear and dinuclear complexes with the same coordination and metal type. Regarding the energy barrier of the first excited KDs, the introduction of a second metal center leads to divergent phenomena: in Er complexes, the energy barrier is elevated, whereas in Dy complexes a decrease in energy barrier appeared. This weak coupling leads to the suppression of quantum tunnelling of magnetization (QTM) in Er dimers, whereas it results in more low-lying microstates for Dy dimers. Therefore, barrier-less magnetic relaxation pathways were possible for Dy dimers. In the research field of SMMs, securing a high energy barrier for the excited state does not necessarily ensure optimal SMM performance. This is because magnetic relaxation processes, such as QTM that occurs at low temperatures, can effectively make the magnetic reversal barrier-less. A careful ligand design to enhance magnetic anisotropy and increase excited state energies together with a strategy to inhibit low temperature magnetic relaxation is a promising approach. The equatorial ligands that were presented in this chapter facilitate the magnetic behaviour of prolate-shaped Er^{3+}. Introducing metal-metal interactions is an effective method to achieve a suppression of QTM.

In Chapter 5 the molecular approach was extended to lanthanide oxides through the use of an embedded cluster model, with a focus on cerium oxide in this thesis. Initially, both perfect and defect quantum clusters of various sizes were examined to reach a balance between accurately describing the properties of interest and computational complexity. Regards of both geometrical parameters and electronic properties, a 2-center cluster was sufficient to achieve a good description and remain computationally

efficient, thus was adopted as a model in most calculations. Furthermore, the significance of local geometry relaxation was emphasized in achieving accurate descriptions of zero-field splitting and absorption spectra in the defect clusters. Moreover, to explore the optical and magnetic properties of high-entropy oxides (HEOs), other open-shell Ln^{3+} ions were incorporated into the quantum cluster. HEOs embody significant complexity, presenting a challenge for an accurate description through quantum chemical methods. The coupling between nearest neighbouring metal centers was found to be small, therefore, to reduce computational complexity, optical and magnetic properties were calculated with substituting all besides one of the centers by diamagnetic La^{3+}/Ce^{4+}. The molar magnetic susceptibility of HEOs can potentially be extrapolated from the calculations based on a simple model with only one open-shell metal. The calculated absorption spectra of the clusters containing Ln^{3+} provide a fundamental basis for interpretation of measured spectra.

In summary, this thesis demonstrated a quantum chemical approach to predict and interpret the magnetic and optical properties of complexes containing lanthanides or transition metals. Achieving an accurate description of the electronic structure is crucial, necessitating the explicit treatment of local coordination environments of the metal centers.

A Appendix

A Appendix For Chapter 2

Electron Configuration	a	b
$4f^1$	0	0
$4f^2$	7/12	7/6
$4f^3$	7/9	14/9
$4f^4$	7/8	7/4
$4f^5$	14/15	28/15
$4f^6$	35/36	35/18
$4f^7$	1	2
$4f^8$	63/64	49/32
$4f^9$	238/243	308/243
$4f^{10}$	49/50	28/25
$4f^{11}$	119/121	126/121
$4f^{12}$	427/432	217/216
$4f^{13}$	168/169	167/169
$4f^{14}$	1	1

Table A1: Calculated Roothaan Parameters for the electron configuration of [Xe]$4f^1$ to [Xe]$4f^{14}$

B Appendix For Chapter 4

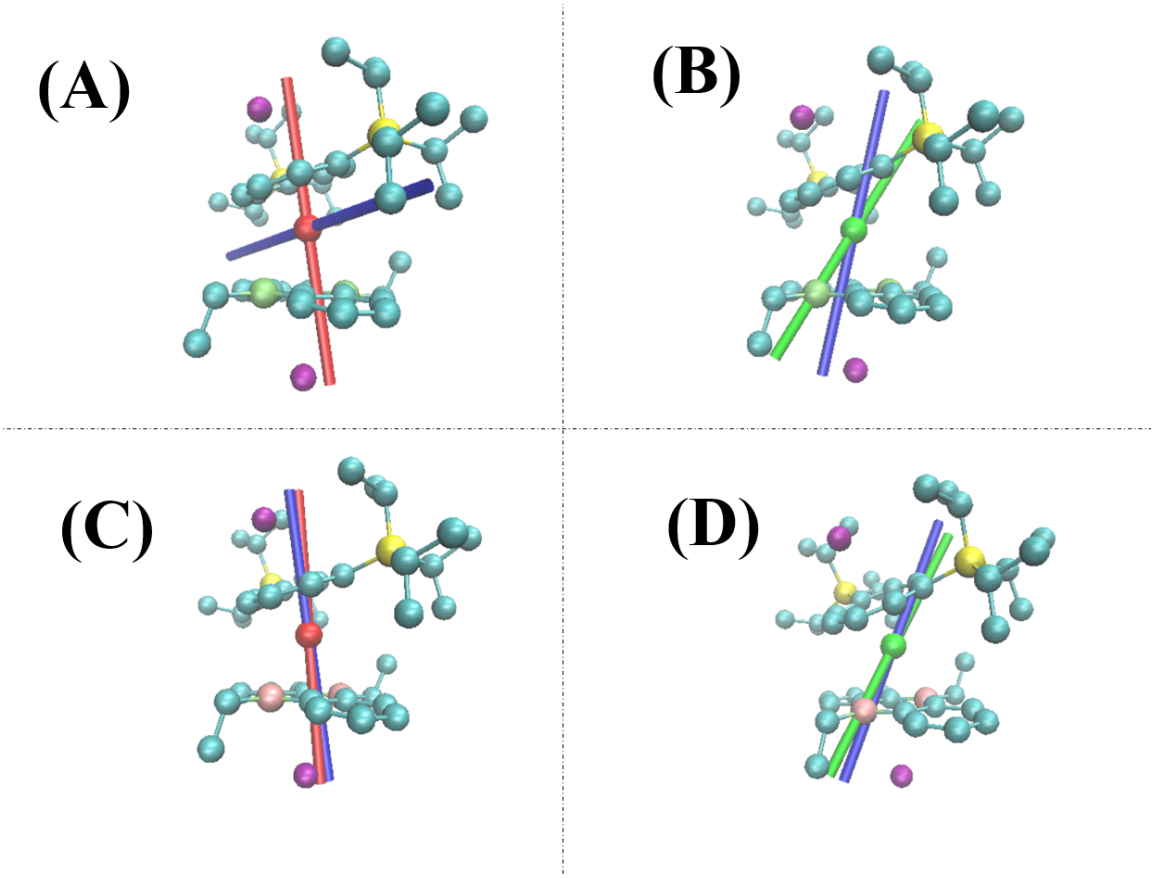

Figure A1: Plotted magnetic main axes of the ground KDs (red/green for Er/Dy complexes) and the second KDs (blue) of 2-Er (A,C) and 2-Dy (B,D). (C: cyan; H: white; Si: yellow; K: purple; B: pink; Er: red; Dy: green; hydrogens are omitted for clarity).

	2-Er		2-Dy	
	g-values (g_x, g_y, g_z)	Energy level (cm^{-1})	g-values (g_x, g_y, g_z)	Energy level (cm^{-1})
	0.02		0.00	
1st KD	0.03	0	0.01	0
	17.72		19.98	
	1.25		0.25	
2nd KD	5.15	44.45	0.95	80.56
	13.46		13.20	
	2.11		0.12	
3rd KD	3.95	74.68	1.17	99.78
	7.18		12.95	
	0.34		1.32	
4th KD	0.59	88.33	1.82	154.72
	15.49		12.46	
	1.15		3.98	
5th KD	1.61	125.46	6.23	174.75
	8.76		9.92	
	0.14		1.23	
6th KD	0.47	160.81	2.25	226.54
	12.16		15.69	
	0.10		0.06	
7th KD	0.14	212.17	0.16	346.48
	16.65		19.75	
	0.02		0.01	
8th KD	0.04	281.64	0.02	399.28
	16.91		19.83	

Table A2: Calculated g-factors of the first 8 KDs of 2-Er and 2-Dy with corresponding energy based on ROHF-optimized orbitals.

	3-Er		3-Dy	
	g-values (g_x, g_y, g_z)	energy level (cm^{-1})	g-values (g_x, g_y, g_z)	energy level (cm^{-1})
	0.01		0.03	
1st KD	0.01	0	0.05	0
	17.86		19.57	
	0.09		0.81	
2nd KD	0.12	97.9	1.73	57.21
	16.31		15.38	
	1.08		1.39	
3rd KD	3.61	135.95	2.69	82.52
	13.91		11.98	
	7.91		8.48	
4th KD	4.99	165.42	5.52	110.85
	1.22		2.33	
	0.26		2.37	
5th KD	2.28	197.8	4.23	138.78
	8.33		13.09	
	1.31		0.18	
6th KD	4.12	218.4	0.39	193.78
	7.86		18.62	
	0.17		0.08	
7th KD	0.56	286.4	0.17	225.99
	15.98		17.09	
	0.12		0.00	
8th KD	0.35	325.2	0.00	556.6
	16.45		19.84	

Table A3: Calculated g-factors of the first 8 KDs of 3-Er and 3-Dy with corresponding energy based on ROHF-optimized orbitals.

				x	y	z
2-Er	1st KD	g_x	0.00	-0.163	0.900	-0.404
		g_y	0.00	-0.987	-0.150	0.065
		g_z	17.81	-0.002	0.409	0.912
	2nd KD	g_x	0.11	0.897	-0.150	-0.416
		g_y	1.56	0.065	0.975	-0.212
		g_z	10.76	0.437	0.163	0.884
2-Dy	1st KD	g_x	0.00	0.879	0.186	0.439
		g_y	0.00	0.477	-0.337	-0.812
		g_z	19.79	-0.003	0.923	-0.385
	2nd KD	g_x	0.22	0.998	-0.061	0.005
		g_y	0.53	-0.028	-0.527	-0.849
		g_z	14.90	0.054	0.848	-0.528
3-Er	1st KD	g_x	0.00	0.737	0.295	0.608
		g_y	0.00	-0.075	-0.858	0.507
		g_z	17.88	0.672	-0.419	-0.610
	2nd KD	g_x	0.01	0.778	0.628	-0.018
		g_y	0.02	-0.567	0.690	-0.449
		g_z	16.44	-0.270	0.360	0.893
3-Dy	1st KD	g_x	0.01	0.374	-0.138	0.917
		g_y	0.03	0.025	-0.987	-0.159
		g_z	19.41	0.927	0.082	-0.366
	2nd KD	g_x	0.83	0.387	0.141	0.911
		g_y	1.71	0.542	-0.834	-0.101
		g_z	16.38	0.746	0.533	-0.399

Table A4: Calculated magnetic main axes of the first and second KDs of 2-Er, 2-Dy, 3-Er and 3-Dy based on CASSCF-optimized (lowest RS term) orbitals.

				x	y	z
4-Er	1st KD	g_x	0.00	0.491	0.015	0.871
		g_y	0.00	0.772	-0.471	-0.427
		g_z	17.81	0.404	0.882	-0.243
	2nd KDs	g_x	0.01	0.517	0.096	0.850
		g_y	0.01	0.839	-0.255	-0.481
		g_z	15.62	0.170	0.962	-0.213
4-Dy	1st KD	g_x	0.04	0.953	-0.290	-0.093
		g_y	0.05	0.194	0.813	-0.549
		g_z	19.66	0.234	0.505	0.831
	2nd KDs	g_x	0.15	0.148	0.989	0.018
		g_y	0.25	-0.988	0.147	0.041
		g_z	18.25	0.038	-0.024	0.999
5-Er	1st KD	g_x	0.00	0.058	-0.244	0.968
		g_y	0.00	-0.155	-0.960	-0.232
		g_z	17.89	0.986	-0.137	-0.094
	2nd KDs	g_x	0.00	0.045	-0.076	0.996
		g_y	0.00	-0.334	-0.941	-0.057
		g_z	15.61	0.941	-0.330	-0.067
5-Dy	1st KD	g_x	0.36	0.592	0.800	-0.099
		g_y	1.44	-0.766	0.597	0.238
		g_z	18.32	0.250	-0.065	0.966
	2nd KDs	g_x	0.56	-0.023	0.993	-0.114
		g_y	1.10	-0.997	-0.031	-0.071
		g_z	16.86	-0.074	0.112	0.991

Table A5: Calculated magnetic main axes of the first and second KDs of 4-Er, 4-Dy, 5-Er and 5-Dy based on CASSCF-optimized (lowest RS term) orbitals.

m_j	1st KD	2nd KD	3rd KD	4th KD	5th KD	6th KD	7th KD	8th KD
± 7.5	0.978	0.003	0.002	0.001	0.002	0.003	0.000	0.009
± 6.5	0	0.344	0.174	0.014	0.227	0.045	0.008	0.189
± 5.5	0.017	0.193	0.191	0.02	0.058	0.017	0.006	0.498
± 4.5	0.001	0.025	0.058	0.087	0.421	0.129	0.003	0.276
± 3.5	0.005	0.007	0.004	0.18	0.22	0.447	0.121	0.015
± 2.5	0	0.144	0.12	0.346	0.032	0.05	0.305	0.002
± 1.5	0	0.173	0.299	0.118	0.007	0.065	0.330	0.007
± 0.5	0	0.11	0.152	0.234	0.032	0.244	0.225	0.003

Table A6: Calculated m_j composition of each Kramer's Doublet in the ground state of 2-Er.

m_j	1st KD	2nd KD	3rd KD	4th KD	5th KD	6th KD	7th KD	8th KD
± 7.5	0.988	0	0	0.005	0.003	0.001	0	0.003
± 6.5	0	0.82	0.11	0.002	0.029	0.005	0.001	0.032
± 5.5	0.006	0.001	0.034	0.781	0.021	0.03	0.004	0.123
± 4.5	0.004	0.038	0.044	0.026	0.372	0.245	0.037	0.235
± 3.5	0.001	0.04	0.105	0.055	0.138	0.273	0.115	0.272
± 2.5	0	0.018	0.201	0.063	0.057	0.267	0.181	0.213
± 1.5	0.001	0.029	0.246	0.05	0.133	0.153	0.291	0.098
± 0.5	0	0.053	0.261	0.018	0.248	0.026	0.371	0.023

Table A7: Calculated m_j composition of each Kramer's Doublet in the ground state of 2-Dy.

m_j	1st KD	2nd KD	3rd KD	4th KD	5th KD	6th KD	7th KD	8th KD
± 7.5	0.99	0.001	0	0	0.001	0.003	0.002	0.002
± 6.5	0	0.62	0.024	0.193	0.047	0.013	0.05	0.052
± 5.5	0.007	0.312	0.041	0.121	0.034	0.043	0.218	0.224
± 4.5	0.001	0.051	0.046	0.406	0.05	0.03	0.171	0.245
± 3.5	0.002	0.008	0.03	0.076	0.192	0.549	0.069	0.074
± 2.5	0	0.006	0.275	0.054	0.248	0.071	0.195	0.15
± 1.5	0	0.001	0.429	0.041	0.049	0.123	0.195	0.161
± 0.5	0	0.001	0.155	0.108	0.378	0.168	0.099	0.091

Table A8: Calculated m_j composition of each Kramer's Doublet in the ground state of 3-Er.

m_j	1st KD	2nd KD	3rd KD	4th KD	5th KD	6th KD	7th KD	8th KD
± 7.5	0.92	0.01	0.023	0.034	0.004	0.007	0.002	0.000
± 6.5	0	0.57	0.297	0.030	0.028	0.057	0.017	0.001
± 5.5	0.075	0.093	0.211	0.349	0.044	0.142	0.077	0.009
± 4.5	0.001	0.227	0.181	0.099	0.128	0.151	0.175	0.038
± 3.5	0.004	0.05	0.128	0.262	0.140	0.088	0.226	0.103
± 2.5	0	0.02	0.08	0.075	0.271	0.169	0.185	0.200
± 1.5	0	0.017	0.046	0.076	0.121	0.296	0.148	0.295
± 0.5	0	0.013	0.034	0.075	0.264	0.090	0.170	0.352

Table A9: Calculated m_j composition of each Kramer's Doublet in the ground state of 3-Dy.

m_j	1st KD	2nd KD	3rd KD	4th KD	5th KD	6th KD	7th KD	8th KD
± 7.5	0.978	0.001	0.000	0.018	0.001	0.000	0.000	0.001
± 6.5	0	0.880	0.000	0.108	0.005	0.004	0.001	0.002
± 5.5	0.014	0.088	0.003	0.685	0.026	0.019	0.138	0.026
± 4.5	0.007	0.020	0.002	0.143	0.012	0.080	0.429	0.306
± 3.5	0	0.010	0.024	0.003	0.058	0.278	0.108	0.519
± 2.5	0	0.000	0.134	0.010	0.161	0.312	0.246	0.136
± 1.5	0	0.000	0.337	0.004	0.334	0.245	0.070	0.009
± 0.5	0	0.000	0.499	0.030	0.403	0.061	0.006	0.001

Table A10: Calculated m_j composition of each Kramer's Doublet in the ground state of 4-Er.

m_j	1st KD	2nd KD	3rd KD	4th KD	5th KD	6th KD	7th KD	8th KD
± 7.5	0.983	0.000	0.006	0.002	0.001	0.004	0.004	0.001
± 6.5	0.000	0.669	0.189	0.058	0.033	0.017	0.027	0.008
± 5.5	0.001	0.300	0.224	0.133	0.145	0.077	0.089	0.031
± 4.5	0.014	0.021	0.434	0.076	0.077	0.130	0.165	0.084
± 3.5	0.001	0.003	0.036	0.387	0.201	0.049	0.166	0.157
± 2.5	0.001	0.001	0.050	0.088	0.309	0.225	0.105	0.220
± 1.5	0.000	0.005	0.034	0.139	0.028	0.393	0.152	0.249
± 0.5	0.000	0.002	0.028	0.116	0.206	0.105	0.293	0.251

Table A11: Calculated m_j composition of each Kramer's Doublet in the ground state of 4-Dy.

m_j	1st KD	2nd KD	3rd KD	4th KD	5th KD	6th KD	7th KD	8th KD
± 7.5	0.991	0.000	0.001	0.005	0.000	0.001	0.002	0.000
± 6.5	0.000	0.929	0.004	0.059	0.001	0.001	0.003	0.004
± 5.5	0.003	0.051	0.085	0.740	0.008	0.017	0.095	0.001
± 4.5	0.006	0.008	0.020	0.078	0.019	0.118	0.619	0.132
± 3.5	0.000	0.011	0.025	0.012	0.031	0.106	0.158	0.657
± 2.5	0.000	0.000	0.121	0.008	0.104	0.508	0.063	0.196
± 1.5	0.000	0.000	0.277	0.031	0.411	0.235	0.043	0.004
± 0.5	0.000	0.000	0.468	0.066	0.427	0.014	0.018	0.006

Table A12: Calculated m_j composition of each Kramer's Doublet in the ground state of 5-Er.

m_j	1st KD	2nd KD	3rd KD	4th KD	5th KD	6th KD	7th KD	8th KD
± 7.5	0.801	0.031	0.146	0.013	0.005	0.003	0.001	0.000
± 6.5	0.012	0.684	0.242	0.020	0.014	0.010	0.015	0.004
± 5.5	0.112	0.188	0.301	0.182	0.125	0.012	0.063	0.018
± 4.5	0.061	0.060	0.214	0.196	0.185	0.081	0.146	0.056
± 3.5	0.008	0.018	0.012	0.358	0.172	0.104	0.205	0.124
± 2.5	0.001	0.009	0.025	0.089	0.328	0.149	0.192	0.207
± 1.5	0.003	0.009	0.019	0.081	0.064	0.373	0.175	0.277
± 0.5	0.003	0.002	0.041	0.060	0.108	0.267	0.203	0.315

Table A13: Calculated m_j composition of each Kramer's Doublet in the ground state of 5-Dy.

k	q	2-Er	2-Dy	3-Er	3-Dy
2	-2	2.40E-01	-1.89E-01	2.99E-01	-2.39E+00
2	-1	-4.34E-01	2.26E+00	5.17E-01	1.58E+00
2	0	-9.21E-01	-1.46E+00	-1.61E+00	-2.45E+00
2	1	-1.42E+00	1.28E+00	-1.80E+00	-3.93E+00
2	2	1.04E+00	5.79E-01	5.94E-01	4.39E+00
4	-4	-6.70E-04	-1.70E-02	-1.10E-03	-3.64E-02
4	-3	-1.83E-03	-3.26E-03	3.60E-03	4.11E-02
4	-2	-4.99E-04	1.64E-02	5.39E-04	1.10E-02
4	-1	-4.67E-03	-1.48E-02	4.37E-03	-1.18E-02
4	0	-5.33E-03	-3.48E-03	-5.37E-03	2.77E-03
4	1	-2.20E-02	-8.45E-03	-2.01E-02	2.99E-02
4	2	2.69E-04	-1.09E-02	5.70E-04	-1.54E-02
4	3	-3.65E-03	-8.80E-02	-4.55E-03	-3.30E-02
4	4	-2.41E-03	-7.11E-03	-3.05E-03	1.26E-02
6	-6	-1.05E-05	-2.30E-05	-9.56E-06	-8.81E-05
6	-5	5.28E-05	-1.01E-04	2.40E-04	9.41E-05
6	-4	-5.09E-05	-3.12E-05	-5.36E-05	1.53E-04
6	-3	-6.56E-05	6.54E-05	8.46E-05	-1.02E-04
6	-2	1.93E-05	-1.24E-04	-1.23E-05	-1.36E-04
6	-1	1.39E-04	4.31E-05	-1.49E-04	4.58E-05
6	0	-2.09E-05	1.34E-05	-9.43E-06	-1.92E-05
6	1	4.76E-04	2.41E-05	5.17E-04	-1.38E-04
6	2	1.37E-04	1.00E-04	1.08E-04	1.26E-04
6	3	-1.27E-04	1.77E-04	-1.36E-04	1.36E-04
6	4	-9.65E-05	-1.46E-05	-1.06E-04	-2.77E-05
6	5	-9.26E-05	2.39E-05	-7.41E-05	-2.17E-04
6	6	1.69E-06	-3.16E-05	-3.04E-06	1.68E-05

Table A14: The extended Stevens operator coefficients B_k^q extracted from CASOCI calculations of 2-Er, 2-Dy, 3-Er and 3-Dy (for 3-Er and 3-Dy, the calculation was done for the individual centers).

k	q	4-Er	4-Dy	5-Er	5-Dy
2	-2	4.85E-01	-1.63E+00	2.52E-01	2.23E+00
2	-1	6.58E-01	6.17E+00	-5.26E-01	-2.89E+00
2	0	-1.81E+00	-2.42E+00	-2.03E+00	-1.70E+00
2	1	-4.86E-01	-8.47E-01	2.24E-01	-1.01E+00
2	2	5.06E-01	-4.61E+00	4.63E-01	-2.14E+00
4	-4	1.98E-04	2.78E-02	-1.26E-04	-3.08E-02
4	-3	-6.01E-03	-6.69E-02	7.35E-03	1.70E-02
4	-2	1.54E-03	4.31E-03	7.33E-04	-1.03E-02
4	-1	8.10E-03	-3.90E-02	-6.26E-03	2.22E-02
4	0	-6.27E-03	1.60E-03	-6.32E-03	2.37E-03
4	1	-1.44E-03	5.03E-03	2.70E-03	7.88E-03
4	2	1.73E-03	1.45E-02	1.57E-03	1.33E-02
4	3	8.96E-03	4.87E-02	-8.25E-03	4.52E-02
4	4	-7.51E-04	2.11E-02	-5.78E-04	-5.37E-03
6	-6	2.11E-05	-1.80E-04	2.92E-06	1.75E-04
6	-5	6.17E-05	4.49E-04	9.09E-05	-5.12E-05
6	-4	3.14E-05	7.70E-06	-1.09E-05	5.66E-06
6	-3	-1.32E-04	5.53E-05	1.91E-04	2.18E-05
6	-2	8.48E-05	5.24E-06	7.88E-06	1.08E-05
6	-1	-2.98E-04	5.23E-05	2.12E-04	1.50E-06
6	0	1.85E-05	1.32E-06	1.64E-05	-5.58E-08
6	1	1.05E-04	-9.79E-06	-8.35E-05	-1.96E-05
6	2	8.70E-05	-1.46E-06	4.03E-05	1.93E-05
6	3	2.37E-04	-5.28E-05	-2.18E-04	-4.69E-05
6	4	-2.18E-05	1.65E-05	-1.81E-05	-4.37E-06
6	5	4.61E-05	-2.43E-04	2.25E-05	-2.59E-04
6	6	-3.03E-05	-1.97E-04	-2.93E-06	-7.94E-06

Table A15: The extended Stevens operator coefficients B_k^q extracted from CASOCI calculations of 4-Er, 4-Dy, 5-Er and 5-Dy (for 5-Er and 5-Dy, the calculation was done for the individual centers).

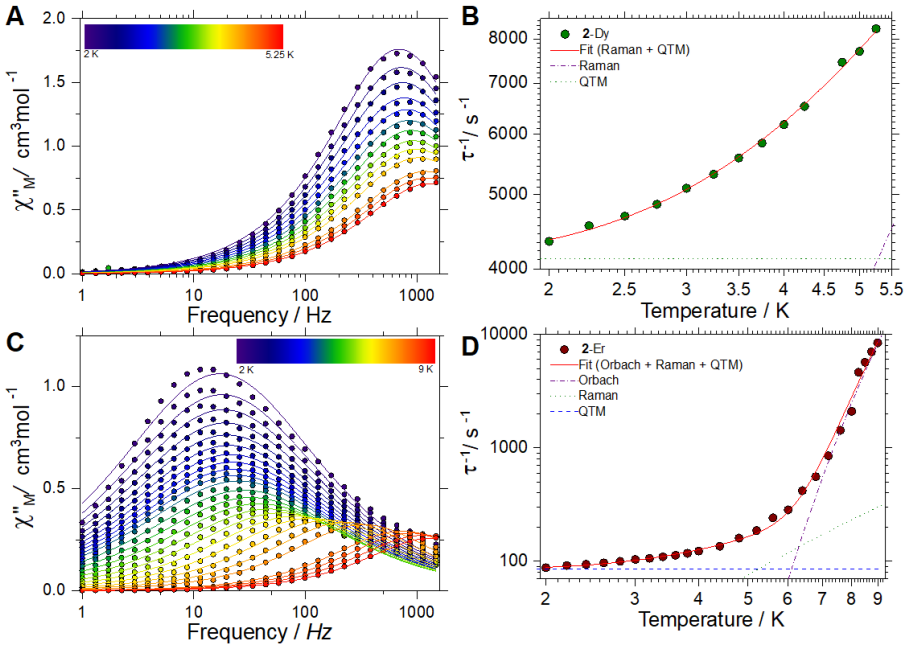

Figure A2: Out-of-phase magnetic susceptibility ($\chi''_M(\nu)$) data for complexes 2-Dy (A) and 2-Er (C) and temperature-dependent relaxation times (τ(T)) for 2-Dy (B) and 2-Er (D). Solid lines in $\chi''_M(\nu)$) are the fits to a generalised Debye model, while in τ(T) are the fits to different relaxation processes using eq.80 as described in the text.

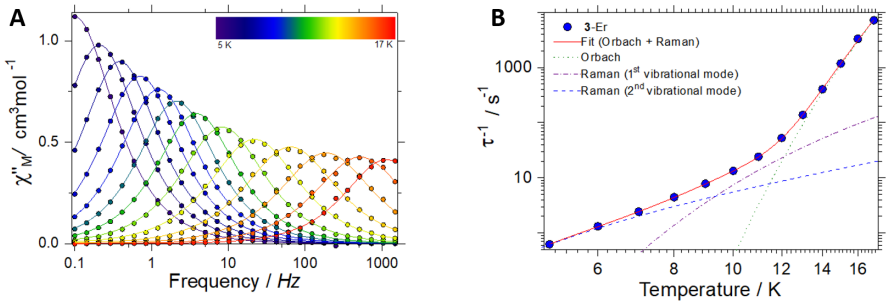

Figure A3: Out-of-phase magnetic susceptibility ($\chi''_M(\nu)$) data for complexes (A) and temperature-dependent relaxation times (τ(T)) (B) for 3-Er. Solid lines in $\chi''_M(\nu)$ are the fits to a generalised Debye model, while in τ(T) are the fits to different relaxation processes using eq.80 as described in the text.

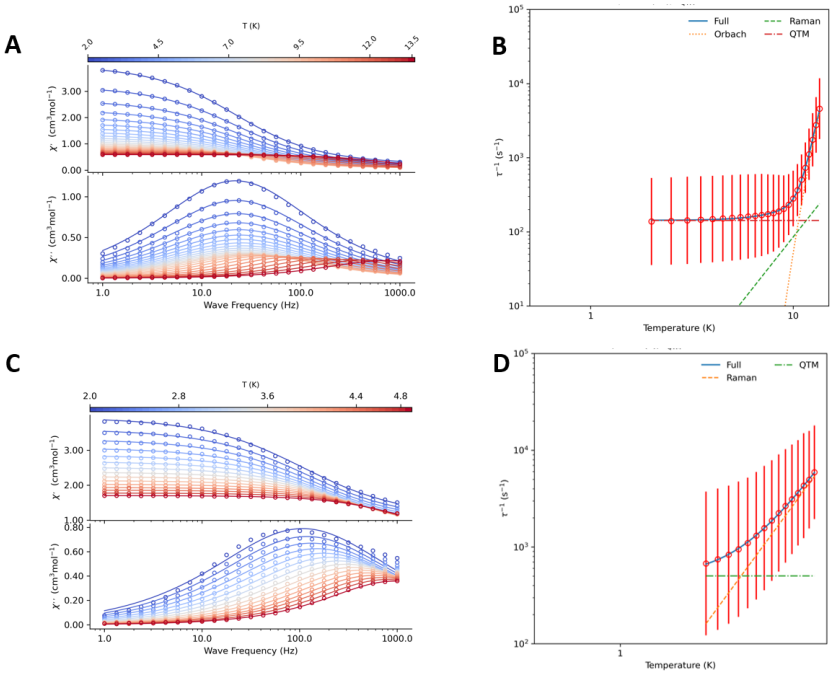

Figure A4: Out-of-phase magnetic susceptibility ($\chi''_M(\nu)$) data for complexes 4-Dy (A,) and 4-Er (C) and temperature-dependent relaxation times (τ(T)) (right column) for 4-Dy (B) and 4-Er (D). Solid lines in $\chi''_M(\nu)$) are the fits to a generalised Debye model, while in τ(T) are the fits to different relaxation processes using eq.80 as described in the text.

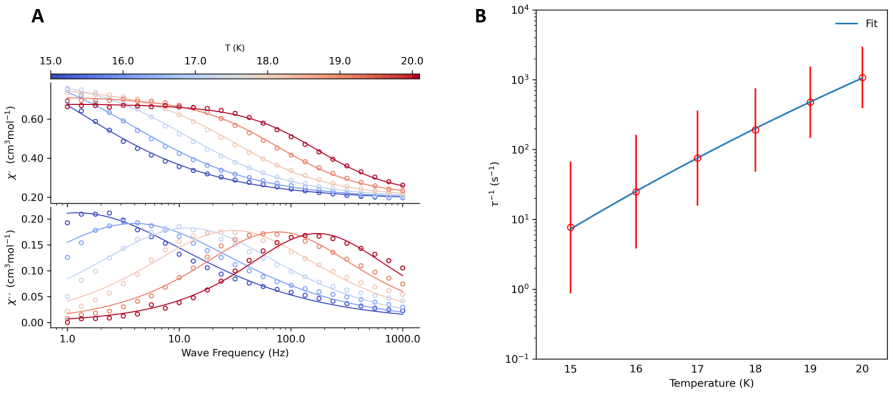

Figure A5: Out-of-phase magnetic susceptibility ($\chi''_M(\nu)$) data for complexes (A) and temperature-dependent relaxation times (τ(T)) (B) for 5-Er. Solid lines in $\chi''_M(\nu)$ are the fits to a generalised Debye model, while in τ(T) are the fits to different relaxation processes using eq.80 as described in the text.

C Appendix For Chapter 5

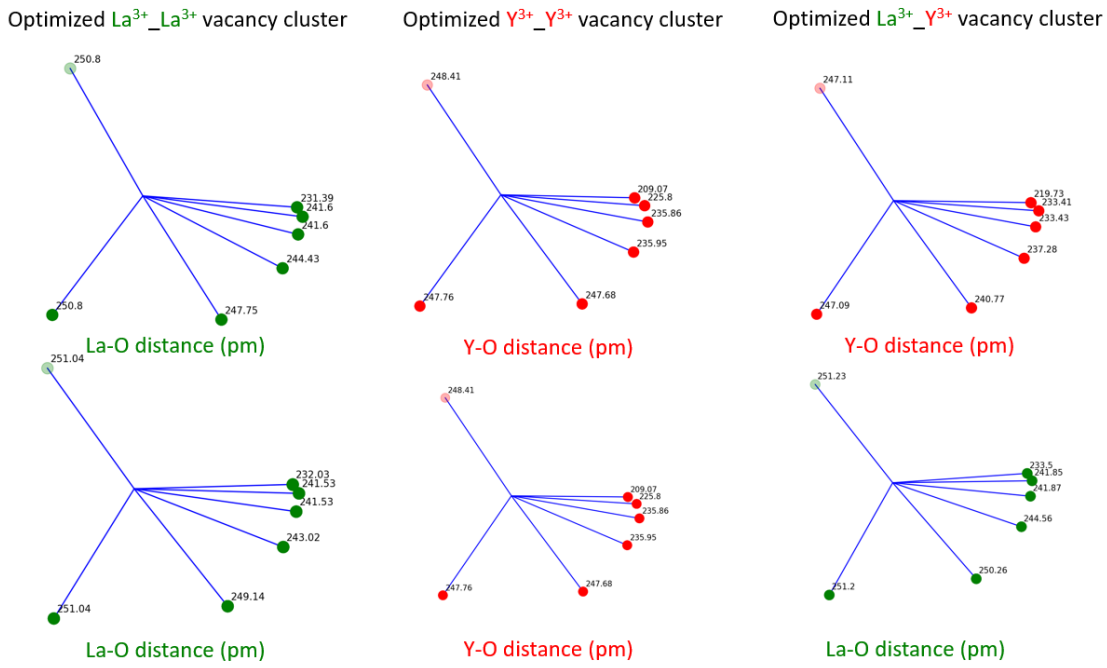

Figure A6: Ln-O distance (Å) in optimized vacancy clusters with different diamagnetic substitutions at PBE0-D3(BJ)/TZVP level.

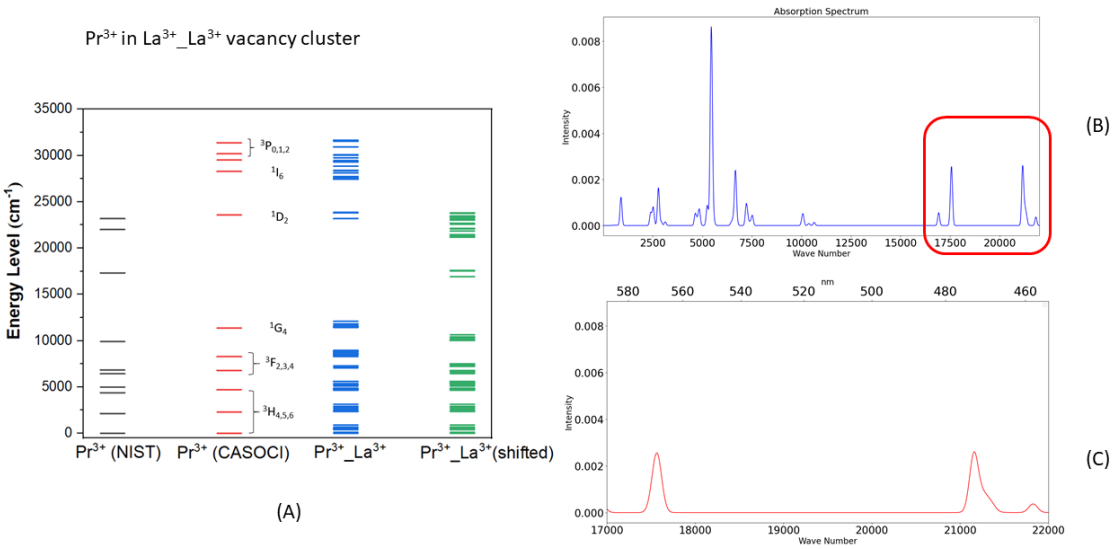

Figure A7: Calculated energy levels and the absorption spectrum of Pr^{3+} in the crystal field of the La^{3+}_La^{3+} vacancy cluster.

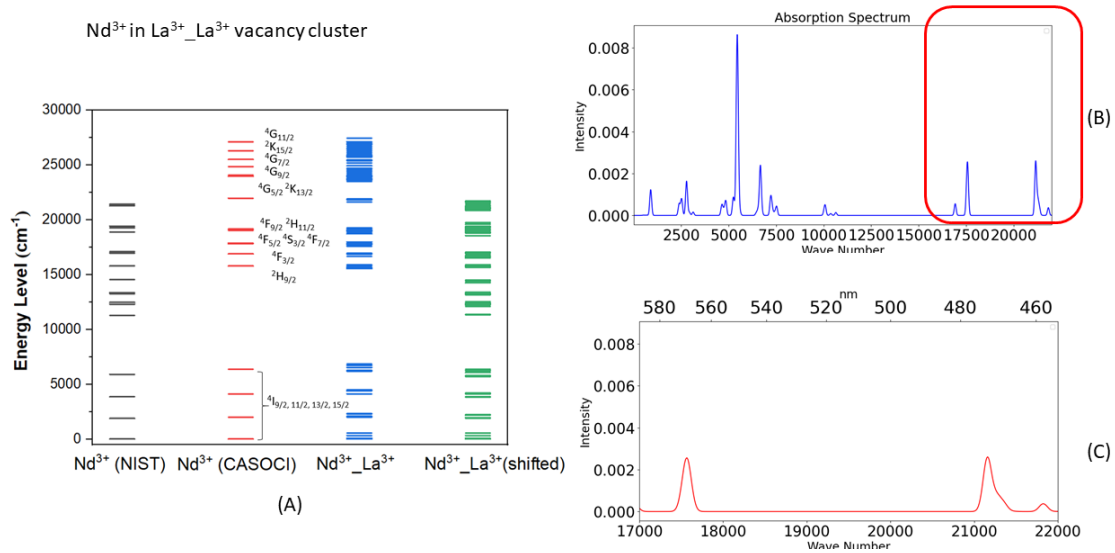

Figure A8: Calculated energy levels and the absorption spectrum of Nd^{3+} in the crystal field of the La^{3+}_La^{3+} vacancy cluster.

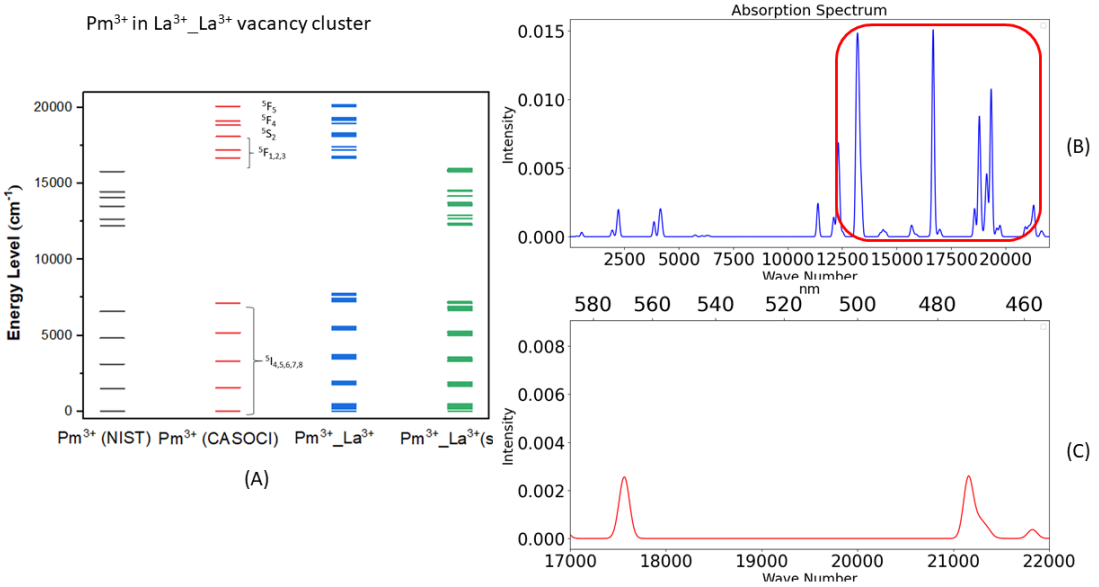

Figure A9: Calculated energy levels and the absorption spectrum of Pm^{3+} in the crystal field of the La^{3+}_La^{3+} vacancy cluster.

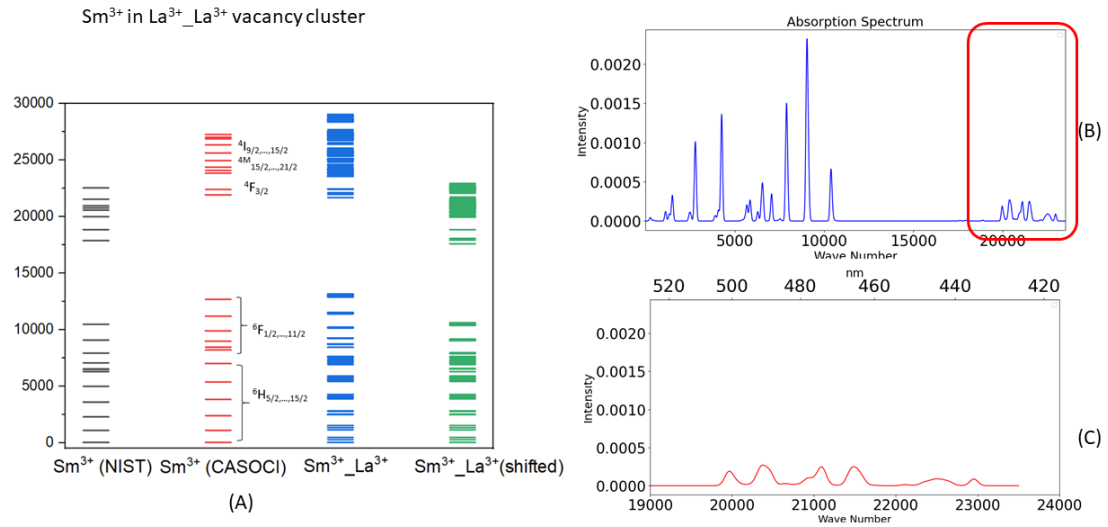

Figure A10: Calculated energy levels and the absorption spectrum of Sm^{3+} in the crystal field of the La^{3+}_La^{3+} vacancy cluster.

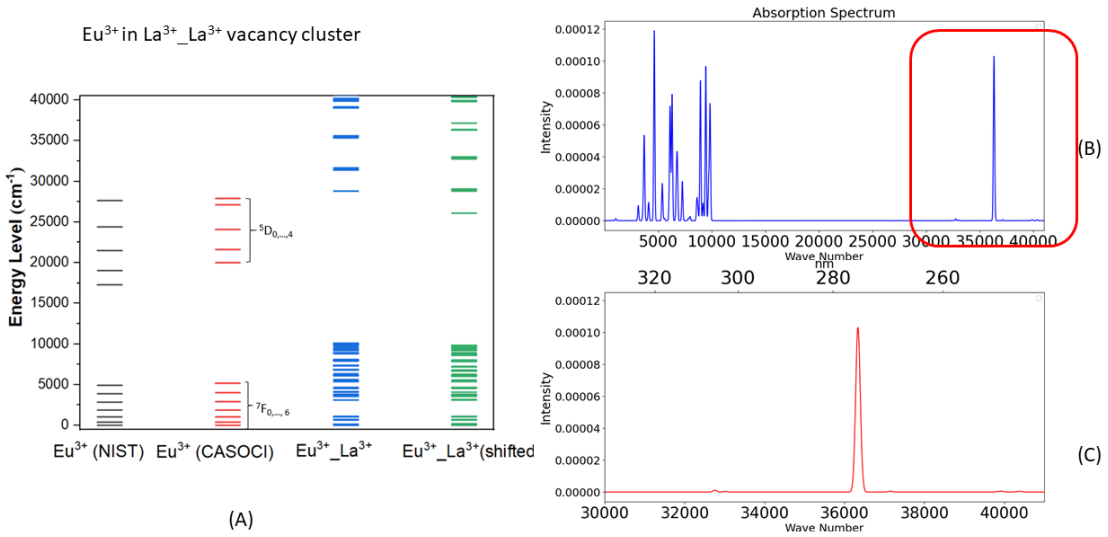

Figure A11: Calculated energy levels and the absorption spectrum of Eu^{3+} in the crystal field of the La^{3+}_La^{3+} vacancy cluster.

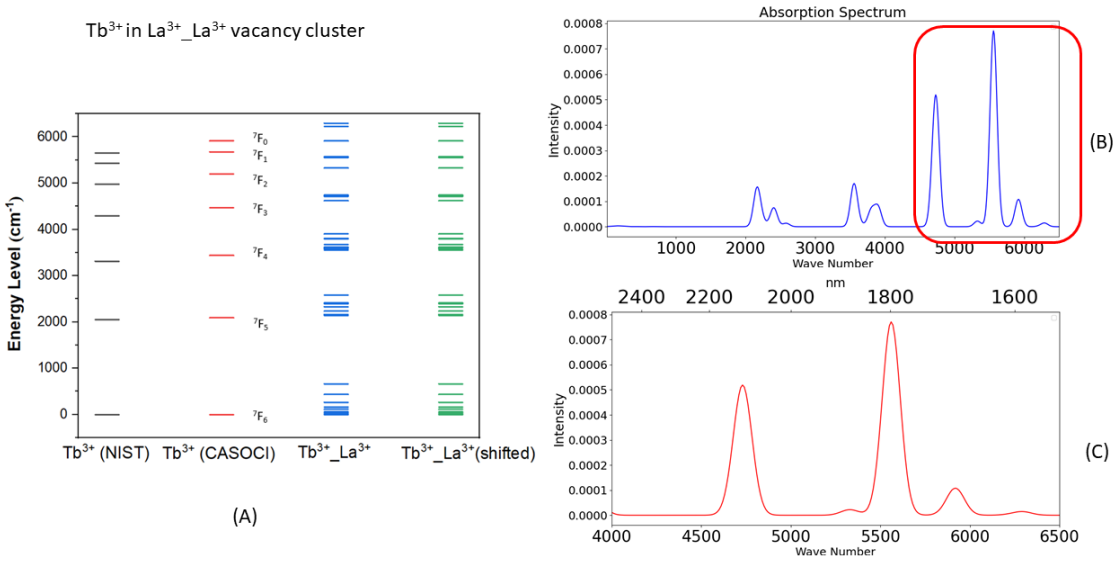

Figure A12: Calculated energy levels and the absorption spectrum of Tb^{3+} in the crystal field of the La^{3+}_La^{3+} vacancy cluster.

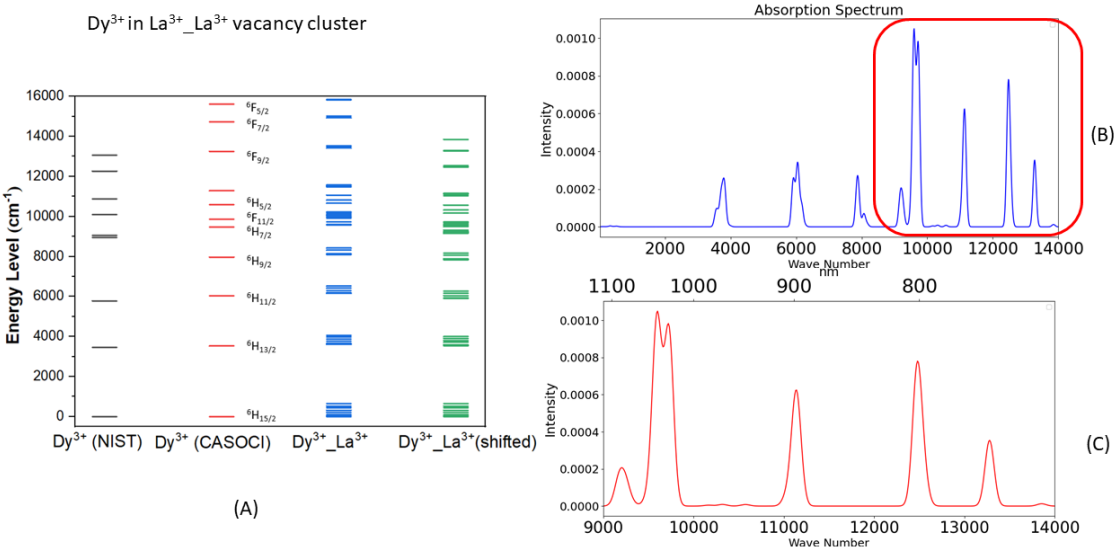

Figure A13: Calculated energy levels and the absorption spectrum of Dy^{3+} in the crystal field of the La^{3+}_La^{3+} vacancy cluster.

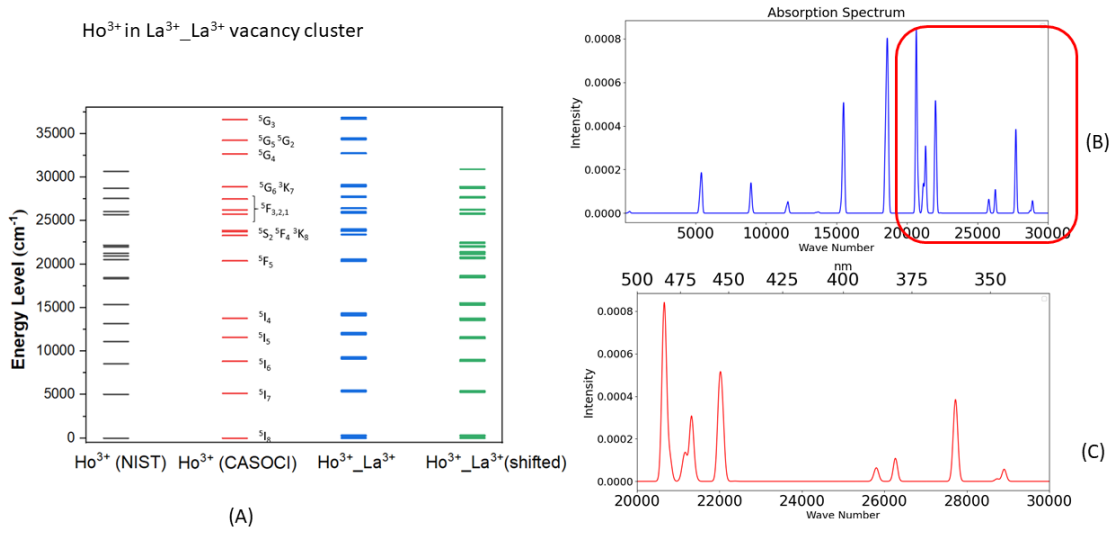

Figure A14: Calculated energy levels and the absorption spectrum of Ho^{3+} in the crystal field of the La^{3+}_La^{3+} vacancy cluster.

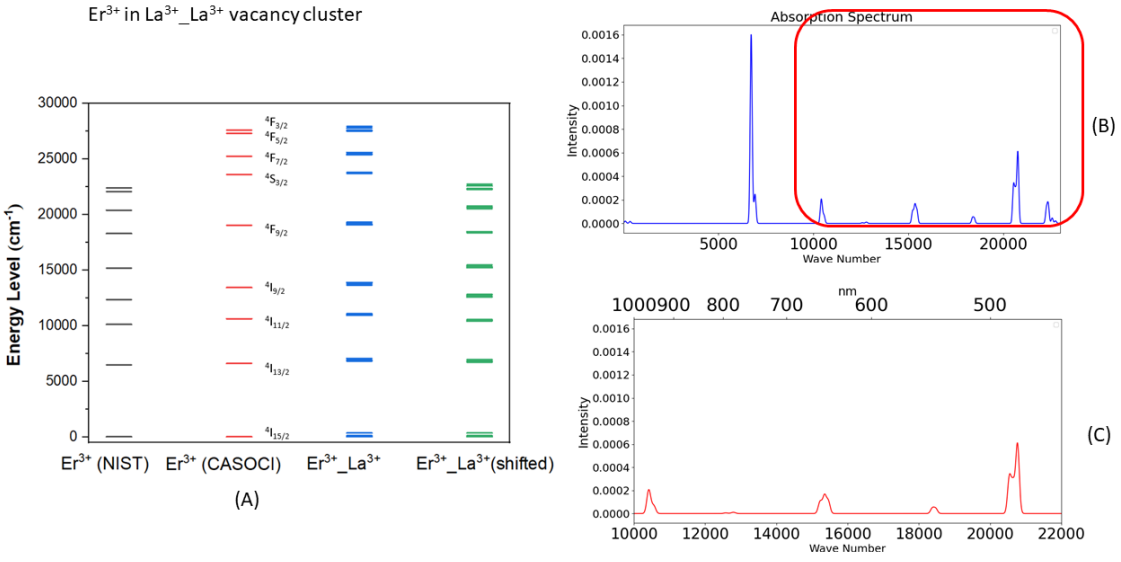

Figure A15: Calculated energy levels and the absorption spectrum of Er^{3+} in the crystal field of the La^{3+}_La^{3+} vacancy cluster.

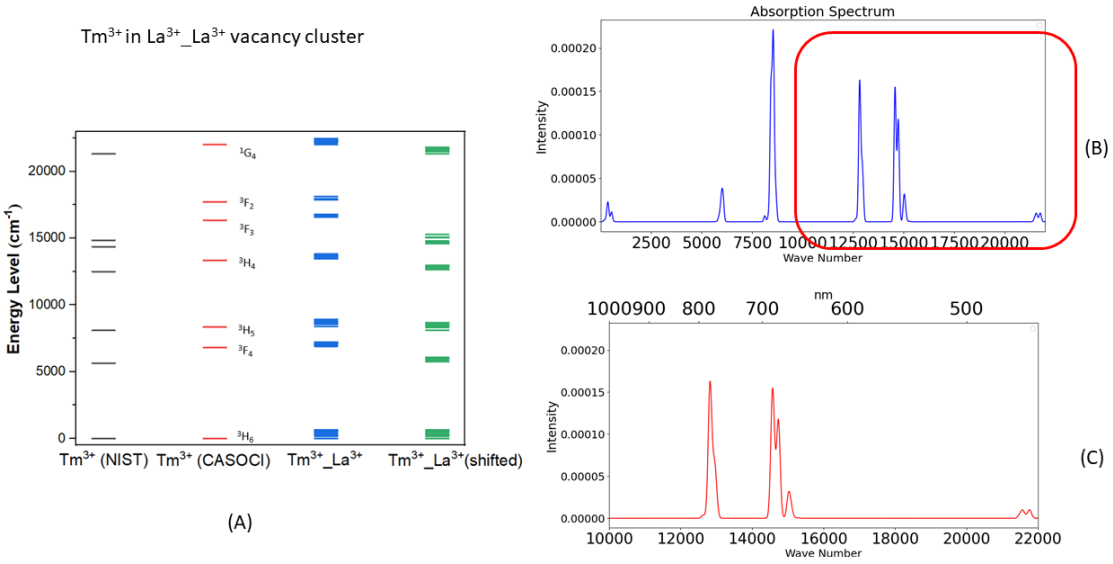

Figure A16: Calculated energy levels and the absorption spectrum of Tm^{3+} in the crystal field of the La^{3+}_La^{3+} vacancy cluster.

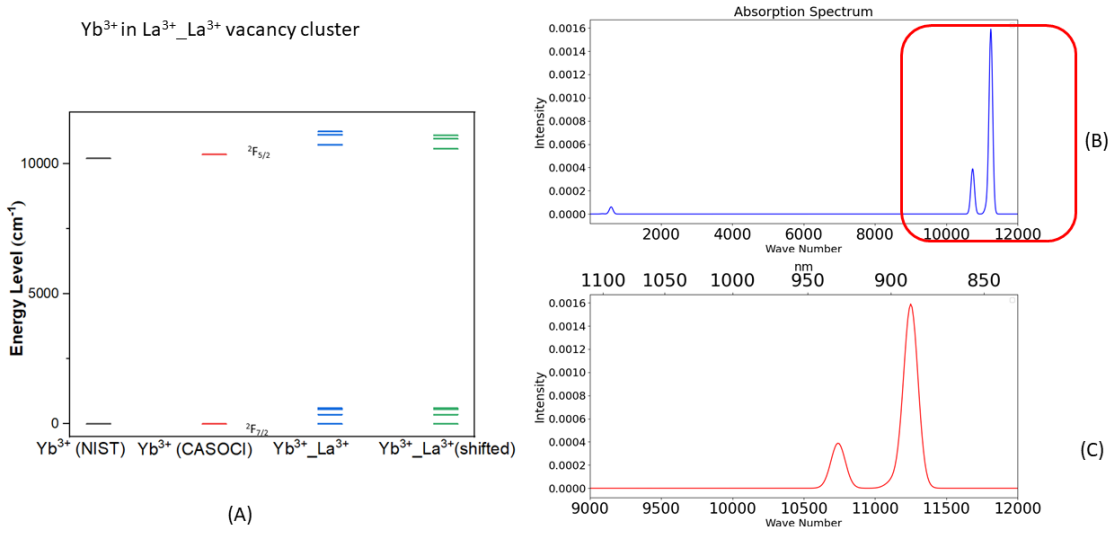

Figure A17: Calculated energy levels and the absorption spectrum of Yb^{3+} in the crystal field of the La^{3+}_La^{3+} vacancy cluster.

Bibliography

[1] D. Wang, D. Astruc, *Chem. Soc. Rev.* **2017**, *46*, 816–854.

[2] W. Zhan, Y. Guo, X. Gong, Y. Guo, Y. Wang, G. Lu, *Chinese J. Catal.s* **2014**, *35*, 1238–1250.

[3] *Molecular Catalysis of Rare-Earth Elements*, (Ed.: P. W. Roesky), Springer, Berlin, Heidelberg, **2010**.

[4] *Modern Applications of Lanthanide Luminescence*, (Ed.: A. De Bettencourt-Dias), Springer International Publishing, Cham, **2023**.

[5] N. F. Chilton, *Annu. Rev. Mater. Res.* **2022**, *52*, 79–101.

[6] Z. Zhu, M. Guo, X.-L. Li, J. Tang, *Coord. Chem. Rev.*, Special issue on the 8th Chinese Coordination Chemistry Conference **2019**, *378*, 350–364.

[7] S. T. Liddle, J. v. Slageren, *Chem. Soc. Rev.* **2015**, *44*, 6655–6669.

[8] F. Krätschmer, X. Sun, D. Frick, C. Zovko, W. Klopper, P. W. Roesky, *Inorg. Chem. Front.* **2024**, *11*, 853–862.

[9] J. Kido, K. Nagai, Y. Ohashi, *Chem. Lett.* **1990**, *19*, 657–660.

[10] J. Kido, Y. Okamoto, *Chem. Rev.* **2002**, *102*, 2357–2368.

[11] R. Sessoli, H. L. Tsai, A. R. Schake, S. Wang, J. B. Vincent, K. Folting, D. Gatteschi, G. Christou, D. N. Hendrickson, *J. Am. Chem. Soc.* **1993**, *115*, 1804–1816.

[12] R. Sessoli, D. Gatteschi, A. Caneschi, M. A. Novak, *Nature* **1993**, *365*, 141–143.

[13] T. Lis, *Acta. Cryst. B* **1980**, *36*, 2042–2046.

[14] C. A. Gould, K. R. McClain, D. Reta, J. G. C. Kragskow, D. A. Marchiori, E. Lachman, E.-S. Choi, J. G. Analytis, R. D. Britt, N. F. Chilton, B. G. Harvey, J. R. Long, *Science* **2022**, *375*, 198–202.

[15] V. D. Dergachev, D. D. Nakritskaia, S. A. Varganov, *J. Phys. Chem. Lett.* **2022**, *13*, 6749–6754.

[16] T. Bodenstein, A. Heimermann, K. Fink, C. van Wüllen, *ChemPhysChem* **2022**, *23*, e202100648.

[17] A. Szabo, N. Ostlund, *Modern Quantum Chemistry: Introduction to Advanced Electronic Structure Theory*, Dover Publications, **1996**.

[18] F. Jensen, *Introduction to computational chemistry*, John Wiley & Sons, **2007**, p. 599.

[19] A. Edmonds, *Angular Momentum in Quantum Mechanics*, **1996**.

[20] H. Lueken, *Course of lectures on magnetism of lanthanide ions under varying ligand and magnetic fields*, **2008**.

[21] T. Bodenstein, PhD thesis, Karlsruher Institut für Technologie (KIT), **2015**, 172 pp.

[22] C. C. J. Roothaan, *Rev. Mod. Phys.* **1951**, *23*, 69–89.

[23] J. A. Pople, R. K. Nesbet, *J. Chem. Phys.* **2004**, *22*, 571–572.

[24] C. C. J. Roothaan, *Rev. Mod. Phys.* **1960**, *32*, 179–185.

[25] C. van Wüllen, Mathematica script and introduction to Roothaan parameters provided by Prof. C. van Wüllen (RPTU Kaiserslautern-Landau).

[26] B. O. Roos, P. R. Taylor, P. E. M. Sigbahn, *Chem. Phys.* **1980**, *48*, 157–173.

[27] I. G. Ross, *Trans. Faraday Soc.* **1952**, *48*, 973–991.

[28] E. Rossi, G. L. Bendazzoli, S. Evangelisti, D. Maynau, *Chem. Phys. Lett.* **1999**, *310*, 530–536.

[29] B. Levy, G. Berthier, *nt. J. Quantum Chem.* **1968**, *2*, 307–319.

[30] U. Meier, V. Staemmler, *Theoret. Chim. Acta.* **1989**, *76*, 95–111.

[31] J. Almöf, B. Roos, P. Siegbahn, *Computers & Chemistry* **1978**, *2*, 89–94.

[32] J. Curély, *Monatsh. Chem.* **2005**, *136*, 1013–1036.

[33] P.-O. Löwdin, *J. Chem. Phys.* **1950**, *18*, 365–375.

[34] A. J. Amoroso, S. J. A. Pope, *Chem. Soc. Rev.* **2015**, *44*, 4723–4742.

[35] D. N. Woodruff, R. E. P. Winpenny, R. A. Layfield, *Chem. Rev.* **2013**, *113*, 5110–5148.

[36] K. Hagiwara, K. Hikasa, K. Nakamura, M. Tanabashi, M. Aguilar-Benitez, C. Amsler, R. M. Barnett, P. R. Burchat, C. D. Carone, C. Caso, G. Conforto, O. Dahl, M. Doser, S. Eidelman, J. L. Feng, L. Gibbons, M. Goodman, C. Grab, D. E. Groom, A. Gurtu, K. G. Hayes, J. J. Herna'ndez-Rey, K. Honscheid, C. Kolda, M. L. Mangano, D. M. Manley, A. V. Manohar, J. March-Russell, A. Masoni, R. Miquel, K. Mönig, H. Murayama, S. Navas, K. A. Olive, L. Pape, C. Patrignani, A. Piepke, M. Roos, J. Terning, N. A. Törnqvist, T. G. Trippe, P. Vogel, C. G. Wohl, R. L. Workman, W.-M. Yao, B. Armstrong, P. S. Gee, K. S. Lugovsky, S. B. Lugovsky, V. S. Lugovsky, M. Artuso, D. Asner, K. S. Babu, E. Barberio, M. Battaglia, H. Bichsel, O. Biebel, P. Bloch, R. N. Cahn, A. Cattai, R. S. Chivukula, R. D. Cousins, G. Cowan, T. Damour, K. Desler, R. J. Donahue, D. A. Edwards, V. D. Elvira, J. Erler, V. V. Ezhela, A. Fasso', W. Fetscher, B. D. Fields, B. Foster, D. Froidevaux, M. Fukugita, T. K. Gaisser, L. Garren, H.-J. Gerber, F. J. Gilman, H. E. Haber, C. Hagmann, J. Hewett, I. Hinchliffe, C. J. Hogan, G. Höhler, P. Igo-Kemenes, J. D. Jackson, K. F. Johnson, D. Karlen, B. Kayser, S. R. Klein, K. Kleinknecht, I. G. Knowles, P. Kreitz, Y. V. Kuyanov, R. Landua, P. Langacker, L. Littenberg, A. D. Martin, T. Nakada, M. Narain, P. Nason, J. A. Peacock, H. R. Quinn, S. Raby, G. Raffelt, E. A. Razuvaev, B. Renk, L. Rolandi, M. T. Ronan, L. J. Rosenberg, C. T. Sachrajda, A. I. Sanda, S. Sarkar, M. Schmitt, O. Schneider, D. Scott, W. G. Seligman, M. H. Shaevitz, T. Sjöstrand, G. F. Smoot, S. Spanier, H. Spieler, N. J. C. Spooner, M. Srednicki, A. Stahl, T. Stanev, M. Suzuki, N. P. Tkachenko, G. Valencia, K. van Bibber, M. G. Vincter, D. R. Ward, B. R. Webber, M. Whalley, L. Wolfenstein, J. Womersley, C. L. Woody, O. V. Zenin, *Phys. Rev. D* **2002**, *66*, 010001.

[37] H. N. Russell, F. A. Saunders, *The Astrophysical Journal* **1925**, *61*, 38.

[38] F. Hund, *Zeitschrift für Physik* **1925**, *33*, 855–859.

[39] M. Blume, R. E. Watson, *Proceedings of the Royal Society of London. Series A Mathematical and Physical Sciences* **1962**, *270*, 127–143.

[40] L. H. Thomas, *Phil. Mag. Ser. 7* **1927**, *3*, 1–21.

[41] G. Breit, *Phys. Rev.* **1930**, *36*, 383–397.

[42] G. Breit, *Phys. Rev.* **1929**, *34*, 553–573.

[43] G. Breit, *Phys. Rev.* **1932**, *39*, 616–624.

[44] W. Pauli, *Z. Physik* **1927**, *43*, 601–623.

[45] F. Neese, *J. Chem. Phys.* **2005**, *122*, 034107.

[46] J. S. Griffith, L. E. Orgel, *Q. Rev. Chem. Soc.* **1957**, *11*, 381–393.

[47] R. S. Mulliken, *Phys. Rev.* **1932**, *40*, 55–62.

[48] H. Bethe, *Annalen der Physik* **1929**, *395*, 133–208.

[49] J. H. Van Vleck, *Phys. Rev.* **1932**, *41*, 208–215.

[50] H. Lueken, C. Elschenbroich, F. Hensel, H. Hopf, *Magnetochemie*, Vieweg Teubner Verlag, Wiesbaden, **1999**.

[51] M. Atanasov, D. Ganyushin, K. Sivalingam, F. Neese in *Molecular Electronic Structures of Transition Metal Complexes II*, (Eds.: D. M. P. Mingos, P. Day, J. P. Dahl), Structure and Bonding, Springer, Berlin, Heidelberg, **2012**, pp. 149–220.

[52] Y. Tanabe, S. Sugano, *J. Phys. Soc. Jpn.* **1954**, *9*, 753–766.

[53] Y. Tanabe, S. Sugano, *J. Phys. Soc. Jpn.* **1954**, *9*, 766–779.

[54] Y. Tanabe, S. Sugano, *J. Phys. Soc. Jpn.* **1956**, *11*, 864–877.

[55] V. Staemmler, *Theoret. Chim. Acta.* **1977**, *45*, 89–94.

[56] J. Wasilewski, *Int. J. Quantum Chem.* **1989**, *36*, 503–524.

[57] K. Fink, C. Wang, V. Staemmler, *Inorg. Chem.* **1999**, *38*, 3847–3856.

[58] R. Fink, V. Staemmler, *Theoret. Chim. Acta.* **1993**, *87*, 129–145.

[59] P. J. Knowles, N. C. Handy, *Chem. Phys. Lett.* **1984**, *111*, 315–321.

[60] M. Sjøvoll, O. Gropen, J. Olsen, *Theoret. Chim. Acta.* **1997**, *97*, 301–312.

[61] E. R. Davidson, *J. Comput. Phys.* **1975**, *17*, 87–94.

[62] B. A. Heß, C. M. Marian, U. Wahlgren, O. Gropen, *Chem. Phys. Lett.* **1996**, *251*, 365–371.

[63] B. Odom, D. Hanneke, B. D'Urso, G. Gabrielse, *Phys. Rev. Lett.* **2006**, *97*, 030801.

[64] G. Gabrielse, D. Hanneke, T. Kinoshita, M. Nio, B. Odom, *Phys. Rev. Lett.* **2007**, *99*, 039902.

[65] K. Fink, V. Staemmler, *Mol. Phys.* **2013**, *111*, 2594–2605.

[66] C. Pachl, masterthesis, Karlsruher Institut für Technologie (KIT), **2023**, 158 pp.

[67] C. Mehlich, C. van Wüllen, *J. Phys. Chem. C* **2019**, *123*, 7717–7730.

[68] F. Neese, E. I. Solomon, *Inorg. Chem.* **1998**, *37*, 6568–6582.

[69] R. Boča, *Coord. Chem. Rev.* **2004**, *248*, 757–815.

[70] D. Gatteschi, R. Sessoli, J. Villain, *Molecular Nanomagnets*, Oxford University Press, **2006**.

[71] F. Neese, D. A. Pantazis, *Faraday Discuss.* **2011**, *148*, 229–238.

[72] D. Ganyushin, F. Neese, *Chem. Phys.* **2006**, *125*, 024103.

[73] K. W. H. Stevens, *Proc. Phys. Soc. A* **1952**, *65*, 209.

[74] C. Rudowicz, *J. Phys. C: Solid State Phys.* **1985**, *18*, 1415.

[75] C. Rudowicz, *J. Phys. C: Solid State Phys.* **1985**, *18*, 3837.

[76] I. D. Ryabov, *J. Magn. Reson.* **1999**, *140*, 141–145.

[77] S. Ghassemi Tabrizi, R. Rodríguez-Guzmán, C. A. Jiménez-Hoyos, *Mol. Phys.* **2023**, *121*, e2192820.

[78] A. Abragam, B. Bleaney, A. Abragam, B. Bleaney, *Electron Paramagnetic Resonance of Transition Ions*, Oxford University Press, Oxford, New York, **2012**, 726 pp.

[79] L. F. Chibotaru in *Advances in Chemical Physics*, John Wiley & Sons, Ltd, **2013**, pp. 397–519.

[80] M. Gerloch, R. F. McMeeking, *J. Chem. Soc. Dalton Trans.* **1975**, 2443–2451.

[81] C. S. Naiman, T. R. Lawrence, *J. Appl. Phys.* **2004**, *37*, 1138–1140.

[82] W. Heisenberg, *Z. Physik* **1928**, *49*, 619–636.

[83] L. Noodleman, *J. Chem. Phys.* **1981**, *74*, 5737–5743.

[84] K. Yamaguchi, Y. Takahara, T. Fueno in Applied Quantum Chemistry, (Eds.: V. H. Smith, H. F. Schaefer, K. Morokuma), Springer Netherlands, Dordrecht, **1986**, pp. 155–184.

[85] T. Soda, Y. Kitagawa, T. Onishi, Y. Takano, Y. Shigeta, H. Nagao, Y. Yoshioka, K. Yamaguchi, *Chem. Phys. Lett.* **2000**, *319*, 223–230.

[86] F. Neese, *J. Phys. Chem. Solids*, Design, Characterization and Modelling of Molecule-Based Magnetic Materials Proceedings of Symposium K, EMRS Spring Meeting, June 2003, Strasbourg, France **2004**, *65*, 781–785.

[87] D. Bhattacharya, N. Vaval, S. Pal, *Chem. Phys.* **2013**, *138*, 094108.

[88] P. E. Grabowski, D. F. Chernoff, *Phys. Rev. A* **2011**, *84*, 042505.

[89] O. Laporte, W. F. Meggers, *J. Opt. Soc. Am.* **1925**, *11*, 459–463.

[90] Z. Szakács, E. Vauthey, *J. Phys. Chem. Lett.* **2021**, *12*, 4067–4071.

[91] J.-C. G. Bünzli, S. Comby, A.-S. Chauvin, C. D. B. Vandevyver, *J. Rare Earth* **2007**, *25*, 257–274.

[92] R. C. Evans, P. Douglas, C. J. Winscom, *Coord. Chem. Rev.* **2006**, *250*, 2093–2126.

[93] J. H. S. K. Monteiro, *Molecules* **2020**, *25*, 2089.

[94] G. Blasse in Spectra and Chemical Interactions, (Eds.: P. S. Braterman, G. Blasse, A. Müller, E. J. Baran, R. O. Carter), Springer, Berlin, Heidelberg, **1976**, pp. 43–79.

[95] M. Tamatani in *Fundamentals of Phosphors*, Num Pages: 24, CRC Press, **2007**.

[96] P. Dorenbos, *J. Lumin.* **2000**, *91*, 91–106.

[97] D. R. Pye, N. P. Mankad, *Chem. Sci.* **2017**, *8*, 1705–1718.

[98] I. G. Powers, C. Uyeda, *ACS Catal.* **2017**, *7*, 936–958.

[99] J. F. Berry, C. C. Lu, *Inorg. Chem.* **2017**, *56*, 7577–7581.

[100] F. A. Cotton, N. F. Curtis, C. B. Harris, B. F. G. Johnson, S. J. Lippard, J. T. Mague, W. R. Robinson, J. S. Wood, *Science* **1964**, *145*, 1305–1307.

[101] K. Shi, I. Douair, G. Feng, P. Wang, Y. Zhao, L. Maron, C. Zhu, *J. Am. Chem. Soc.* **2021**, *143*, 5998–6005.

[102] F. Völcker, F. M. Mück, K. D. Vogiatzis, K. Fink, P. W. Roesky, *Chem. Comm.* **2015**, *51*, 11761–11764.

[103] M. Dahlen, N. Reinfandt, C. Jin, M. T. Gamer, K. Fink, P. W. Roesky, *Chem. Eur. J.* **2021**, *27*, 15128–15136.

[104] C. Zovko, S. Bestgen, C. Schoo, A. Görner, J. M. Goicoechea, P. W. Roesky, *Chem. Eur. J.* **2020**, *26*, 13191–13202.

[105] G. S. Day, B. Pan, D. L. Kellenberger, B. M. Foxman, C. M. Thomas, *Chem. Commun.* **2011**, *47*, 3634–3636.

[106] L.-C. Liang, P.-S. Chien, J.-M. Lin, M.-H. Huang, Y.-L. Huang, J.-H. Liao, *Organometallics* **2006**, *25*, 1399–1411.

[107] TURBOMOLE V7.6 2022, a development of University of Karlsruhe Forschungszentrum Karlsruhe GmbH, 1989-2007, TURBOMOLE GmbH, since 2007; available from http://www.turbomole.com.

[108] A. D. Becke, *Phys. Rev. A* **1988**, *38*, 3098–3100.

[109] J. P. Perdew, *Phys. Rev. B* **1986**, *33*, 8822–8824.

[110] S. Grimme, J. Antony, S. Ehrlich, H. Krieg, *J. Chem. Phys.* **2010**, *132*, 154104.

[111] S. Grimme, S. Ehrlich, L. Goerigk, *J. Comput. Chem.* **2011**, *32*, 1456–1465.

[112] K. Eichkorn, O. Treutler, H. Öhm, M. Häser, R. Ahlrichs, *Chem. Phys. Lett.* **1995**, *240*, 283–290.

[113] K. Eichkorn, F. Weigend, O. Treutler, R. Ahlrichs, *Theoret. Chim. Acta.* **1997**, *97*, 119–124.

[114] F. Weigend, *Phys. Chem. Chem. Phys.* **2006**, *8*, 1057–1065.

[115] F. Weigend, R. Ahlrichs, *Phys. Chem. Chem. Phys.* **2005**, *7*, 3297–3305.

[116] J. P. Perdew, K. Burke, M. Ernzerhof, *Phys. Rev. Lett.* **1996**, *77*, 3865–3868.

[117] C. Adamo, V. Barone, *J. Chem. Phys.* **1999**, *110*, 6158–6170.

[118] S. Grimme, *J. Chem. Phys.* **2013**, *138*, 244104.

[119] W. Humphrey, A. Dalke, K. Schulten, *J. Mol. Graph.* **1996**, *14*, 33–38.

[120] A.-R. Allouche, *J. Comput. Chem.* **2011**, *32*, 174–182.

[121] Origin(Pro) Version 2022, **2022**, `https://www.originlab.com/index.aspx?go=Company&pid=1130`.

[122] K. B. Wiberg, *Tetrahedron* **1968**, *24*, 1083–1096.

[123] P. Su, H. Li, *J. Chem. Phys.* **2009**, *131*, 014102.

[124] H. H. Caspers, H. E. Rast, R. A. Buchanan, *Chem. Phys.* **1965**, *42*, 3214–3217.

[125] M. Dahlen, M. Kehry, S. Lebedkin, M. M.Â Kappes, W. Klopper, P. W.Â Roesky, *Dalton Trans.* **2021**, *50*, 13412–13420.

[126] *Kramida, A., Ralchenko, Yu., Reader, J., and NIST ASD Team (2021). NIST Atomic Spectra Database (ver. 5.9), [Online]. Available: https://physics.nist.gov/asd [2022, September 1]. National Institute of Standards and Technology, Gaithersburg, MD.*

[127] A. Gaita-Ariño, F. Luis, S. Hill, E. Coronado, *Nat. Chem.* **2019**, *11*, 301–309.

[128] J. Villain, F. Hartman-Boutron, R. Sessoli, A. Rettori, *EPL* **1994**, *27*, 159.

[129] A. M. Ako, I. J. Hewitt, V. Mereacre, R. Clérac, W. Wernsdorfer, C. E. Anson, A. K. Powell, *Angew. Chem. Int. Ed.* **2006**, *45*, 4926–4929.

[130] N. Ishikawa, M. Sugita, T. Ishikawa, S.-y. Koshihara, Y. Kaizu, *J. Am. Chem. Soc.* **2003**, *125*, 8694–8695.

[131] E. Coronado, *Nat. Rev. Mater.* **2020**, *5*, 87–104.

[132] M. A. AlDamen, J. M. Clemente-Juan, E. Coronado, C. Martí-Gastaldo, A. Gaita-Ariño, *J. Am. Chem. Soc.* **2008**, *130*, 8874–8875.

[133] M. A. AlDamen, S. Cardona-Serra, J. M. Clemente-Juan, E. Coronado, A. Gaita-Ariño, C. Martí-Gastaldo, F. Luis, O. Montero, *Inorg. Chem.* **2009**, *48*, 3467–3479.

[134] J. R. Friedman, M. P. Sarachik, J. Tejada, R. Ziolo, *Phys. Rev. Lett.* **1996**, *76*, 3830–3833.

[135] D. A. Garanin, E. M. Chudnovsky, *Phys. Rev. B* **1997**, *56*, 11102–11118.

[136] M. J. Giansiracusa, E. Moreno-Pineda, R. Hussain, R. Marx, M. MartÃnez Prada, P. Neugebauer, S. Al-Badran, D. Collison, F. Tuna, J. van Slageren, S. Carretta, T. Guidi, E. J. L. McInnes, R. E. P. Winpenny, N. F. Chilton, *J. Am. Chem. Soc.* **2018**, *140*, 2504–2513.

[137] F. Kleemiss, O. V. Dolomanov, M. Bodensteiner, N. Peyerimhoff, L. Midgley, L. J. Bourhis, A. Genoni, L. A. Malaspina, D. Jayatilaka, J. L. Spencer, F. White, B. Grundkötter-Stock, S. Steinhauer, D. Lentz, H. Puschmann, S. Grabowsky, *Chem. Sci.* **2021**, *12*, 1675–1692.

[138] J. Tao, J. P. Perdew, V. N. Staroverov, G. E. Scuseria, *Phys. Rev. Lett.* **2003**, *91*, 146401.

[139] P. Pollak, F. Weigend, *J. Chem. Theory Comput.* **2017**, *13*, 3696–3705.

[140] C. van Wüllen, *J. Chem. Phys.* **2004**, *120*, 7307–7313.

[141] C. van Wüllen, C. Michauk, *J. Chem. Phys.* **2005**, *123*, 204113.

[142] C. Lee, W. Yang, R. G. Parr, *Phys. Rev. B* **1988**, *37*, 785–789.

[143] A. D. Becke, *J. Chem. Phys.* **1992**, *96*, 2155–2160.

[144] J. J. Le Roy, L. Ungur, I. Korobkov, L. F. Chibotaru, M. Murugesu, *J. Am. Chem. Soc.* **2014**, *136*, 8003–8010.

[145] J. J. Le Roy, M. Jeletic, S. I. Gorelsky, I. Korobkov, L. Ungur, L. F. Chibotaru, M. Murugesu, *J. Am. Chem. Soc.* **2013**, *135*, 3502–3510.

[146] J. D. Rinehart, J. R. Long, *Chem. Sci.* **2011**, *2*, 2078–2085.

[147] G. Cucinotta, M. Perfetti, J. Luzon, M. Etienne, P.-E. Car, A. Caneschi, G. Calvez, K. Bernot, R. Sessoli, *Angew. Chem. Int. Ed.* **2012**, *51*, 1606–1610.

[148] N. F. Chilton, R. P. Anderson, L. D. Turner, A. Soncini, K. S. Murray, *J. Comput. Chem.* **2013**, *34*, 1164–1175.

[149] F. Illas, R. L. Martin, *J. Chem. Phys.* **1998**, *108*, 2519–2527.

[150] A. Abragam, B. Bleaney, *Electron Paramagnetic Resonance of Transition Ions*, Oxford, New York, **2012**.

[151] M. Zając, C. Rudowicz, *Acta Phys. Pol. A* **2017**, *132*, 19–23.

[152] W. Wernsdorfer, N. Aliaga-Alcalde, D. N. Hendrickson, G. Christou, *Nature* **2002**, *416*, 406–409.

[153] J. J. L. Roy, I. Korobkov, M. Murugesu, *Chem. Commun.* **2014**, *50*, Publisher: Royal Society of Chemistry, 1602–1604.

[154] B. Cantor, I. T. H. Chang, P. Knight, A. J. B. Vincent, *Mater. Sci. Eng. A* **2004**, *375-377*, 213–218.

[155] J.-W. Yeh, S.-K. Chen, S.-J. Lin, J.-Y. Gan, T.-S. Chin, T.-T. Shun, C.-H. Tsau, S.-Y. Chang, *Adv. Eng. Mater.* **2004**, *6*, 299–303.

[156] *High-Entropy Alloys*, (Eds.: M. C. Gao, J.-W. Yeh, P. K. Liaw, Y. Zhang), Springer International Publishing, Cham, **2016**.

[157] A. Sarkar, Q. Wang, A. Schiele, M. R. Chellali, S. S. Bhattacharya, D. Wang, T. Brezesinski, H. Hahn, L. Velasco, B. Breitung, *Adv. Mater.* **2019**, *31*, 1806236.

[158] C. M. Rost, E. Sachet, T. Borman, A. Moballegh, E. C. Dickey, D. Hou, J. L. Jones, S. Curtarolo, J.-P. Maria, *Nat. Commun,* **2015**, *6*, 8485.

[159] S. H. Albedwawi, A. AlJaberi, G. N. Haidemenopoulos, K. Polychronopoulou, *Mater. Des.* **2021**, *202*, 109534.

[160] S. Zhu, Y. Chen, V. Somayaji, P. Novello, D. Chacko, F. Li, J. Liu, *ACS Appl. Mater. Interfaces* **2023**, *15*, 31384–31392.

[161] S. Nundy, D. Tatar, J. Kojčinović, H. Ullah, A. Ghosh, T. K. Mallick, R. Meinusch, B. M. Smarsly, A. A. Tahir, I. Djerdj, *Adv. Sustain. Syst.* **2022**, *6*, 2200067.

[162] W. Kohn, L. J. Sham, *Phys. Rev.* **1965**, *140*, A1133–A1138.

[163] N. Ashcroft, N. D. Mermin, *Solid State Physics*, Saunders Collage Publishing, **1976**, 848 pp.

[164] V. I. Anisimov, J. Zaanen, O. K. Andersen, *Phys. Rev. B* **1991**, *44*, 943–954.

[165] A. Svane, *Phys. Rev. Lett.* **1992**, *68*, 1900–1903.

[166] K. Bhola, J. J. Varghese, L. Dapeng, Y. Liu, S. H. Mushrif, *J. Phys. Chem. C* **2017**, *121*, 21343–21353.

[167] J. Paier, C. Penschke, J. Sauer, *Chem. Rev.* **2013**, *113*, 3949–3985.

[168] R. L. Martin, F. Illas, *Phys. Rev. Lett.* **1997**, *79*, 1539–1542.

[169] J. L. F. Da Silva, M. V. Ganduglia-Pirovano, J. Sauer, V. Bayer, G. Kresse, *Phys. Rev. B* **2007**, *75*, 045121.

[170] E. R. Batista, R. A. Friesner, *J. Phys. Chem. B* **2002**, *106*, 8136–8141.

[171] P. S. Bagus, M. J. Sassi, K. M. Rosso, *J. Chem. Phys.* **2019**, *151*, 044107.

[172] B. Herschend, M. Baudin, K. Hermansson, *Surf. Sci.* **2005**, *599*, 173–186.

[173] C. Müller, B. Herschend, K. Hermansson, B. Paulus, *J. Chem. Phys.* **2008**, *128*, 214701.

[174] Z. Barandiarán, L. Seijo, *J. Chem. Phys.* **1988**, *89*, 5739–5746.

[175] L. Seijo, Z. Barandiarán, *J. Chem. Phys.* **1991**, *94*, 8158–8164.

[176] J. Sauer, *Chem. Rev.* **1989**, *89*, 199–255.

[177] H. M. Evjen, *Phys. Rev.* **1932**, *39*, 675–687.

[178] U. Wedig, PhD thesis, Karlsruher Institut für Technologie (KIT), **1986**.

[179] M. Dolg, H. Stoll, A. Savin, H. Preuss, *Theoret. Chim. Acta.* **1989**, *75*, 173–194.

[180] J. Kullgren, C. W. M. Castleton, C. Müller, D. M. Ramo, K. Hermansson, *J. Chem. Phys.* **2010**, *132*, 054110.

[181] K. Momma, F. Izumi, *J. Appl. Cryst.* **2011**, *44*, 1272–1276.

[182] J. D. Hunter, *CiSE* **2007**, *9*, 90–95.

[183] R. D. Shannon, *Acta. Cryst. A* **1976**, *32*, 751–767.

[184] M. A. Panhans, R. N. Blumenthal, *Solid State Ion.* **1993**, *60*, 279–298.

[185] R. J. Gorte, *AIChE Journal* **2010**, *56*, 1126–1135.

[186] J. Heyd, G. E. Scuseria, M. Ernzerhof, *J. Chem. Phys.* **2003**, *118*, 8207–8215.

[187] J. Heyd, G. E. Scuseria, M. Ernzerhof, *J. Chem. Phys.* **2006**, *124*, 219906.

[188] A. M. Burow, M. Sierka, J. Döbler, J. Sauer, *J. Chem. Phys.* **2009**, *130*, 174710.

[189] X. Zhang, L. Zhu, Q. Hou, J. Guan, Y. Lu, T. W. Keal, J. Buckeridge, C. R. A. Catlow, A. A. Sokol, *Chem. Mater.* **2023**, *35*, 207–227.

[190] M. V. Ganduglia-Pirovano, G. E. Murgida, V. Ferrari, A. M. Llois, *J. Phys. Chem. C* **2017**, *121*, 21080–21083.

[191] G. E. Murgida, V. Ferrari, M. V. Ganduglia-Pirovano, A. M. Llois, *Phys. Rev. B* **2014**, *90*, 115120.

[192] G. E. Murgida, M. V. Ganduglia-Pirovano, *Phys. Rev. Lett.* **2013**, *110*, 246101.

[193] M. V. Ganduglia-Pirovano, J. L. F. Da Silva, J. Sauer, *Phys. Rev. Lett.* **2009**, *102*, Publisher: American Physical Society, 026101.

[194] X. Han, N. Amrane, Z. Zhang, M. Benkraouda, *J. Phys. Chem. C* **2016**, *120*, 13325–13331.

[195] X. Han, N. Amrane, Z. Zhang, M. Benkraouda, *J. Phys. Chem. C* **2017**, *121*, 21084–21086.

[196] P. R. L. Keating, D. O. Scanlon, B. J. Morgan, N. M. Galea, G. W. Watson, *J. Phys. Chem. C* **2012**, *116*, 2443–2452.

[197] M. Nolan, S. C. Parker, G. W. Watson, *Surf. Sci.* **2005**, *595*, 223–232.

[198] F. Esch, S. Fabris, L. Zhou, T. Montini, C. Africh, P. Fornasiero, G. Comelli, R. Rosei, *Science* **2005**, *309*, 752–755.

[199] A. V. Krukau, O. A. Vydrov, A. F. Izmaylov, G. E. Scuseria, *Chem. Phys.* **2006**, *125*, 224106.

[200] J. Kullgren, K. Hermansson, C. Castleton, *J. Chem. Phys.* **2012**, *137*, 044705.

[201] M. J. Weber, *J. Appl. Phys.* **1973**, *44*, 3205–3208.

[202] R. A. Buchanan, H. E. Rast, H. H. Caspers, *J. Chem. Phys.* **1966**, *44*, 4063–4065.

[203] S. Afrin, P. Bollini, *J. Phys. Chem. C* **2023**, *127*, 234–247.

[204] K. Andersson, P. A. Malmqvist, B. O. Roos, A. J. Sadlej, K. Wolinski, *J. Phys. Chem.* **1990**, *94*, 5483–5488.

[205] K. Andersson, P.-Å. Malmqvist, B. O. O. Roos, *J. Chem. Phys.* **1992**, *96*, 1218–1226.

[206] Y. Shimizu, Y. Takano, K. Ueda, *J. Lumin.* **2013**, *141*, 44–47.

[207] Z. J. Corey, P. Lu, G. Zhang, Y. Sharma, B. X. Rutherford, S. Dhole, P. Roy, Z. Wang, Y. Wu, H. Wang, A. Chen, Q. Jia, *Adv. Sci.* **2022**, *9*, 2202671.

Acronyms and Abbreviations

CM Coinage Metal

J Coupling Constant

KD Kramer's Doublet

LLCT Ligand to Ligand Charge Transfer

LMMCT Ligand to Metal-Metal Charge Transfer

OLED Organic Light-Emitting Diode

SMM Single Molecule Magnet

TDDFT Time-dependent Density Functional Theory

TM Transition Metal

rs Russell-Saunders

sTDA simplified Tamm-Dancoff Approximation

BS Broken Symmetry

CASOCI Complete Active Space Spin-orbit Configuration Interaction

CASSCF Complete Active Space Self-Consistent Field

CI Configuration Interaction

CT Charge transfer

DFT Density Functional Theory

ECP Effective Core Potential

GGA Generalized Gradient Approximation

HF Hartree-Fock theory

HOMO Highest Occupied Molecular Orbital

LDA Local Density Approximation

LUMO Lowest Occupied Molecular Orbital

MO Molecular Orbital

NMO Non-orthogonal Magnetic Orbital

OMO Orthogonal Magnetic Orbital

RHF Restricted Hartree-Fock

RI Resolution of the Identity

ROHF Restricted Open-shell Hartree-Fock

SD Slater Determinant

TDM Transition Dipole Moment

UHF Unrestricted Hartree-Fock

Permissions to Print

This work contains material adapted from work previously published in scientific journals. Permissions for reuse or reprint of the relevant content has been requested to the copyright owner.

- Chapter 3: Partially adapted from *Hetero-bimetallic Lanthanide-Coinage Metal Compounds Featuring Possible Metal-Metal Interactions in the Excited State* Milena Dahlen, Niklas Reinfandt, Chengyu Jin, Dr. Michael T. Gamer, Prof.Dr. Karin Fink, Prof.Dr. Peter W. Roesky *Chemistry—A European Journal* **27**, 15128 –15136, (2021). The Authors. Wiley-VCH.
- Chapter 4: Partially adapted from *Unique Double and Triple Decker Arrangements of Rare-Earth 9,10-Diborataanthracene Complexes Featuring Single-Molecule Magnet Characteristics* Cedric Uhlmann, Luca Münzfeld, Adrian Hauser, Ting-Ting Ruan, Senthil Kumar Kuppusamy, Chengyu Jin, Mario Ruben, Karin Fink, Eufemio Moreno-Pineda, Peter Werner Roesky *Angewandte Chemie International Edition* **Accepted**, e202401372, (2024).

List of Publications

- *Unique Double and Triple Decker Arrangements of Rare-Earth 9,10-Diborataanthracene Complexes Featuring Single-Molecule Magnet Characteristics* Cedric Uhlmann, Luca Münzfeld, Adrian Hauser, Ting-Ting Ruan, Senthil Kumar Kuppusamy, Chengyu Jin, Mario Ruben, Karin Fink, Eufemio Moreno-Pineda, Peter Werner Roesky, *Angewandte Chemie International Edition* **editting**, 15128–15136, (2024)
- *Experimental and computational study of the exchange interaction between the V(iii) centers in the vanadium-cyclal dimer* Andreas Reiß, Maximilian Kai Reimann, Chengyu Jin, Martha Wachter-Lehn, Reinhard K. Kremer, Rainer Pöttgen, Karin Fink, Wim Klopper, Claus Feldmann *Dalton Transactions* **52**, 17389, (2023)
- *Hetero-bimetallic Lanthanide-Coinage Metal Compounds Featuring Possible Metal-Metal Interactions in the Excited State* Milena Dahlen, Niklas Reinfandt, Chengyu Jin, Dr. Michael T. Gamer, Prof.Dr. Karin Fink, Prof.Dr. Peter W. Roesky, *Chemistry—A European Journal* **27**, 15128–15136, (2021)

Acknowledgments

This thesis is made possible through the support of the Virtual Material Design (Virtmat) initiative at Karlsruhe Institute of Technology, the DFG-funded SFB/TRR 88 Transregional Collaborative Research Center "Cooperative Effects in Homo- and Hetero-metallic Complexes (3MET)," and the DFG-funded Collaborative Research Centre (CRC) 1573 "4f for Future."

I express my deepest gratitude to Prof. Dr. Karin Fink for imparting knowledge and practical skills. Her patience, encouragement, and role modeling have been instrumental. Special thanks to Prof. Dr. Willem Klopper for his pivotal role as Korreferent.

Heartfelt thanks to colleagues and collaborators for their contributions and valuable feedback. Special mention to Dr. Angsar Pausch, Christian Pachl, and Dr. Juana Vázquez Quesada for proofreading this thesis.

I extend my gratitude to my grandparents for shaping my intellectual journey and to my mother, Li Hao, for the gift of life.

Lastly, sincere appreciation to all friends for being companions in this Ph.D. adventure. Our shared joy in exploration and creativity has made this journey fulfilling, and your support has been a beacon of light during challenging times.

Declaration

I, Chengyu Jin, declare that for the polishing and translation of my thesis, I have utilized the language model GPT-4 (Generative Pre-trained Transformer 4), developed by OpenAI. The usage of GPT-4 was specifically employed for refining the language as well as for the translation of the abstract into German. I acknowledge that while GPT-4 has been a valuable aid in the editing and translation processes, the ultimate responsibility for the content and accuracy of my thesis lies with me as the author.